

Evolutionary tracks of quiet-Sun magnetic features

Iker Sánchez Requerey

INSTITUTO DE ASTROFÍSICA DE ANDALUCÍA
Consejo Superior de Investigaciones Científicas

Memoria para optar al grado de
Doctor en Ciencias Físicas

Editor: Universidad de Granada. Tesis Doctorales

Autor: Iker Sánchez Requerey

ISBN: 978-84-9125-411-9

URI: <http://hdl.handle.net/10481/41719>

DECLARACIÓN

El doctorando **Iker Sánchez Requerey** y el director de la tesis **Dr. Jose Carlos del Toro Iniesta** garantizamos, al firmar esta tesis doctoral, que el trabajo ha sido realizado por el doctorando bajo la dirección del director de la tesis y, hasta donde nuestro conocimiento alcanza, en la realización del trabajo, se han respetado los derechos de otros autores a ser citados, cuando se han utilizado sus resultados o publicaciones.



Iker Sánchez Requerey

El doctorando



Dr. Jose Carlos del Toro Iniesta

El director

Granada, 30 de octubre de 2015.

RESUMEN

Esta tesis presenta un estudio de estructuras magnéticas fotosféricas del Sol en calma. Los campos magnéticos del Sol en calma se organizan a pequeñas escalas, evolucionan rápidamente y producen débiles señales de polarización. Estas propiedades físicas exigen medidas de la mayor resolución espacial y temporal posible junto con altas sensibilidad y precisión polarimétricas. Estas limitaciones instrumentales han causado que el origen y evolución de estas pequeñas estructuras permanezca aún relativamente desconocido.

IMaX (siglas de Imaging Magnetograph eXperiment o *imaginador* magnetográfico experimental) es un espectropolarímetro con imagen que voló sobre el círculo polar ártico a bordo del globo estratosférico SUNRISE. IMaX se diseñó para aliviar los problemas anteriores y ha proporcionado observaciones con la inédita resolución espacial de unos cien kilómetros. Al volar en la estratosfera, obtuvo series temporales de imágenes virtualmente libres del *seeing* que cubrían vastas zonas del Sol. Estas características son de verdad cruciales para estudiar la naturaleza altamente dinámica del magnetismo del Sol en calma.

La tesis reúne pruebas empíricas sobre la magnetoconvección a las escalas más pequeñas jamás observadas. Presentamos trazas evolutivas de diversas estructuras magnéticas del Sol en calma que se encuentran en continua interacción con la convección fotosférica. Específicamente, estudiamos 1) la formación y evolución de un elemento magnético aislado; 2) la dinámica de estructuras magnéticas multinúcleo; y 3) la relación entre estructuras magnéticas y sumideros persistentes sostenidos por la convección en las uniones de varias células mesogranulares.

Vista a la escala de unos cien kilómetros, la evolución de la estructura magnética aislada se contempla como un proceso complicado en el que intervienen muchos fenómenos. Su formación comienza cuando un pequeño bucle magnético emerge a la fotosfera en una zona de flujo ascendente granular. Sus pies son barridos rápidamente hacia las líneas intergranulares cercanas donde se encuentran previamente algunas otras estructuras de polaridad positiva. El pie negativo se cancela con una estructura positiva mientras que los flujos conectivos granulares desplazan el positivo y otros remanentes hacia un sumidero persistente.

Sus campos magnéticos se aglutinan en el sumidero dando forma a un nuevo elemento cuya intensidad de campo se encuentra en valores de equipartición con la densidad de energía cinética de los movimientos convectivos. El flujo descendente intergranular empieza entonces a incrementarse en la estructura magnética, a la vez que los gránulos circundantes la comprimen hasta que alcanza intensidades de kiloGauss. Durante este proceso, aparece un punto brillante en el borde de la concentración de flujo casi coespacial con una pluma de flujo ascendente. El desarrollo del elemento magnético no se detiene ahí sino que resulta ser inestable. De hecho, muestra un comportamiento oscilatorio ya que su intensidad magnética decae y se refuerza con el tiempo.

Si nos centramos en estructuras magnéticas extendidas que albergan varios puntos brillantes en su interior, encontramos que son resolubles en varios núcleos magnéticos más elementales, cada uno de los cuales se encuentra relacionado con un punto brillante. Los núcleos más internos son intensos y verticales. Están rodeados por un conjunto de campos magnéticos más débiles e inclinados. Nosotros interpretamos esas estructuras como ramilletes de concentraciones de flujo en la baja fotosfera que se expanden con la altura hasta mezclarse en una única marquesina común en las capas fotosféricas altas. Los flujos convectivos granulares locales gobiernan la evolución de los núcleos magnéticos individuales. Mediante tal interacción, los núcleos se intensifican, se fragmentan y se funden de la misma manera que otras observaciones fotométricas informan que hacen las cadenas de puntos brillantes. Tal comportamiento evolutivo se traduce en oscilaciones de campo de la estructura global. Nosotros concluimos que tales oscilaciones —previamente descubiertas en pequeños elementos magnéticos del Sol en calma— obedecen más a la presión de los movimientos granulares que a modos oscilatorios propios de tubos delgados de flujo magnético.

Finalmente, analizamos la relación entre flujos mesogranulares, flujos descendentes localizados y campos magnéticos del Sol en calma. Comenzamos por un estudio estadístico de los sumideros. Algunos se muestran como remolinos mientras que otros despliegan flujos radialmente convergentes. Su distribución espacial los sitúa en los vértices de mesogranulos vecinos. Demostramos cuantitativamente que los campos más intensos tienden a concentrarse en los sumideros. Por el contrario, los bucles magnéticos a pequeña escala no muestran distribución preferente alguna a escalas mesogranulares. Así mismo, analizamos en detalle uno de los mesogranulos y descubrimos que los bucles magnéticos que aparecen en el seno de su celda mesogranular pueden ser arrastrados por los flujos hacia uno de los vértices. Si nuestras observaciones se confirman, estos resultados pueden implicar que la formación de elementos magnéticos a través de la concentración de pies de bucles en vértices mesogranulares es ubicua en la superficie solar.

SUMMARY

This thesis presents a study of quiet-Sun magnetic features in the solar photosphere. Magnetic fields in the quiet Sun organize on small spatial scales, evolve very rapidly, and produce weak polarization signals. With these properties their observation requires high spatial and temporal resolution together with sensitive and accurate polarimetric measurements. It is for these instrumental limitations that the origin and evolution of these features remains elusive.

The Imaging Magnetograph eXperiment (IMaX) is an imaging spectropolarimeter that flew over the Arctic Circle aboard the SUNRISE balloon-borne stratospheric mission. IMaX was designed to mitigate the above mentioned issues and has provided polarimetric observations with unprecedentedly high spatial resolution of a hundred kilometers. Flying in the stratosphere, it obtained stable, nearly seeing-free time series, and its imaging capabilities allowed to cover large areas of the Sun simultaneously. All these features are indeed crucial when studying the highly dynamic nature of the quiet-Sun magnetism.

The thesis gathers empirical evidence of magnetoconvection at the smallest scales ever observed. The evolutionary tracks of several different quiet-Sun magnetic structures in a continuous interaction with photospheric convection are presented. Specifically, we study 1) the formation and evolution of an isolated magnetic element; 2) the dynamics of multi-core magnetic structures; and 3) the relation between magnetic features and convectively driven, long living sinks at the junctions of several mesogranular cells.

Seen at a scale of one hundred kilometers, we find that the evolution of an isolated quiet-Sun magnetic element is a complex process where many phenomena are involved. The formation starts when a small-scale magnetic loop emerges through the solar surface in a granular upflow. Its footpoints are soon swept to nearby intergranular lanes where some, weak positive polarity patches are already present. The negative polarity footpoint cancels out with an opposite polarity feature while the positive one and other remaining patches are advected by converging granular flows toward a long-living sink. The magnetic fields agglomerate in the sinkhole and a new element with a magnetic field strength in equipartition with the kinetic energy density of convective motions is formed. The intergranular downflow

then begins to increase within the magnetic feature while the surrounding granules compress it until kiloGauss field strengths are reached. During this process, a bright point appears at the edge of the flux concentration almost co-spatial with an upflow plume. The development of the magnetic element does not stop here since we discover that it is indeed unstable. The magnetic element displays an oscillatory behavior as the field strength weakens and rises again with time.

Focusing on extended magnetic structures that harbor multiple bright points in their interiors, we find that they are resolvable into a series of more elemental inner magnetic cores, each of which appears related with a single bright point. The inner cores are strong and vertical. They all are surrounded by common, weaker, and more inclined fields. We interpret these structures as bundles of flux concentrations in the lower photosphere that expand with height to merge into a common canopy in the upper photospheric layers. The evolution of the individual magnetic cores is completely governed by the local granular convection flows. Through this interaction, they continuously intensify, fragment, and merge in the same way that chains of bright points in photometric observations have been reported to do. This evolutionary behavior results in magnetic field oscillations of the global entity. We conclude that the magnetic field oscillations previously discovered in small quiet-Sun magnetic elements correspond to the forcing by granular motions and not to characteristic oscillatory modes of thin flux tubes.

Finally, we analyze the relation between mesogranular flows, localized downdrafts, and quiet-Sun magnetic fields. We study first the statistical properties of the sinks. Some of them manifest as whirlpools while the others display radially symmetrical converging flows. Their spatial distribution reveals that they are located at the vertices between neighboring mesogranules. We prove quantitatively that the strongest fields tend to concentrate at sink-holes. Meanwhile, the small-scale magnetic loops do not show any preferential distribution at mesogranular scales. We also analyze one of the mesogranules in more detail and observe that magnetic loops appearing inside the mesogranular cell can be advected by horizontal flows toward its vertex. If confirmed by new observations, these results can imply that the formation of magnetic elements through the concentration of loop footpoints in mesogranular vertices is ubiquitous over the solar surface.

CONTENTS

1	Introduction	1
1.1	The solar structure	1
1.2	Quiet-Sun magnetic fields	3
1.2.1	Spatial distribution of quiet-Sun magnetic fields	6
1.2.2	Magnetic field strength and inclination in the IN	7
1.2.3	Formation of magnetic elements	9
1.2.4	Bright points and magnetic flux tubes	10
1.2.5	Origin of IN magnetic fields	12
1.3	Motivation of this work	13
2	Spectropolarimetry	15
2.1	Measurements of polarized light	15
2.2	Spectropolarimetry with IMaX	18
2.2.1	Polarimetric analysis	18
2.2.2	Spectral analysis	20
2.3	The radiative transfer equation in a magnetized atmosphere	21
3	Instrumentation, data and analysis	25
3.1	SUNRISE stratospheric balloon-borne solar observatory	25
3.1.1	IMaX: the Imaging Magnetograph eXperiment	26
3.1.2	SuFI: the SUNRISE Filter Imager	28
3.2	Diagnostics of physical quantities	29
3.2.1	The inversion problem	29
3.2.2	SIR: Stokes Inversions based on Response functions	30
4	The history of a quiet-Sun magnetic element	33
4.1	Introduction	34

4.2	Observations and data analysis	36
4.3	Flux concentration	39
4.4	Formation of a kiloGauss magnetic flux tube	43
4.4.1	Converging granules and small-scale upflow features	48
4.4.2	Bright points inside the flux tube	49
4.5	Mature flux tube	50
4.5.1	Downflow plumes	51
4.6	Averaged history	54
4.7	Summary and Conclusions	55
5	Dynamics of multi-cored magnetic structures in the quiet Sun	59
5.1	Introduction	60
5.2	Observations and data reduction	62
5.3	Data analysis	64
5.4	Multi-cored magnetic structures	65
5.5	Evolution of magnetic elements	68
5.6	Interaction with granular convection	70
5.6.1	Intensification by granule compression	70
5.6.2	Fragmentation	72
5.6.3	Coalescence and further fragmentation	72
5.7	Magnetic field oscillations	74
5.8	Discussion and conclusions	76
6	On the relation between magnetic fields and convectively driven sinks in the quiet Sun	81
6.1	Introduction	82
6.2	Observations	83
6.3	Sink detection and statistics	86
6.3.1	Mesogranular lane identification	86
6.3.2	Sink identification	87
6.3.3	Sink classification	87
6.3.4	Sink statistics	88
6.4	Correlation between mesogranules, sinks, and magnetic fields	90
6.4.1	Mesogranule: a case study	92
6.5	Discussion and conclusions	95
7	Conclusions	97

INTRODUCTION

The solar photosphere is a unique laboratory for studying ubiquitous astrophysical processes such as the interaction between plasma and magnetic fields. At this thin layer sunspots appear as the most outstanding footprints of solar activity in white light. Outside them, in the *quiet Sun*, only convective granules seem to pervade the vast majority of the solar surface. When seen in polarized light, however, a reticular network of magnetic structures is revealed. The regions between them, the so-called internetwork, have been thought to be devoid of magnetic signals for long. In the last years, the development of new instrumentation with steadily increasing spatial resolution and polarimetric sensitivity has turned our understanding of the internetwork magnetic fields upside down. From being basically quiet (i.e., non magnetic), it has started to exhibit an extraordinary magnetic activity. This revolution has been led by seeing-free space-borne missions that together with the advent of sophisticated numerical models have led to a new age of discoveries. The aim of this thesis is to contribute to the understanding of the quiet-Sun magnetism based on the analysis of spectropolarimetric data from the SUNRISE balloon-borne solar observatory.

1.1 The solar structure

Deep in the solar core, at an effective temperature of $\sim 1.5 \times 10^7$ K, quantum-tunneling effect drives nuclear fusion between hydrogen atoms. The energy released through this process travels outward, first as radiation (in the innermost 70% of the solar radius) and later by convection (see textbooks by, e.g., [Stix 2002](#); [Foukal 2004](#)). At the visible surface of the Sun, more than 90% of the solar radiation escapes into space through radiative cooling of convective material. The escaping photons carry away some of the thermal energy of the

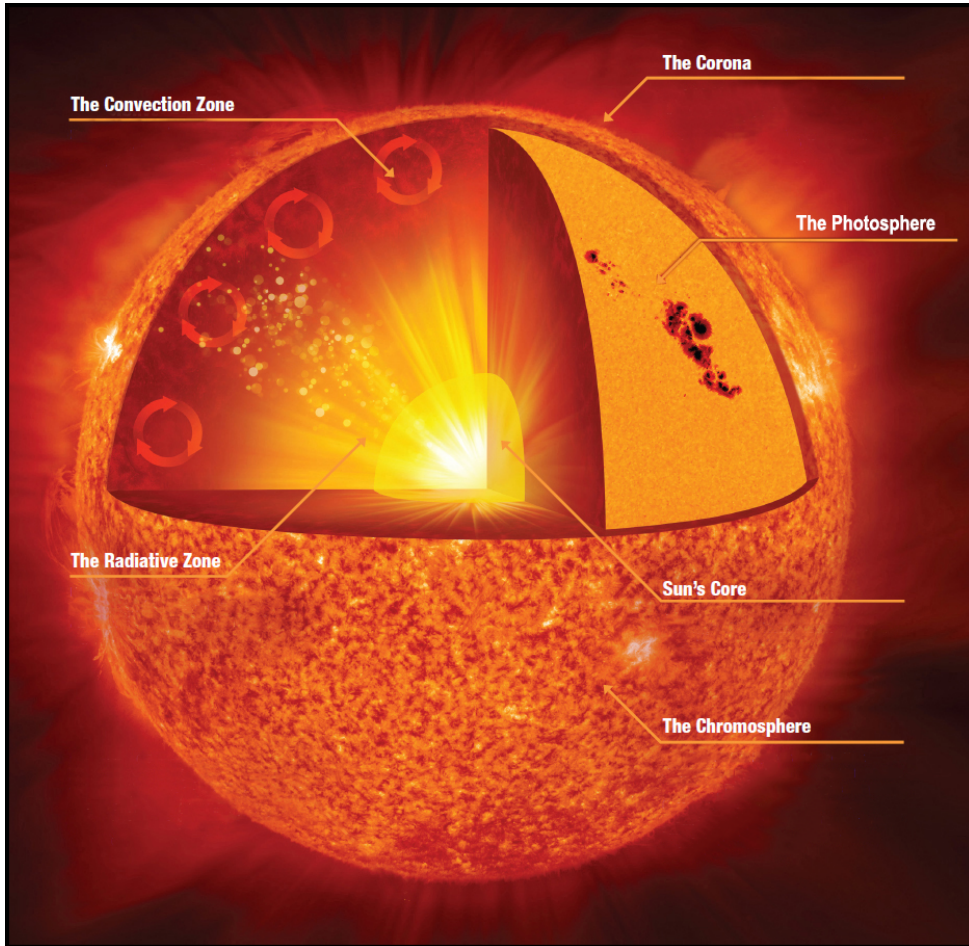


Figure 1.1: Illustration of the Sun structure from the core to the corona. See text for details. Image adapted from NASA/Jenny Mottar.

rising plasma. As a result, the plasma cools down, moves horizontally, and sinks back down into the Sun. This convection is observed as a granular pattern in the intensity variations of visible light images, where bright (hot) granules are surrounded by dark (cooler) lanes (see [Nordlund et al. 2009](#), for a review). The bright granules have a diameter of approximately 1 Mm and they are related with convective upflows, whereas the dark intergranular lanes are associated with convective downflows.

The solar atmosphere is the region from which photons escape into space. According to the different physical properties, it can be divided in three main layers, namely, the *photosphere*, the *chromosphere*, and the *corona*. The base of the photosphere (i.e. the solar

surface) is defined as the region where the continuum optical depth, τ_c , at 500 nm, is unity. Its effective temperature is ~ 5700 K and it spans vertically for about 500 km. At this height, the temperature reaches its minimum value ~ 4500 K (temperature minimum; e.g., Foukal 2004). Starting from the temperature minimum, the chromosphere is a ~ 1500 km wide layer where a broad temperature plateau of $\sim 10^4$ K (e.g., Stix 2002) is reached. The particle density drops rapidly from 10^{23} m^{-3} to 10^{19} m^{-3} in this layer. Above the chromosphere the solar corona extends from the top of a narrow *transition region* (within which the temperature abruptly increases from $\sim 10^4$ K to $\sim 10^6$ K) out into the *solar wind* (e.g., Priest 2014). The Sun structure from the core to the corona is illustrated in Figure 1.1.

The heating of the upper solar atmosphere is one of the most important problems in astrophysics (Klimchuk 2006; Parnell & De Moortel 2012). There is still no clear consensus about the mechanism (or mechanisms) which heats the chromosphere to 10^4 K and the corona to 10^6 K, in comparison with the 6000 K photosphere. The difficulties arise from the fact that the different atmospheric layers (which differ strongly in their plasma properties) are not energetically isolated from the others and rather the whole solar atmosphere forms a highly coupled system. Since the magnetic field of the Sun connects the different atmospheric layers, it is generally accepted that solar magnetism plays a key role in the chromospheric and coronal heating. The magnetic field is created in the solar interior, is measured with highest sensitivity on the photosphere and is responsible for most of the dynamical processes in the solar atmosphere (see Wiegmann et al. 2014, for a review).

1.2 Quiet-Sun magnetic fields

Magnetic fields in the Sun were first discovered in sunspots by Hale (1908, see Del Toro Iniesta (1996) for a review of historical details) and later in their near vicinity (Babcock & Babcock 1955), at plage regions (also called faculae when seen in the solar limb). In the solar photosphere sunspots appear darker (cooler) than their surroundings while plage regions are seen as conspicuous bright (hot) areas around sunspots. The non-stationary evolution of magnetic fields at these regions were soon related with the solar activity, which manifests as eruptive processes, coronal activity, and geomagnetic disturbances, among others. This connection between solar activity and magnetic fields gave rise to the concept of *active region*. Since then, the areas of the solar surface outside sunspot and plage regions are termed the *quiet Sun* (see recent reviews by de Wijn et al. 2009; Sánchez Almeida & Martínez González 2011; Martínez Pillet 2013; Bellot Rubio & Orozco Suárez 2015).

The Sun was considered non magnetic everywhere outside active regions until the 1970's when a substantial amount of the solar magnetic flux was found. In particular, Howard & Stenflo (1972) estimated that more than 90% of the total magnetic flux at the solar surface

is concentrated in the boundaries of supergranules, which have diameters of about 30 Mm (see [Rieutord & Rincon 2010](#), for a review). Full disk longitudinal magnetograms reveal that the magnetic fields at these locations display a reticular pattern which forms the so-called magnetic *network* (see [Figure 1.2 \(b\)](#)). The magnetic field in the network has field strengths of the order of kiloGauss values (e.g., [Stenflo 1973](#); [Wiehr 1978](#); [Solanki & Stenflo 1984](#); [Stenflo & Harvey 1985](#); [Solanki et al. 1987](#); [Grossmann-Doerth et al. 1996](#)). Weaker magnetic signals were soon discovered in the interiors of supergranular cells ([Livingston & Harvey 1971, 1975](#); [Smithson 1975](#)) and the term intranetwork ([Martin 1984](#)) or *internetwork* ([Lites et al. 1993](#)) was created. Internetwork (IN) magnetic fields cover the vast majority of the solar surface and they have been estimated to contribute the solar magnetic flux with ~ 26 Mx per day ([Zhou et al. 2013](#)), over 4 orders of magnitude higher than the active region contribution.

At the solar disk center, and under the weak field regime (e.g., [Landi Degl'Innocenti & Landolfi 2004](#)), the circular and linear polarization states of the outgoing light are mostly produced by the longitudinal and transverse (horizontal) components of the magnetic field, respectively. In the jargon of solar physicists, circular polarization maps are commonly known as longitudinal magnetograms where positive (negative) polarities stand for magnetic fields pointing toward the observer (down into the Sun). Observed in circularly polarized light, IN magnetic fields appear as small discrete magnetic features (*magnetic elements*) with mixed polarities ([Livingston & Harvey 1975](#)). The lifetime of magnetic elements range from 1 to 20 minutes ([Zhou et al. 2010](#)), but many of them survive several hours while they interact with other features ([de Wijn et al. 2008](#)). As soon as linearly polarized light was measured, a new component of the quiet Sun magnetism became apparent in the form of arcsecond scale linear polarization patches ([Lites et al. 1996](#)). These patches, or Horizontal Internetwork Fields (HIFs) as they were called, are very dynamic ([Danilovic et al. 2010b](#)), with a lifetime of less than 10 minutes, comparable to that of granules. Some of them appear between two opposite-polarity patches. Such structures are interpreted as low-lying (photospheric) magnetic loops ([Martínez González et al. 2007](#)) where the two opposite circular patches and the linear one are created by the two footpoints and the apex of the loop, respectively ([Centeno et al. 2007](#)). A significant fraction of them emerge through the solar surface in the form of Ω -loops ([Martínez González & Bellot Rubio 2009](#)). They carry an enormous amount of flux to the photosphere, with values of 1.1×10^{24} Mx day $^{-1}$ ([Martínez González & Bellot Rubio 2009](#)) and 9.8×10^{24} Mx day $^{-1}$ ([Jin et al. 2009](#)) over the solar surface for Ω -loops and HIFs, respectively. About 23 % of the loops reach the chromosphere and thus may supply a substantial amount of energy to the upper atmospheric layers ([Martínez González & Bellot Rubio 2009](#)).

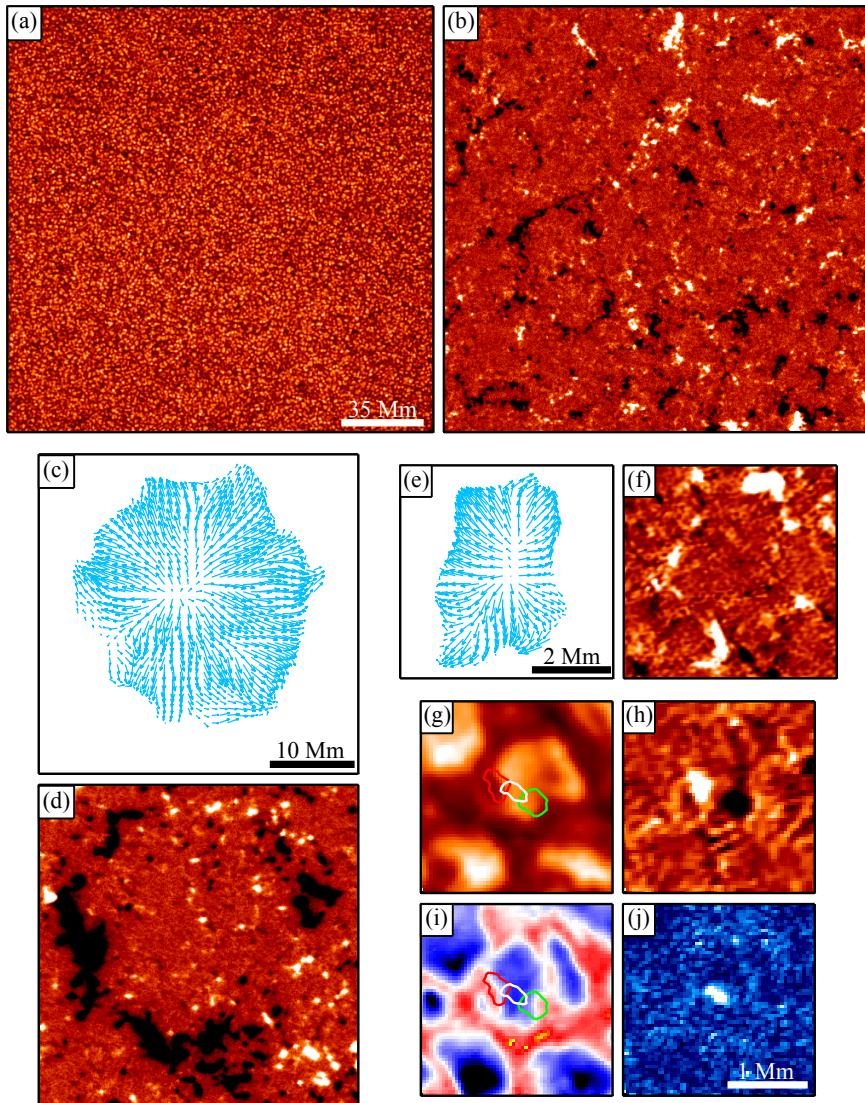


Figure 1.2: Quiet Sun at the disk center as observed by SDO/HMI: (a) continuum intensity; (b) longitudinal magnetogram. Supergranular cell as observed by *Hinode*/NFI (courtesy Milan Gošić): (c) supergranular flow field; (d) longitudinal magnetogram. Mesogranular cell as observed by SUNRISE/IMaX: (e) mesogranular flow field, (e) longitudinal magnetogram. Small-scale Ω -loop as observed by SUNRISE/IMaX: (g) continuum intensity; (h) longitudinal magnetogram; (i) line-of-sight velocity; (j) linear polarization. Red, green, and white contours represent positive polarity, negative polarity, and linear polarization patches, respectively.

1.2.1 Spatial distribution of quiet-Sun magnetic fields

Figure 1.2 shows images from quiet-Sun regions observed with different instruments and spatial resolutions. Panel (a) and (b) display a wide quiet-Sun area at disk center observed with the Helioseismic and Magnetic Imager (HMI; Scherrer et al. 2012) aboard the Solar Dynamics Observatory (SDO; Pesnell et al. 2012) at the spatial resolution of $1''$. The solar surface convection is observed as a granular pattern in the continuum intensity image of panel (a). The co-spatial longitudinal magnetogram illustrates the reticular pattern produced by the magnetic network in panel (b). An individual supergranular cell is shown in Figure 1.2 (c) and (d) as observed with the Narrowband Filter Imager (NFI; Tsuneta et al. 2008) on board the *Hinode* satellite (Kosugi et al. 2007). The panels display the horizontal flow field map of the supergranular cell and the corresponding longitudinal magnetogram, respectively. The horizontal supergranular flow goes from the center of the cell toward its boundary where the network patches are observed. With a spatial resolution of about $0''.3$, many IN magnetic elements are also found in the interior of the magnetic network. Different features of such IN areas are also displayed in panels (e)–(j) with a higher spatial resolution of $0''.15$ – $0''.18$. These images have been acquired with the Imaging Magnetograph eXperiment (IMaX; Martínez Pillet et al. 2011a) aboard the SUNRISE (Barthol et al. 2011) balloon-borne solar observatory. Detailed information of the different panels is given later in the text.

In most places of the solar photosphere the ratio of the gas pressure to the magnetic pressure, the so-called plasma β , is much larger than one. As a result, quiet-Sun magnetic fields are observed to evolve in the solar surface influenced by granular motions. Long-living IN elements move radially toward the network (de Wijn et al. 2008) as they are advected by horizontal supergranular flows (Orozco Suárez et al. 2012). During their migration, IN magnetic elements interact frequently with other structures (de Wijn et al. 2008) and they are continuously being buffeted by neighbouring granules (Manso Sainz et al. 2011), thus producing random motions at shorter time scales. Many magnetic elements disappear inside the IN by cancellations or fading below the detection limit (Gošić et al. 2015), whereas others survive long enough to reach the network (Wang & Zirin 1988; Orozco Suárez et al. 2012; Gošić et al. 2014). The latter ones merge (cancel) with same-polarity (opposite-polarity) network flux concentrations and modify the network flux budget. Using stable longitudinal magnetogram observations with durations longer than 20 hours, Gošić et al. (2014) found that merging processes appear to be dominant. Through this positive net flux contribution, the IN magnetic elements could replace the entire network flux in approximately 1 day.

Between the well-known granular and supergranular convective scales (see e.g., Nordlund et al. 2009; Rieutord & Rincon 2010, for reviews), many observations suggest the

existence of an intermediate scale of convection (5-10 Mm of size, [November et al. 1981](#)) known as mesogranulation ([November et al. 1981](#); [Simon et al. 1988](#); [Title et al. 1989](#); [Brandt et al. 1991](#); [Muller et al. 1992](#); [Roudier et al. 1998](#); [Shine et al. 2000](#); [Leitzinger et al. 2005](#)). Figure 1.2 (e) displays the horizontal velocity flow field of a single mesogranule. It depicts a very similar shape as that of a supergranule, but with one order of magnitude smaller size. Despite many investigations, there is an ongoing debate about whether mesogranulation is a distinct scale of solar convection ([Rieutord et al. 2000](#); [Cattaneo et al. 2001](#); [Domínguez Cerdeña 2003a](#); [Rast 2003](#); [Roudier et al. 2003](#); [Roudier & Muller 2004](#); [Matloch et al. 2009, 2010](#); [Yelles Chaouche et al. 2011](#); [Bushby & Favier 2014](#)). Others suggest them to be persistent granule associations that produce mesogranular-sized positive horizontal flow divergences. Specifically, they have been related to “trees of fragmenting granules” ([Roudier et al. 2003](#); [Roudier & Muller 2004](#)), which consist of a family of repeatedly exploding granules. Regardless of their nature, it has recently become clear that magnetic elements accumulate at mesogranular boundaries ([Yelles Chaouche et al. 2011](#)). Roughly 85 % of the pixels harboring longitudinal fields with values larger than 100 G are located in the near neighborhood of mesogranular lanes. Figure 1.2 (e)–(f) show an example where many magnetic features are observed all around a mesogranule.

Linear polarization patches seem to be also organized on mesogranular scales ([Lites et al. 2008](#); [Danilovic et al. 2010b](#)). Visual evidence has been obtained showing that they are co-spatial with mesogranular boundaries ([Ishikawa & Tsuneta 2010](#)). However, quantitative information of such a relation is still missing. The most exhaustive statistical analysis of the evolution of HIFs has been performed by [Danilovic et al. \(2010b\)](#). They found that these features are preferentially located at the edges of granules, with most of them falling into the intergranular lanes at some point during their evolution. This is consistent with the evolution found for emerging magnetic loops, which appear first within a granule and then are swept into the intergranular lanes ([Centeno et al. 2007](#)). Figure 1.2 (g)–(j) shows an example of one of these Ω -loops emerging above a granule. At the center of panel (h) the two opposite polarity footpoints are observed. These footpoints are connected by a small linear polarization patch in panel (j). Their contours are shown on the continuum intensity and line-of-sight velocity maps, panel (g) and (i) respectively. The loop is rising within a convective upflow as represented by blue areas in the velocity map.

1.2.2 Magnetic field strength and inclination in the IN

The question about whether IN magnetic fields are weak or strong was a matter of a heated debate over the past decade (see e.g., [de Wijn et al. 2009](#); [Bellot Rubio & Orozco Suárez 2015](#), for a review). The discussion was primarily motivated by the contradictory results ob-

tained from ground-based observations when different spectral regions were used. While the field strengths inferred through visible Fe I lines at 630 nm used to favor kG fields (Sánchez Almeida & Lites 2000; Domínguez Cerdeña et al. 2003b,c; Lites & Socas-Navarro 2004), those obtained from near-IR lines used to derive hG fields (Lin 1995; Lin & Rimmele 1999; Khomenko et al. 2003). Theoretical arguments suggested that visible Fe I lines at 630 nm could be affected by the noise (Bellot Rubio & Collados 2003) and crosstalks between the thermodynamic and magnetic parameters (Martínez González et al. 2006). In both cases the reason was attributed to the lower magnetic sensitivity of the visible lines.

The controversy started to be elucidated with the development of new solar instruments with improved angular resolution. Thanks to its unprecedented stability, a major contribution was carried by the Japanese *Hinode* satellite. The Spectro-Polarimeter (SP; Lites et al. 2013) on board *Hinode*'s 0.5-m Solar Optical Telescope (SOT; Tsuneta et al. 2008) performs full Stokes vector spectropolarimetric observations of the Fe I lines at 630 nm with an spatial resolution of $0''.32$. The analysis of these data through Milne-Eddington (ME) inversions of the radiative transfer equation (e.g., Orozco Suárez et al. 2007a,b; Asensio Ramos 2009; Borrero & Kobel 2011; Jin et al. 2012; Orozco Suárez & Bellot Rubio 2012) showed a predominance of hG fields, in agreement with those derived from ground-based measurements of near-IR lines. Same results were found by Martínez González et al. (2008) through the combined inversion of visible and near-IR lines measured simultaneously at the same telescope. These new results reconciled visible and near-IR measurements and a consensus was reached regarding the IN field strength distribution.

The first inversions of the *Hinode*/SP data also revealed a surprisingly large amount of inclined magnetic fields (e.g., Orozco Suárez et al. 2007b; Lites et al. 2008), suggesting that the orientations of IN fields are not isotropically distributed. Soon doubts concerning the reliability of the magnetic parameters inferred from ME inversions appeared. Some authors suggested that the large abundance of horizontal fields could be biased (de Wijn et al. 2009; Asensio Ramos 2009; Borrero & Kobel 2011). Since a large fraction of the analyzed pixels have linear polarization signals dominated by noise, they concluded that most of the weak horizontal fields were not real, but due to noise. These doubts were tackled with both solid theoretical arguments (Del Toro Iniesta et al. 2010) and new high sensitivity *Hinode*/SP measurements (Orozco Suárez & Bellot Rubio 2012). In the latter, they used four times less noisy data and they confirmed the idea that IN fields are weak and very inclined. The magnetic field strength and inclination distributions resulting from this observations are depicted in Figure 1.3. The distributions show that most of the magnetic fields have hG strengths and horizontal inclinations (90°). Interestingly, the field strength distribution extends up to kG values and two little, nearly vertical, humps are observed at inclination values close to 0° and 180° . If the related field strengths are weak, they could

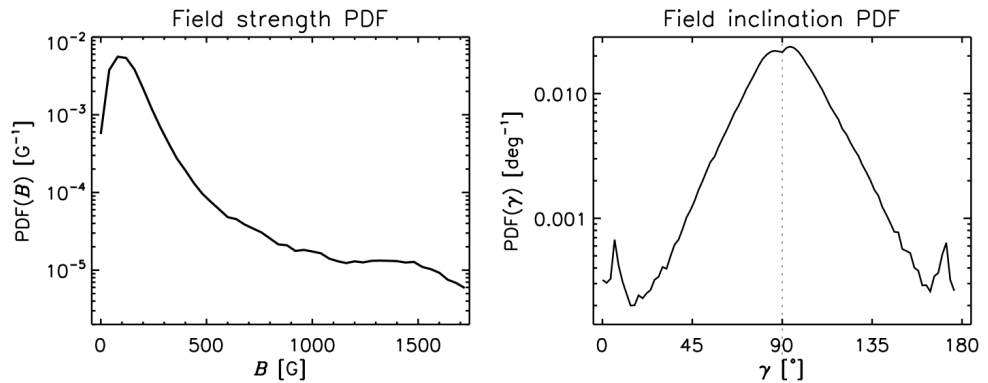


Figure 1.3: Magnetic field strength (left) and inclination (right) probability density functions for internetwork regions resulting from a ME inversion of spectropolarimetric data obtained with the *Hinode*/SP at a noise level of 3×10^{-4} . Only pixels whose Stokes profile amplitude exceeded a polarization threshold of 4.5 times the noise level were included in the analysis. From Orozco Suárez & Bellot Rubio (2012)

be associated with the footpoints of small-scale magnetic loops. If instead their fields are strong, they could be related with kG magnetic elements.

1.2.3 Formation of magnetic elements

The formation of strong magnetic elements is thought to be well understood from a theoretical point of view. Convective eddies expel magnetic fields into intergranular lanes (Weiss 1966). The flux is there concentrated roughly up to the equipartition field strength, ~ 500 G, the level where the magnetic energy density becomes equal to the kinetic energy density of granular flows. The enhanced magnetic pressure suppresses the convective energy transport and the gas cools down inside the flux concentration (Webb & Roberts 1978; Spruit & Zweibel 1979). Attracted by gravity, the dense cool gas sinks down and leads to the partial evacuation of the magnetic feature (*convective collapse*; Parker 1978). The gas pressure drops inside the magnetic element and it is compressed by surrounding plasma. Through this process, the flux concentration is further intensified up to 1–2 kG field strengths (Spruit 1979) and the horizontal pressure balance is again established.

One observation of such an intensification process from equipartition to kG values and a simultaneous strong downflow in a magnetic element has been interpreted as an evidence for a convective collapse (Nagata et al. 2008). Realistic magnetoconvection models show that magnetic fields are advected by convective motions to well localized sinkholes located at the vertices of granular and mesogranular downflow lanes (Stein & Nordlund 2006; Danilovic

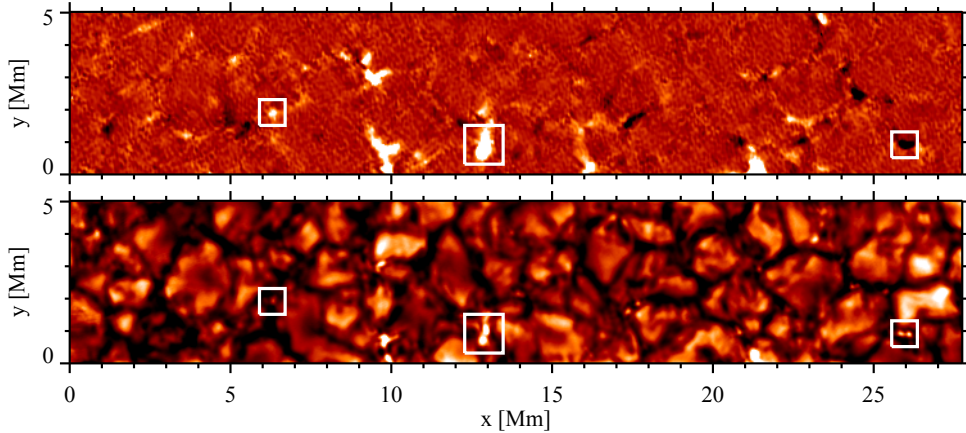


Figure 1.4: Co-spatial images from both the IMAx and SuFI instruments aboard the SUNRISE balloon-borne solar observatory. Top panel: longitudinal magnetogram as observed by IMAx. Bottom panel: CN-band image at 388 nm as observed by SuFI. Examples of magnetic concentrations with associated bright points are marked by white boxes. The left most one shows a small magnetic element with a related BP, while the two right most magnetic features contain two BPs.

et al. 2010a). There, they are concentrated and intensified by converging granules. Observation of the entire process requires high resolution spectropolarimetric images over relatively long time periods. Such observations have recently been achieved with the balloon-borne SUNRISE observatory.

1.2.4 Bright points and magnetic flux tubes

Strong magnetic concentrations in the solar photosphere show up as small point-like bright features in intergranular lanes (e.g., Berger & Title 2001; Sánchez Almeida et al. 2010; Vitić et al. 2010). Figure 1.4 displays a magnetogram co-spatial with a CN-band filtergram. White boxes show three clear examples where magnetic structures appear associated with bright points (BPs). The largest magnetic features can be related with BP groups (see the two rightmost boxes). Based on a recent comparison between SUNRISE observations and 3D magnetohydrodynamical (MHD) simulations, Riethmüller et al. (2014) deduced that BPs are associated with kG magnetic elements.

Magnetic concentrations in the solar surface are generally modeled by magnetostatic *flux tubes* (Spruit 1976). Strong magnetic field inhibits the convective motions and results in a partially evacuated tube (see Section 1.2.3). Since the energy input from below is reduced, the temperature is lower than in the outside plasma at equal geometric height. The gas pressure is also lower in the tube and so is the opacity. Therefore, the optical depth

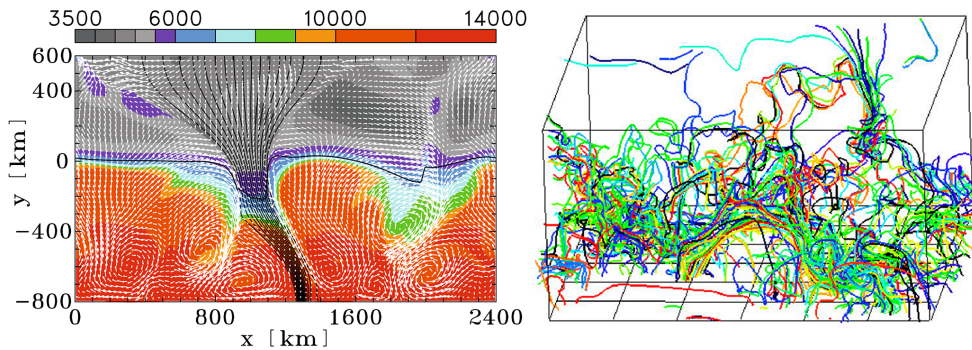


Figure 1.5: Left panel: 2D MHD model of a flux tube. The temperature (background image), the velocity field (arrows), and magnetic field lines (thin lines). The thick horizontal curve indicates continuum optical depth unity. From <http://www.kis.uni-freiburg.de/~steiner/>. Right panel: 3D magnetoconvection simulation. Magnetic field lines of an snapshot viewed from an angle. From [Stein & Nordlund \(2006\)](#)

unity level is depressed inside the tube and it is located at a geometrically deeper layer compared to surrounding plasma (Wilson depression effect). The temperature is higher at deeper layers but still cooler than in the tube at equal optical depth. The less opaque magnetic flux tube also causes a lateral inflow of radiation into their evacuated interiors. This horizontal influx of radiation is sufficient to heat the tube up to a temperature which is higher than the photospheric temperature at the same optical depth. As a consequence, the flux concentration appears brighter than its surrounding material. This is true for small magnetic structures as those found in the quiet Sun. At larger scales, the influx of radiation only heats a thin part of the outer surface, and thus sunspots appear dark in the solar photosphere.

More sophisticated 2D models of flux tubes show that they are far from being static ([Steiner et al. 1996, 1998](#)). The flux tubes are instead very dynamic, they move and bend continuously as they are buffeted by surrounding granules. An example of such a flux tube model is displayed in the left panel of [Figure 1.5](#), where the Wilson depression effect is clearly shown by the horizontal thick black curve, which indicates the location of the continuum optical depth unity. In 3D magnetoconvection simulations, the concept of isolated flux tube is not valid anymore ([Stein & Nordlund 2006](#)). The topology is rather complex, coherent bundles of field lines are only seen at the surface and they are connected to many different locations both below and above the surface (see right panel in [Figure 1.5](#)).

From the observational point of view, BPs have been widely used as proxy diagnostics to study the evolution of magnetic elements (e.g., [Muller & Roudier 1992](#); [Roudier et al. 1994](#); [Berger & Title 1996](#); [de Wijn et al. 2005](#); [Jafarzadeh et al. 2013](#); [Utz et al. 2014](#)). This has been primarily motivated by their small point-like nature which makes them easier

to be tracked compared to the more extended magnetic structures. In addition, intensity tracers are far more easier to be observed at high angular resolution than the associated magnetic features. Discerning the vector magnetic field requires high precision polarimetric measurements only achievable under extremely stable seeing conditions. Molecular lines such as the Fraunhofer G band and CN band have been extensively used due to their high contrast. Those lines are strongly weakened inside flux concentrations and when integrated over the passband the BPs appear much brighter than in continuum images (Kiselman et al. 2001). Intensity tracers have however many limitations as strong flux concentrations are required to form a bright point (Berger & Title 2001; Ishikawa et al. 2007; Riethmüller et al. 2014). This is not, however, a sufficient condition, as many strong magnetic elements do not have a related BP. The contrast of BPs decreases as the inclination angle between the vector magnetic field and the line of sight increases (Beck et al. 2007a). In addition, during their lifetime, magnetic structures can be related to different BPs at different times. The magnetic flux exists before and after the appearance and disappearance of each individual BP (de Wijn et al. 2005). All these restrictions call for the need of sensitive polarimetric observations.

1.2.5 Origin of IN magnetic fields

Whenever there is a continuous injection of magnetic flux at the solar surface, the existence of strong magnetic elements in the convective downflows can be found (Section 1.2.3). The fundamental question now is to know where this flux comes from. One possibility is that the quiet Sun magnetic field is recycled from decaying active regions as the debris fragments of magnetic flux submerge and rise again in other places of the solar surface. In fact, magneto-convection models that study the interaction of convective flows with an imposed magnetic field can reproduce many of the observed quiet-Sun features (e.g., Khomenko et al. 2005; Stein & Nordlund 2006; Bushby et al. 2008), including the concentration of magnetic flux in mesogranular lanes (Stein & Nordlund 2006). If the input field is coming from decaying active regions, then it would be generated by the global solar dynamo and a dependence on the solar cycle would be expected. However, it has been found that IN longitudinal magnetic field shows little correlation with the strength of the surrounding network field (Lites 2011), and also very slight dependence on the sunspot number (Jin & Wang 2015a). In addition, the occurrence rate of linear polarization patches is the same in both the quiet Sun and in plage regions (Ishikawa & Tsuneta 2009). It does not vary along the solar cycle (Jin & Wang 2015b). Another possibility is that IN magnetic fields are generated locally through a small-scale dynamo action driven by near-surface convective flows (Petrovay & Szakaly 1993). The small-scale dynamo can operate on both granular (Cattaneo 1999; Vögler & Schüssler

2007) and mesogranular scales (Bushby et al. 2012; Bushby & Favier 2014; Rempel 2014). However, it is more efficient when mesogranulation is also present (Bushby & Favier 2014). In fact, the photospheric magnetic energy is doubled as a strong mesogranular network is formed (Rempel 2014).

1.3 Motivation of this work

Our understanding of the dynamics and evolution of quiet-Sun magnetic fields has been limited by the need for stable seeing conditions to achieve high spatial resolution together with sufficient stability and polarimetric sensitivity. One possibility to fulfill this requirement is to fly a telescope outside the perturbing action of the Earth atmosphere.

The Imaging Magnetograph eXperiment is a spectropolarimeter with full polarization and imaging capabilities which is designed to fly as a post-focus instrument of the 1-m telescope aboard the SUNRISE balloon-borne solar observatory. It provides nearly diffraction limited observations of the Stokes profiles of the solar photospheric Fe I line at 525.02 nm. Being stratospheric (the balloon reached 40 km of altitude), SUNRISE has been able to get rid of most of the atmosphere, hence improving the image quality. An image stabilization system has maintained the spatial resolution for long periods of time, thus allowing to explore the evolution of photospheric features. With an unprecedented spatial resolution of $0''.15\text{--}0''.18$ (after reconstruction) and high time cadence of 33 s, we have for the first time the opportunity to study the evolution of spatially resolved quiet-Sun magnetic structures (Lagg et al. 2010).

IMaX is already leading new insights into the magnetism and convection of the quiet-Sun photosphere (e.g., Borrero et al. 2010; Bonet et al. 2010; Khomenko et al. 2010; Steiner et al. 2010; Martínez González et al. 2011). The Solar Physics Group at the Instituto de Astrofísica de Andalucía (IAA-CSIC) has participated in the design, development, and construction of IMaX, and on its scientific definition and analysis. The present thesis is devoted to the study of quiet-Sun magnetic fields through the exploitation of these high-quality data. We analyze the evolution of several different quiet-Sun magnetic structures, and we characterize their spatial distribution in the solar photosphere. Specifically, we study 1) the formation and evolution of an isolated magnetic element; 2) the dynamics of multi-core magnetic structures; and 3) the relation between magnetic features and convectively driven, long living sinks at the junctions of several mesogranular cells.

SPECTROPOLARIMETRY

Some basic concepts of spectropolarimetry are introduced in this Chapter. This knowledge of the measurements and analysis of light will be especially useful later in this thesis in order to better understand the inference of physical quantities such as solar magnetic fields and line-of-sight (LOS) velocities. The Chapter includes a mathematical formulation of polarized light, an overview of the spectropolarimetric measurements carried out with the Imaging Magnetograph eXperiment, and a description of the radiative transfer equation in the presence of a magnetic field. For further reading on spectropolarimetry, we refer to [Del Toro Iniesta \(2003\)](#).

2.1 Measurements of polarized light

In a homogeneous isotropic medium, Maxwell's equations ensure that both the electric (\mathbf{E}) and magnetic field vectors, satisfy the homogeneous wave equation

$$\nabla^2 \mathbf{E} - \frac{\epsilon\mu}{c^2} \ddot{\mathbf{E}} = 0. \quad (2.1)$$

The simplest solution for that equation is a plane wave, where the electric and magnetic vectors are orthogonal to each other in the plane perpendicular to the ray path direction. This is a good approximation to more elaborate solutions (e.g., spherical waves) when the observer is far enough from the light source, as is the case for most astrophysical applications. A polychromatic light beam can be described as the superposition of monochromatic (single frequency) plane waves. If the beam propagates through the z-axis, at a given point in the

space, the description of a polychromatic wave can always be put in the form

$$\begin{aligned} E_x(t) &= \mathcal{E}_x(t) e^{-i(\omega t - \delta_x(t))}, \\ E_y(t) &= \mathcal{E}_y(t) e^{-i(\omega t - \delta_y(t))}, \\ E_z(t) &= 0, \end{aligned} \quad (2.2)$$

where $\mathcal{E}_x(t)$ and $\mathcal{E}_y(t)$ represent the amplitudes of each of the x and y components, $\delta_x(t)$ and $\delta_y(t)$ are their phase shifts, and ω the angular frequency. For simplicity hereafter we omit the argument (t) .

These quantities, however, are not measurable with available devices because they are complex, and the polarization properties of any electromagnetic wave is better described by the Stokes parameters:

$$\begin{aligned} I &= \kappa(\langle |E_x|^2 \rangle + \langle |E_y|^2 \rangle) = \kappa\langle \mathcal{E}_x^2 + \mathcal{E}_y^2 \rangle, \\ Q &= \kappa(\langle |E_x|^2 \rangle - \langle |E_y|^2 \rangle) = \kappa\langle \mathcal{E}_x^2 - \mathcal{E}_y^2 \rangle, \\ U &= \kappa(\langle E_x^* E_y \rangle + \langle E_y(t) E_x^* \rangle) = 2\kappa\langle \mathcal{E}_x \mathcal{E}_y \cos \delta \rangle, \\ V &= i\kappa(\langle E_x^* E_y \rangle - \langle E_y E_x^* \rangle) = 2\kappa\langle \mathcal{E}_x \mathcal{E}_y \sin \delta \rangle, \end{aligned} \quad (2.3)$$

where κ is a dimensional constant which translates the Stokes parameters into intensity units, $\langle \rangle$ means time average, $*$ stands for complex conjugate, and $\delta = \delta_x - \delta_y$ is the phase difference between the two components. Note that all four Stokes parameters are real and have dimensions of energy. They are thus measurable and they must obey the inequality: $I^2 \geq Q^2 + U^2 + V^2$. Although not straightforward, the above inequality can be interpreted as a proof that polychromatic light is not always polarized. As a matter of fact, any polychromatic beam can be decomposed in two, one totally unpolarized and another totally polarized, whose energy is given by the right-hand side of the inequality. It can therefore be read as “the energy content of any polychromatic beam is always larger than or equal to the energy content of its polarized component”. When equality holds, light is said to be *totally polarized*, whereas when $Q = U = V = 0$, light is said to be *natural* or *completely unpolarized*. Otherwise, the light beam is said to be *partially polarized*.

In order to measure the Stokes parameters two specific optical devices are needed: a *linear polarizer* and a *linear retarder*. A linear polarizer is a device which selectively allows the passage of completely linearly polarized light at an angle θ . This characteristic angle marks the orientation of the so-called *optical axis* of the linear polarizer. The electric field aligned to the optical axis is completely transmitted; while the orthogonal component is completely absorbed. So that at the output, the magnitude of the new electric beam is given

by:

$$E_\theta = E_x \cos \theta + E_y \sin \theta. \quad (2.4)$$

On the other hand, a linear retarder is an optical device which introduces a *retardance* (phase difference) δ between both orthogonal components of \mathbf{E} associated to the beam. The phase-shifted component is parallel to the so-called *slow axis* and perpendicular to the *fast axis*. If we consider a retarder whose fast axis is aligned with the x-axis of the reference coordinate system, the outgoing E'_x and E'_y are

$$\begin{aligned} E'_x &= E_x, \\ E'_y &= E_y e^{i\delta}. \end{aligned} \quad (2.5)$$

Now, if we consider an optical system having those two devices in a row (first the retarder and then the polarizer), the output electric vector amplitude is given by:

$$E_\theta = E_x \cos \theta + E_y \sin \theta e^{i\delta}, \quad (2.6)$$

and the measurable beam intensity is

$$I_{\text{meas}} = \langle E_\theta E_\theta^* \rangle. \quad (2.7)$$

Making use of the Stokes parameters (2.3), and assuming that $\kappa = 1$, the time-averaged electric field square modulus can be recast in the more useful form

$$I_{\text{meas}}(\theta, \delta) = \frac{1}{2} (I + Q \cos 2\theta + U \cos \delta \sin 2\theta + V \sin \delta \sin 2\theta). \quad (2.8)$$

Accordingly, we can infer I , Q , U and V by just varying θ and δ . This can be done by using different optical devices and setups. In the specific case of our optical system,

$$\begin{aligned} I &= I_{\text{meas}}(0, 0) + I_{\text{meas}}\left(\frac{\pi}{2}, 0\right), & Q &= I_{\text{meas}}(0, 0) - I_{\text{meas}}\left(\frac{\pi}{2}, 0\right), \\ U &= I_{\text{meas}}\left(\frac{\pi}{4}, 0\right) - I_{\text{meas}}\left(\frac{3\pi}{4}, 0\right), & V &= I_{\text{meas}}\left(\frac{\pi}{4}, \frac{\pi}{2}\right) - I_{\text{meas}}\left(\frac{3\pi}{4}, \frac{\pi}{2}\right), \end{aligned} \quad (2.9)$$

since the equations for Q , U , and V are differences, these parameters are zero for the case of natural light. Stokes I is the total intensity, namely, the sum of any two orthogonal polarization states. Polarization information is provided by Q , U , and V . Specifically, Q is the difference between the intensities of linear components at 0° and 90° , U is the difference between the intensities of linear components at 45° and 135° , and V is the difference be-

tween the intensities of right-handed and left-handed circularly polarized light. The Stokes parameters can be grouped in the so-called *Stokes vector*,

$$\mathbf{I} = (I, Q, U, V)^T, \quad (2.10)$$

which describes the polarized state of the light, and T represents the transpose.

2.2 Spectropolarimetry with IMaX

So far we know how to measure the polarization state of light by means of two especially suited devices. Once we know the mathematical basis of the Stokes parameters, we are in a position to introduce a little some real solar spectropolarimetry and, in particular, on that performed by the Imaging Magnetograph eXperiment (IMaX; [Martínez Pillet et al. 2011a](#)). In this Section we will focus on its optical setup, designed for retrieving the full Stokes vector. Further details on IMaX observational properties will be described in Section 3.1.1.

IMaX is an imaging magnetograph capable of obtaining two-dimensional maps of the vector magnetic field and the LOS velocity in a given region of the solar surface. Figure 2.1 shows the optical design of IMaX, which is made up of two main optical parts: the spectrum analyzer, and the polarimeter. The former uses a Fabry–Pérot interferometer based on a LiNbO_3 etalon. The etalon is a double pass, narrow-band tunable filter which achieves a spectral resolution of 8.5 pm. The polarimeter uses two liquid crystal variable retarders (LCVRs) as the polarization modulator and a beamsplitter as the polarization analyzer. This optical configuration and the high Zeeman-sensitive line of Fe I at 525.02 nm used by IMaX allows us to observe the four Stokes parameters at various wavelength points inside the spectral line. The spectral line is sampled in various ways depending on the applied observing mode (see Section 3.1.1). In what follows we introduce the polarization and spectrum analyzers.

2.2.1 Polarimetric analysis

With two conceptually identical LCVRs and a beamsplitter, IMaX is able to produce the modulation schemes needed for measuring the full Stokes vector. As shown in Figure 2.1, the light beam passes through the retarders first and across the beamsplitter later. The LCVRs have their fast axis at 0° and 45° , and they introduce retardances of σ and ρ respectively. The optical axis of the beam splitter is aligned with the vertical direction, and consequently it forms an angle of 0° and 90° for each orthogonal polarization state. Proceeding as in the previous Section, the two perpendicular measured intensities can be represented

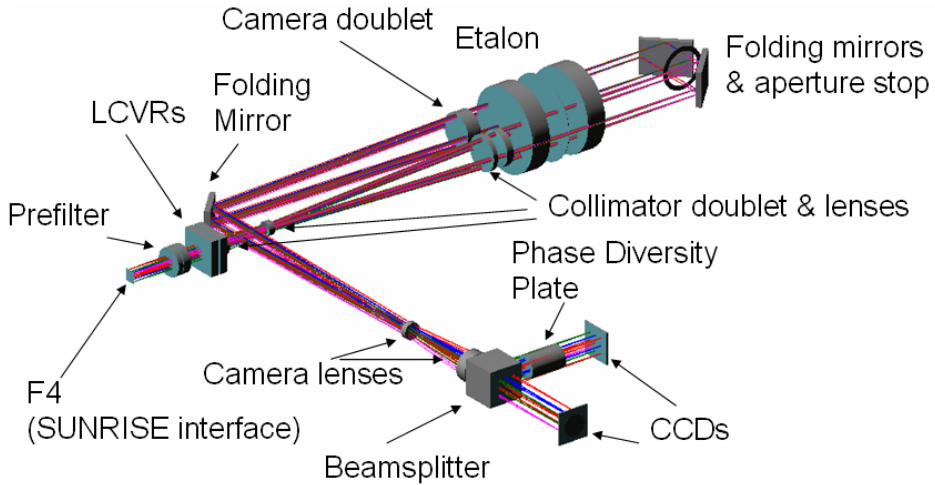


Figure 2.1: IMAx optical design (self-explained). From [Martínez Pillet et al. \(2011a\)](#).

as the following linear combination of the Stokes parameters:

$$\begin{aligned}
 I_{\text{meas},1} &= \frac{1}{2}(I + Q \cos \rho + U \sin \rho \sin \sigma - V \sin \rho \cos \sigma), \\
 I_{\text{meas},2} &= \frac{1}{2}(I - Q \cos \rho - U \sin \rho \sin \sigma + V \sin \rho \cos \sigma).
 \end{aligned}
 \tag{2.11}$$

The LCVRs use voltages in the range of 0–10 V to obtain retardances between 535° and 20° ([Martínez Pillet et al. 2011a](#)). The four Stokes parameters are measured by applying four different combinations of voltages to the LCVRs. In order to maximize the so-called polarimetric efficiency (see [Del Toro Iniesta & Collados 2000](#)) and minimize the switching times of the LCVRs, [Martínez Pillet et al. \(2004\)](#) propose the following retardance values:

$$\begin{aligned}
 (\sigma_1, \sigma_2, \sigma_3, \sigma_4) &= (315, 315, 225, 225), \\
 (\rho_1, \rho_2, \rho_3, \rho_4) &= (305.264, 54.736, 125.264, 234.736),
 \end{aligned}
 \tag{2.12}$$

for the first and second retarders, respectively. As demonstrated by [Martínez Pillet \(2007\)](#) and [Del Toro Iniesta & Martínez Pillet \(2012\)](#), such a combination of retardances enables to reach the theoretically optimum efficiencies. This modulation scheme leads to four inde-

pendent intensity measurements:

$$\begin{aligned} I_1 &= I + \frac{1}{\sqrt{3}}Q + \frac{1}{\sqrt{3}}V + \frac{1}{\sqrt{3}}V, & I_2 &= I + \frac{1}{\sqrt{3}}Q - \frac{1}{\sqrt{3}}V - \frac{1}{\sqrt{3}}V, \\ I_3 &= I - \frac{1}{\sqrt{3}}Q - \frac{1}{\sqrt{3}}V + \frac{1}{\sqrt{3}}V, & I_4 &= I - \frac{1}{\sqrt{3}}Q + \frac{1}{\sqrt{3}}V - \frac{1}{\sqrt{3}}V, \end{aligned} \quad (2.13)$$

which in turn provide all four Stokes parameters as

$$\begin{aligned} I &= \frac{1}{4}I_1 + \frac{1}{4}I_2 + \frac{1}{4}I_3 + \frac{1}{4}I_4, & Q &= \frac{\sqrt{3}}{4}I_1 + \frac{\sqrt{3}}{4}I_2 - \frac{\sqrt{3}}{4}I_3 - \frac{\sqrt{3}}{4}I_4, \\ U &= \frac{\sqrt{3}}{4}I_1 - \frac{\sqrt{3}}{4}I_2 - \frac{\sqrt{3}}{4}I_3 + \frac{\sqrt{3}}{4}I_4, & V &= \frac{\sqrt{3}}{4}I_1 - \frac{\sqrt{3}}{4}I_2 + \frac{\sqrt{3}}{4}I_3 - \frac{\sqrt{3}}{4}I_4. \end{aligned} \quad (2.14)$$

According to Eq. (2.11), two independent determinations of \mathbf{I} are obtained by each camera, the combination of which improves significantly the final signal to noise (S/N) ratio of the observations.

2.2.2 Spectral analysis

The spectral sampling of the Fe I line at 525.02 nm is performed through a Fabry–Pérot interferometer, which is made of a solid LiNbO₃ etalon. As the beam passes through the etalon, it is multiply reflected to produce a multiple-beam interference and maximize the transmission at some wavelengths. Changing the refractive index within by applying an external electric field, the wavelength at which the transmission is highest is modified. Through this process, the line can be scanned in a straightforward way. Telecentric and collimated mountings are two of the most common optical setups adopted for Fabry–Pérot interferometers. IMA_X uses a collimated configuration, which results in a better spectral resolution and image quality than that for the telecentric one (Kentischer et al. 1998). Unfortunately, with this setup, the maximum transmissions are dependent on the incident angle of the ray, and a blueshift over the field of view (FOV) is produced. This issue requires special care with the maximum angle of incidence. The focal length of the collimator guarantees that the angle of incidence on the etalon does not exceed 0.44°, which produces a wavelength drift of 2.8 pm (over the largest circular FOV).

Solid LiNbO₃ etalons have many advantages for their implementation in balloon platforms, such as their low weight and volume. In contrast, their tuning speed is their largest disadvantage. The etalon spends 80 ms tuning the typical step of about 4 pm used by IMA_X (Martínez Pillet et al. 2011a). Since measurements should be carried out in a time shorter than the characteristic variation of solar structures, this limits the number of wavelength samples that are measured.

Finally, an important issue is to reduce the amplitude of the secondary transmission peaks. To this end, the system is also equipped with an interference pre-filter (with a band-pass of 0.1 nm) which strongly reduces their amplitude. The spectral resolution achieved by the instrument is 9.3 pm in a single pass. As the beam goes through the etalon twice the spectral resolution is improved by a factor $\sqrt{2}$ over the single pass case. However, due to the stray light coming from the side lobes, the final effective spectral resolution is degraded to 8.5 pm.

2.3 The radiative transfer equation in a magnetized atmosphere

Now that we are familiar with the propagation of light through different homogeneous optical devices, we can now go a step further and study the propagation of light in an inhomogeneous medium such as the solar photosphere. In particular on that atmosphere permeated by a magnetic field, which makes the medium anisotropic as it breaks the symmetry by introducing a preferential direction. The transport of light through such a medium is governed by the radiative transfer equation (RTE) for polarized light. Following, for instance, the notation in [Del Toro Iniesta \(2003\)](#), the transport of radiative energy through magnetized and plane-parallel anisotropic atmospheres is described by:

$$\frac{d\mathbf{I}}{d\tau_c} = \mathbf{K}(\mathbf{I} - \mathbf{S}) \quad (2.15)$$

where τ_c is the continuum optical depth, \mathbf{S} is the source function vector, and \mathbf{K} is the propagation matrix. Under the local thermodynamic equilibrium (LTE) assumption, $\mathbf{S} = (B_\nu, 0, 0, 0)^T$, where $B_\nu(T)$ is the Planck function at the local temperature, T . All the information about the polarization state of the light is contained in the Stokes vector, $\mathbf{I} = (I, Q, U, V)^T$, while \mathbf{K} and \mathbf{S} include all the medium properties and geometry relevant for the formation of the Stokes spectrum. The propagation matrix \mathbf{K} can be written as:

$$\mathbf{K} = \begin{pmatrix} \eta_I & \eta_Q & \eta_U & \eta_V \\ \eta_Q & \eta_I & \rho_V & -\rho_U \\ \eta_U & -\rho_V & \eta_I & \rho_Q \\ \eta_V & \rho_U & -\rho_Q & \eta_I \end{pmatrix}, \quad (2.16)$$

where

$$\begin{aligned}
\eta_I &= 1 + \frac{\eta_0}{2} \left[\phi_p \sin^2 \gamma + \frac{\phi_b + \phi_r}{2} (1 + \cos^2 \gamma) \right], \\
\eta_Q &= \frac{\eta_0}{2} \left[\phi_p - \frac{\phi_b + \phi_r}{2} \right] \sin^2 \gamma \cos 2\varphi, \\
\eta_U &= \frac{\eta_0}{2} \left[\phi_p - \frac{\phi_b + \phi_r}{2} \right] \sin^2 \gamma \sin 2\varphi, \\
\eta_V &= \frac{\eta_0}{2} [\phi_r - \phi_b] \cos \gamma, \\
\rho_Q &= \frac{\eta_0}{2} \left[\psi_p - \frac{\psi_b + \psi_r}{2} \right] \sin^2 \gamma \cos 2\varphi, \\
\rho_U &= \frac{\eta_0}{2} \left[\psi_p - \frac{\psi_b + \psi_r}{2} \right] \sin^2 \gamma \sin 2\varphi, \\
\rho_V &= \frac{\eta_0}{2} [\psi_r - \psi_b] \cos \gamma.
\end{aligned} \tag{2.17}$$

γ and φ represent the inclination angle (with respect to the propagation direction) and the azimuth angle (with respect to the Stokes Q positive direction) of the vector magnetic field, respectively. η_0 stands for the ratio between the line and continuum absorption coefficients, and it depends on two thermodynamic variables: temperature, T , and density, ρ , or the electron pressure, p_e , through the Boltzmann and Saha equilibrium population equations. $\phi_{p,b,r}$ and $\psi_{p,b,r}$ are the absorption and dispersion profiles, where p,b,r indices stand for the π , σ_b and σ_r components of the “normal” Zeeman triplet. In the most general case, when we account for the “anomalous” Zeeman effect, the absorption and dispersion profiles can be cast as a sum of as many Zeeman components as those allowed by quantum mechanics:

$$\begin{aligned}
\phi_\alpha &= \frac{1}{\sqrt{\pi}} \sum_i S_{\alpha,i} H(u, a), \\
\psi_\alpha &= \frac{1}{\sqrt{\pi}} \sum_i S_{\alpha,i} F(u, a).
\end{aligned} \tag{2.18}$$

$S_{\alpha,i}$ stand for the strength of each Zeeman component and are proportional to the transition probability, with $\alpha = +1, 0, -1$, or b,p,r, referring to three different polarization states, namely, linearly polarized light along the vector magnetic field and circularly polarized light (left- and right-handed) in the plane perpendicular to the vector magnetic field. $H(u, a)$ and $F(u, a)$ are the Voigt and Faraday-Voigt functions:

$$\begin{aligned}
H(u, a) &= \frac{a}{\pi} \int_{-\infty}^{\infty} e^{-y^2} \frac{1}{(u-y)^2 + a^2} dy, \\
F(u, a) &= \frac{1}{\pi} \int_{-\infty}^{\infty} e^{-y^2} \frac{u-y}{(u-y)^2 + a^2} dy,
\end{aligned} \tag{2.19}$$

where $u = u_0 - u_{\text{LOS}} + u_{B,\alpha,i}$. These three variables are dimensionless and they are defined as:

$$u_0 = \frac{\lambda - \lambda_0}{\Delta\lambda_{\text{D}}}, \quad u_{\text{LOS}} = \frac{\lambda_0 v_{\text{LOS}}}{c \Delta\lambda_{\text{D}}}, \quad u_{B,\alpha,i} = -\frac{\Delta\lambda_{B,\alpha,i}}{\Delta\lambda_{\text{D}}}. \quad (2.20)$$

λ_0 is the central wavelength of the spectral line, c is the speed of light and v_{LOS} the plasma bulk velocity along the LOS. $\Delta\lambda_{\text{D}}$ is the Doppler width, which accounts for the broadening of the spectral line due to the Doppler effect produced by the thermal motions of atoms and ions and it is related to the temperature, T , of the medium by

$$\Delta\lambda_{\text{D}} = \frac{\lambda_0}{c} \sqrt{\frac{2kT}{m} + v_{\text{mic}}^2}, \quad (2.21)$$

where k is the Boltzmann constant and m the rest mass of the atom. v_{mic} is the so-called microturbulence velocity, which is an *ad hoc* parameter introduced for accounting for those motions on smaller scales than the mean free path of photons. Last but not least, $\Delta\lambda_{B,\alpha,i}$ is the wavelength shift of the different Zeeman components due to the Zeeman splitting, and it is related to the magnetic field strength, B , by

$$\Delta\lambda_{B,\alpha,i} = \frac{e\lambda_0^2 B}{4\pi m c^2} (M_{l,i}(g_l - g_u) - \alpha g_u), \quad (2.22)$$

where e and m stand for the charge and mass of the electron; l and u are the lower and upper levels of the transition, M is the magnetic quantum number, and g is the *Landé* factor of each Zeeman sublevel involved in the transition.

At this point, it is worth noting that the physical quantities of the medium such as the temperature, T , the LOS velocity, v_{LOS} , and the vector magnetic field (B , γ and φ) among others are included in the propagation matrix and in the source function. Knowing the atmospheric parameters from where a given solar spectral line is formed, we could in principle solve the RTE and obtain the Stokes parameters of the outgoing light beam. However, what we measure with spectropolarimeters like IMA X is nothing but the Stokes parameters of the polarized light. Therefore, what we have to solve is the inverse problem. The medium properties are obtained from the measured Stokes spectrum. This is a formidable problem, but fortunately resolvable, as we shall see in Section 3.2.

INSTRUMENTATION, DATA AND ANALYSIS

The study of quiet-Sun magnetism demands high spatial and temporal resolution, along with polarimetric sensitivity and accuracy. Magnetic fields in the solar photosphere are shown as structures up to the smallest observable scales, and their evolution is found to be highly dynamic (e.g., [de Wijn et al. 2009](#)). We use observations from the SUNRISE balloon-borne solar observatory which allows to resolve magnetic structures with sizes of about 100 km, up to the diffraction limit of the 1-m telescope. Being a stratospheric mission, it gets rid of most of the turbulent Earth's atmosphere, which provides nearly seeing-free imaging conditions.

In this Chapter, we describe the SUNRISE mission and its two main post-focus instruments, the data that we use for this thesis, and the method applied for inferring the physical quantities at the solar surface.

3.1 SUNRISE stratospheric balloon-borne solar observatory

The SUNRISE stratospheric balloon-borne solar observatory ([Solanki et al. 2010](#); [Barthol et al. 2011](#)) consists of a 1-m Gregory-type reflector telescope with two post-focus science instruments: the Imaging Magnetograph eXperiment (IMaX; [Martínez Pillet et al. 2011a](#)), a spectropolarimeter, and the SUNRISE Filter Imager (SuFI; [Gandorfer et al. 2011](#)), a multi-channel UV filter imager. During the whole observation time the science images of both instruments are coaligned and stabilized by the Correlating Wavefront Sensor (CWS; [Berkefeld et al. 2011](#)), and the Image Stabilization Light Distribution (ISLiD; [Gandorfer et al. 2011](#)) unit, respectively. The latter also allows simultaneous observations by distributing the radiation according to the wavelength of each instrument (525.05 nm IMaX; 200–400 nm SuFI).



Figure 3.1: SUNRISE before launch in ESRANGE on 2009 June 8. From [Barthol et al. \(2011\)](#).

SUNRISE flew on a zero-pressure helium balloon in the frame work of NASA’s Long Duration Balloon program. The first science flight was successfully launched on 2009 June 8 from ESRANGE near Kiruna (northern Sweden). Figure 3.1 shows and image of the gondola payload and the partly filled balloon just before launch. It then traveled westward for almost six days over the Arctic Circle at a mean cruise altitude of 36 km, and landed on Somerset island (northern Canada) on 2009, June 13. Figure 3.2 shows the trajectory of the SUNRISE flight. The Sun was extremely quiet at that time, and essentially all of the data correspond to internetwork regions with a few network elements.

3.1.1 IMaX: the Imaging Magnetograph eXperiment

The Imaging Magnetograph eXperiment, IMaX, is an imaging spectropolarimeter with full Stokes vector capabilities at the Zeeman-sensitive Fe I line at 525.02 nm (Landé factor $g = 3$; [Martínez Pillet et al. 2011a](#)). It contains two main optical parts: a spectrograph, and a polarimeter. The spectrograph consists of a double pass LiNbO₃ etalon and narrow band pre-filter (with a FWHM of 0.1 nm) to achieve a spectral resolution of 8.5 pm. The polarimeter performs fast polarization modulation, based on two liquid crystal variable retarders, and dual-beam polarization analysis that, together with the spectrograph, allows to obtain the

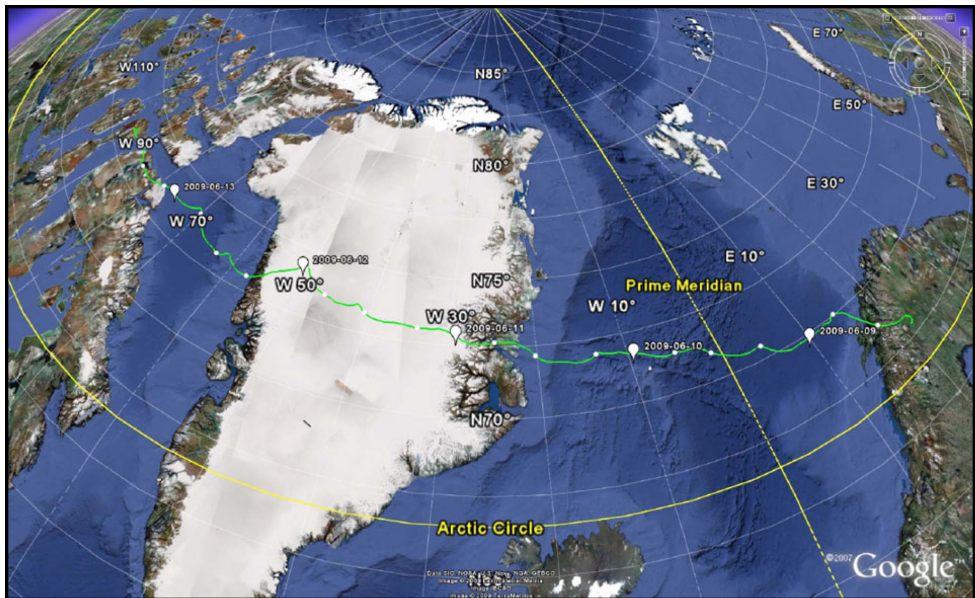


Figure 3.2: SUNRISE flight trajectory from Kiruna in northern Sweden to Somerset island (northern Canada). From [Barthol et al. \(2011\)](#).

four Stokes parameters in various wavelength positions. Such measurements were discussed with some detail in Section 3.2.

During the flight different observing modes were used according to the acquired number of wavelengths (N_λ), accumulations (N_A), and polarization states. Three spectral observing modes with 2, 4 and 11 points inside the spectral line plus one at the nearby continuum were used. An observing mode is called vectorial (labeled V) if all the four Stokes parameters are measured, while a longitudinal mode (labeled L) only cares about circular polarization, namely, only Stokes I and V are measured. Table 3.1 lists all the IMAx observing modes used during the first SUNRISE flight. Labels at the left column represent the polarization states (V and L) followed by wavelengths number (N_λ) and accumulation number (N_A).

The light beam is divided into two orthogonal polarization states by the beamsplitter. The images are recorded in two synchronized 1024×1024 pixels CCD cameras, with a spatial sampling of $0.055 \text{ arcsec pixel}^{-1}$. After every observing run, a thick glass plate is inserted into the light path in front of one of the cameras to acquire a set of 30 in-focus and out-of-focus image pairs for post-facto phase diversity (PD) reconstruction ([Gonsalves 1982](#); [Paxman et al. 1996](#)). Before data reduction, several procedures were used for dark-current subtraction, flat-field correction, and polarization cross-talk removal. Through the PD inversion technique, the point-spread function (PSF) is retrieved and the science images

Table 3.1: IMaX observing modes during the first SUNRISE flight.

Observing mode	Cadence (s)	Line samples (pm)	Continuum (pm)
V5-6	33	-8, -4, +4, +8	+22.7
V5-3	18	-8, -4, +4, +8	+22.7
V3-6	20	-6, +6	+22.7
L3-2	8	-6, +6	+22.7
L12-2	31	-19.25 to +19.25 each 3.5	+19.25

are reconstructed by deconvolving this PSF from the originally recorded images. The process requires an apodization that effectively reduces the IMaX field of view (FOV) down to about $43'' \times 43''$. The spatial resolution has been estimated to be $0.''15\text{--}0.''18$ after reconstruction. The noise level in each Stokes parameter is about 3×10^{-3} in units of the continuum intensity, and the rms contrast of the quiet-Sun granulation obtained from continuum data is about 13.5 % (Solanki et al. 2010), which testifies to the outstanding quality of IMaX images. For more information on IMaX we refer the reader to the paper by Martínez Pillet et al. (2011a).

3.1.2 SuFI: the SUNRISE Filter Imager

The SUNRISE Filter Imager, SuFI, provides images at violet and near ultraviolet wavelengths. It consists of a filter wheel with five filters and a mechanical shutter for exposure control (Gandorfer et al. 2011). The wavelengths sampled are: 214 nm (FWHM ~ 10 nm), 300 nm (FWHM ~ 5 nm), 312 nm (FWHM ~ 1.2 nm), CN-band head at 388 nm (FWHM ~ 0.8 nm), and core of Ca II H at 396.8 nm (FWHM ~ 0.18 nm). However, only the CN-band and Ca II H images are used in this thesis.

A 2048×2048 pixels UV-enhanced CCD, with a spatial sampling of 0.0207 arcsec pixel $^{-1}$ is employed. Focused images are acquired on one half of the detector, while the other half receives an image with a defocus of one wave at 214 nm, which results in a FOV of $13'' \times 38''$. This strategy is used for post-facto PD reconstruction (Hirzberger et al. 2011).

The time cadence varies depending on the light level entering SuFI and the number of filters used. The light level decreases towards shorter wavelengths, and hence the exposure time varies from 1 s (at 396.8 nm) to 30 s (at 214 nm). The typical time cadence ranged between 2–12 s whenever the 214 nm filter was not included. A detailed description of SuFI is given by Gandorfer et al. (2011).

3.2 Diagnostics of physical quantities

We have already seen that IMAx was designed for measuring the Stokes profiles that emerge from the solar atmosphere. The formation of these profiles are well described by the RTE for polarized light (see Section 2.3). This equation shows that the Stokes spectrum depends on the physical properties of the medium. In particular, the atmosphere is specified by a number of physical parameters and their stratification at different optical depths. Typically, the temperature, T , the electron pressure, p_e , the microturbulence velocity, v_{mic} , the LOS velocity, v_{LOS} , the magnetic field strength, B , inclination, γ , and azimuth, φ , are included. This set of parameters forms the so-called *model atmosphere*, which can be represented by a vector,

$$\mathbf{x}(\tau_c) = [T(\tau_c), p_e(\tau_c), v_{\text{mic}}(\tau_c), v_{\text{LOS}}(\tau_c), B(\tau_c), \gamma(\tau_c), \varphi(\tau_c), v_{\text{mac}}(\tau_c)], \quad (3.1)$$

where v_{mac} is the macroturbulence velocity, an ad-hoc parameter that accounts for turbulent motions that are not resolved by the spatial resolution element.

For a given model atmosphere, we can solve the RTE and obtain the synthetic Stokes profiles. This is not, however, a straightforward task and we are not going to enter into the details here. For the description of various numerical solutions, we refer the reader to [Landi Degl'Innocenti \(1987\)](#), [Rees et al. \(1989\)](#), [Bellot Rubio et al. \(1998\)](#), and [Semel & López Ariste \(1999\)](#).

3.2.1 The inversion problem

The fundamental problem in solar physics is the inference of the physical quantities that describe the different processes taking place in the solar atmosphere. Unfortunately we do not have the ability to directly measure the magnetic, dynamic, and thermal properties of the solar features. Rather, what we measure is nothing but the (polarized) light that escapes from the Sun. Therefore, we have to content with indirect inferences of the physical parameters retrieved through the Stokes profiles. The simplest approach is that of a direct comparison between synthetic and observed profiles, where the model atmosphere is modified randomly until a good match is obtained. This is however inefficient when the number of free parameters increases or a large amount of data is used. Hence, automatic procedures are highly desirable. The inversion codes deal with this problem through automatic minimization of the mean quadratic distance between the synthetic and the observed Stokes spectrum given

by a merit function such as

$$\chi^2(\mathbf{x}) = \frac{1}{\nu} \sum_{s=1}^4 \sum_{i=1}^{N_\lambda} \frac{[I_s^{\text{obs}}(\lambda_i) - I_s^{\text{syn}}(\mathbf{x}, \lambda_i)]^2}{\sigma_{s,i}^2} w_s^2, \quad (3.2)$$

where ν represents the number of degrees of freedom, namely, the difference between the number of observables ($4N_\lambda$) and the free parameters (the number of elements in \mathbf{x} , n). Indices s and i scan the four Stokes parameters and the wavelength samples, respectively. The measured uncertainties are given by $\sigma_{s,i}$ and w_s are arbitrary weights for the different Stokes profiles. $I_s^{\text{obs}}(\lambda_i)$ and $I_s^{\text{syn}}(\mathbf{x}, \lambda_i)$ are the observed and synthetic Stokes profiles, respectively.

In order to obtain a physically meaningful model atmosphere, \mathbf{x} , an absolute minimum of the merit function has to be found. This is not trivial as the merit function is a non-linear function in an n -dimensional space. In addition, it may have several local minima, which further increase the problem. In the next section we briefly introduce one of the most successful inversion codes that has been applied to photospheric Stokes profiles.

3.2.2 SIR: Stokes Inversions based on Response functions

The Fe I spectral line at 525.02 nm that IMAx observes is formed in the solar photosphere. In this layer the density is high enough that LTE approximation turns out to be a satisfactory approach. The LTE hypothesis assumes that the collision rates between material particles are frequent enough that the energy level populations of atoms depend only on local values of temperature and density. Hence, the local number of absorbers and emitters in the various quantum states are given by the Boltzmann and Saha population equations.

The SIR inversion code ([Ruiz Cobo & del Toro Iniesta 1992](#)) solves the RTE to compute the synthetic Stokes profiles under the assumption of LTE and for plane-parallel atmospheres. The code uses the Levenberg-Marquardt algorithm to modify the initial model and find the absolute minimum of the merit function. The method is actually a combination of the gradient descent method and the Gauss-Newton method. When the parameters are far from their optimal value the algorithm acts more like the gradient-descent method, which takes large steps down the gradient but it is inaccurate in the final convergence. When the solution is close to the minimum then the Gauss-Newton method is used, which takes small steps down to the minimum.

SIR deals with the full stratification of the model parameters. The number of free parameters is reduced by evaluating perturbations to the different model quantities at a few depth grid points called *nodes*. The nodes are used for perturbing the whole atmosphere through a polynomial spline interpolation. For example, when a single node is used, the whole atmosphere is modified by a constant; if two nodes are selected, the atmosphere is

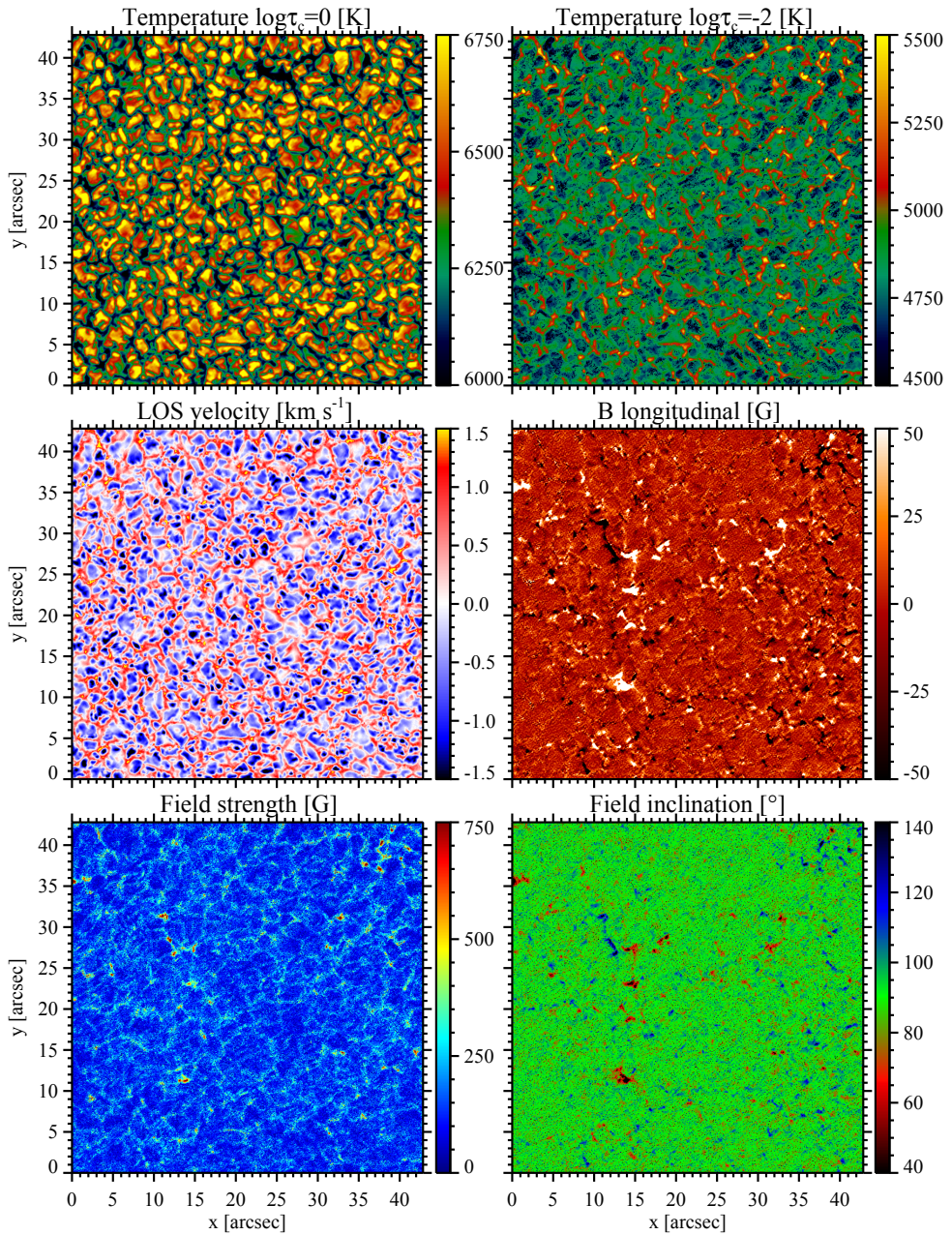


Figure 3.3: Results of the SIR inversions for the data taken by SUNRISE/IMaX on 2009 June 9 at 00:37:09 UT. See text for details.

perturbed by a straight line passing through the perturbations at the nodes; the perturbation is parabolic when the number of nodes is equal to three, and so on. *Equivalent* response functions are calculated to include the sensitivity of all depth grid points (see Ruiz Cobo & del Toro Iniesta 1994). The equivalent response functions are linear combinations of the response functions at all the grid points so that the information from the whole atmosphere is used. For further reading on the SIR code, we refer the reader to Ruiz Cobo & del Toro Iniesta (1992), Del Toro Iniesta & Ruiz Cobo (1996) or Del Toro Iniesta (2003).

Inversion strategy

We initialize the code with the Harvard-Smithsonian Reference Atmosphere (Gingerich et al. 1971, with added magnetic and velocity parameter values). We perform a Milne-Eddington-like approach, which assumes that the magnetic field strength B , the inclination and the azimuth angles γ and ϕ , the LOS velocity v_{LOS} , and the microturbulent velocity v_{mic} are constant with depth. Due to the high spatial resolution of the data, the magnetic filling factor, f (which specifies the fraction of the pixel filled with magnetic field), is assumed to be unity and the macroturbulent velocity v_{mac} is set to zero. From B and γ we also derive the longitudinal component of the magnetic field $B_{\text{long}} = B \cos \gamma$ (longitudinal magnetogram). The temperature T , is modified with two nodes located at the first and last point of the stratification ($\log \tau_c = 1.4$ and -4.0), where τ_c is the continuum optical depth at 500 nm. We estimate the noise-induced uncertainty in the field strength and LOS velocity by repeating the inversions with 100 different realizations of added noise (with amplitudes of $3 \times 10^{-3} I_c$) to the observed Stokes profiles. The standard deviation of all these values is 150 G and 150 m^{-1} respectively.

Figure 3.3 shows an example of the physical parameters resulting from the SIR inversions of the IMaX data. From top to bottom and left to right, we show the temperature at $\log \tau_c = 0$ and $\log \tau_c = -2$, the LOS velocity, the longitudinal component of the magnetic field, the field strength, and inclination. At $\log \tau_c = 0$ the temperature resembles the solar granulation, where hot and cold areas correspond to granules and intergranules respectively. Upper in the photosphere, at $\log \tau_c = -2$, the granulation temperature is reversed, and the hottest regions outline a mesogranular size network. In the LOS velocity image downflows (redshifts) are shown in red and outflows (blueshifts) in blue. The longitudinal magnetogram makes it evident the mixed polarity nature of the quiet-Sun magnetic fields. The largest structures have stronger field strength and they are more vertical than the weakest ones.

THE HISTORY OF A QUIET-SUN MAGNETIC ELEMENT

Isolated flux tubes are considered to be fundamental magnetic building blocks of the solar photosphere. Their formation is usually attributed to the concentration of magnetic field to kG strengths by the convective collapse mechanism. However, the small size of the magnetic elements in quiet-Sun areas has prevented this scenario from being studied in fully resolved structures. Here we report on the formation and subsequent evolution of one such photospheric magnetic flux tube, observed in the quiet Sun with unprecedented spatial resolution ($0''.15$ – $0''.18$) and high temporal cadence (33 s). The observations were acquired by the Imaging Magnetograph Experiment aboard the *SUNRISE* balloon-borne solar observatory. The equipartition field strength magnetic element is the result of the merging of several same polarity magnetic flux patches, including a footpoint of a previously emerged loop. The magnetic structure is then further intensified to kG field strengths by convective collapse. The fine structure found within the flux concentration reveals that the scenario is more complex than can be described by a thin flux tube model with bright points and downflow plumes being established near the edges of the kG magnetic feature. We also observe a daisy-like alignment of surrounding granules and a long-lived inflow towards the magnetic feature. After a subsequent weakening process, the field is again intensified to kG strengths. The area of the magnetic feature is seen to change in anti-phase with the field strength, while the brightness of the bright points and the speed of the downflows varies in phase. We also find a relation between the brightness of the bright point and the presence of upflows within it.

4.1 Introduction

The interaction between convection, radiation, and magnetic field in the electrically conducting solar plasma leads to the creation of a rich variety of magnetic structures. Many of these have kG field strengths and range in size from the largest sunspots, tens of Mm in size, down to the smallest network and internetwork structures, i.e., “magnetic elements” on spatial scales of 100 km or less. The observations of decaying sunspots into smaller structures as well as the formation of pores from the accumulation of smaller magnetic features, has led to the notion that magnetic elements are fundamental entities of magnetic flux from which larger structures are assembled (see, e.g., [Solanki 1993](#); [de Wijn et al. 2009](#), for reviews).

The formation of magnetic elements is thought to be well understood from a theoretical point of view. It is generally accepted that the first step in producing such flux tubes is the *flux expulsion* mechanism. As suggested by [Parker \(1963\)](#) and [Weiss \(1964, 1966\)](#), the magnetic flux is advected by horizontal flows and concentrated in convective downflow areas, roughly up to the equipartition field strength (300–500 G), for which the magnetic energy density equals the kinetic energy density of the gas flow. These equipartition flux concentrations reduce the convective heat transfer, leading to super adiabatic cooling ([Webb & Roberts 1978](#); [Spruit & Zweibel 1979](#)). This evacuates the flux tube, in such a way that the gas pressure of the surrounding plasma compresses the flux concentration until kG field strengths are reached ([Parker 1978](#); [Spruit 1979](#)). This process is known as *convective collapse*, which is thought to be the fundamental step of flux-tube creation.

Later, numerical studies revealed further details of the final state of the magnetic feature. [Hasan \(1985\)](#) found that non-adiabatic effects arising from the radiative exchange between the flux tube and the external medium lead to overstable oscillations as the final state of a collapsed flux tube. On the other hand, [Takeuchi \(1999\)](#) reached a static solution, and showed that if the downflow in a collapsing flux tube becomes strong enough, an upward-traveling shock can develop as the downward flow bounces back in the dense deeper layers. This “rebound shock” reverses the magnetic flux intensification, and may lead to the dissolution of the magnetic flux concentration.

All these results are based on one-dimensional calculations, and rely on the thin flux-tube approximation. [Grossmann-Doerth et al. \(1998\)](#) made use of two-dimensional numerical simulations to study the interaction between the surrounding convective flow and the flux tube. They were the first to find the rebound shock solution for initial field strengths of 400 G. However, this result changes when the initial field is weaker, for which the flux sheet reaches a stable state rather than being dispersed. [Steiner \(1999\)](#) used similar numerical simulations and found a more “quiescent phase” during the time period between the formation of a magnetic flux tube and its dissolution or reformation. During this phase the

magnetic field strength remains quite constant and the flux tube exhibits small internal gas motions. As a consequence of the interaction with the surrounding granular convection, the flux concentration moves laterally, bending and swaying, gets “squeezed”, and during most of the time is bordered by strong, narrow downflows. These strong downflows get narrower with depth and accelerate strongly until they evolve into “jets” (Steiner et al. 1998). They are maintained by the cooling of the gas surrounding the flux concentration through radiative heat losses into the magnetic structure (Deinzer et al. 1984). More recently, Kato et al. (2011) carried out two-dimensional radiation MHD simulations, and showed that these downflow jets can indeed excite a downflow within the magnetic flux concentration, which rebounds and develops into an upward-travelling shock front. Through this mechanism, the atmosphere within the tube oscillates at the acoustic cutoff frequency. Furthermore, Jess et al. (2012) found that upwardly propagating acoustic waves are ubiquitous in quiet-Sun magnetic bright points and 3D MuRAM (Vögler et al. 2005) simulations.

From an observational point of view, spectropolarimetric evidence of convective collapse and subsequent destruction of magnetic flux by an upward-moving front in the quiet Sun was reported by Bellot Rubio et al. (2001). Magnetic flux intensification events have also been observed with the *Hinode* Spectro-Polarimeter. First, a single event by Nagata et al. (2008), where a strong downflow is detected while field strength intensifies and a bright point appears followed by a transient upflow, and then, a statistical analysis of 49 convective collapse events by Fischer et al. (2009).

The interaction between magnetic fields and convection is important to understand the formation and evolution of magnetic structures on the solar surface. Muller et al. (1989) observed that the presence of isolated Network Bright Points (NBPs) disturbs the surrounding granules which elongate in the direction of the magnetic features, forming a characteristic “daisy-like” structure. This granular pattern is formed as the small bright point appears while the surrounding granules converge (Muller & Roudier 1992). Bellot Rubio et al. (1997, 2000) found from the inversion of full Stokes profiles of the Fe I 630 nm lines that magnetic flux tubes in facular regions are surrounded by intense downdrafts, and suggested that these downdrafts produce downflows of lesser magnitude in the tube interior. Close to small magnetic flux concentrations, Rimmele (2004) observed strong, narrow ($<0''.2$) downflow plumes at the edge of many small flux tubes, while there was little gas motion inside the flux concentration, confirming earlier results showing almost unshifted Stokes V zero-crossing in network and plage regions (Solanki 1986; Martínez Pillet et al. 1997).

Isolated magnetic elements are the key to understanding a variety of solar structures, like plages, or the network. Unfortunately, these basic units are generally so small that they have mainly been studied using indirect techniques, either through the interpretation of Stokes spectra of the unresolved feature, or using their association to G-band bright

points. Recently, the Imaging Magnetograph eXperiment (IMaX; [Martínez Pillet et al. 2011a](#)) launched on board the SUNRISE balloon-borne solar observatory ([Solanki et al. 2010](#); [Barthol et al. 2011](#); [Berkefeld et al. 2011](#)) allowed photospheric quiet-Sun magnetic flux tubes to be spatially resolved even in the quiet Sun ([Lagg et al. 2010](#); [Martínez González et al. 2012b](#)).

Here, we take advantage of these unprecedented high quality observations to report on the formation and evolution of a small kG flux concentration and its interaction with the surrounding granulation. The data suggest that the magnetic element is formed by advective coalescence of small-scale flux patches and a subsequent convective collapse phase. Once formed, the evolution of the mature flux tube is much more complicated than that explained by static flux-tube models. Many different phenomena are involved, namely: converging granules and granular fragments, downflow jets, bright points (BPs), oscillations in all basic physical quantities, small-scale upflow plumes, etc.

4.2 Observations and data analysis

We analyze disk center quiet-Sun IMaX spectropolarimetric observations. The data set was obtained on 2009 June 9, 00:36:03–00:58:46 UT. IMaX measured the full Stokes vector in five wavelength positions across the Fe I 525.02 nm line (Landé factor $g = 3$) at $\lambda = -8, -4, +4, +8,$ and $+22.7$ nm from the line center (V5-6 mode). The temporal cadence of a full observing cycle is 33 s, with a pixel size of $0''.055$.

IMaX data reduction routines were used for dark-current subtraction, flat-field correction, and polarization crosstalk removal. The blueshift over the field of view (FOV) produced by the Fabry-Pérot interferometer is corrected in the inferred velocity values. The applied restoration technique requires an apodization that effectively reduces the IMaX FOV down to about $43'' \times 43''$. The spatial resolution has been estimated to be $0''.15$ – $0''.18$ (after reconstruction), and the noise level in each Stokes parameter is about 2.5×10^{-3} in units of the continuum intensity. The rms contrast of the quiet-Sun granulation obtained from IMaX continuum data is around 13.5%, which testifies to the high quality of the SUNRISE/IMaX images. For further details about data reduction, we refer to [Martínez Pillet et al. \(2011a\)](#).

We obtained maps of the mean circular polarization averaged over the line, V_s , and of the mean linear polarization signal, L_s , given respectively by

$$\begin{aligned} V_s &= \frac{1}{4\langle I_c \rangle} \sum_{i=1}^4 \varepsilon_i \cdot V_i, \\ L_s &= \frac{1}{4\langle I_c \rangle} \sum_{i=1}^4 \sqrt{Q_i^2 + U_i^2}, \end{aligned} \tag{4.1}$$

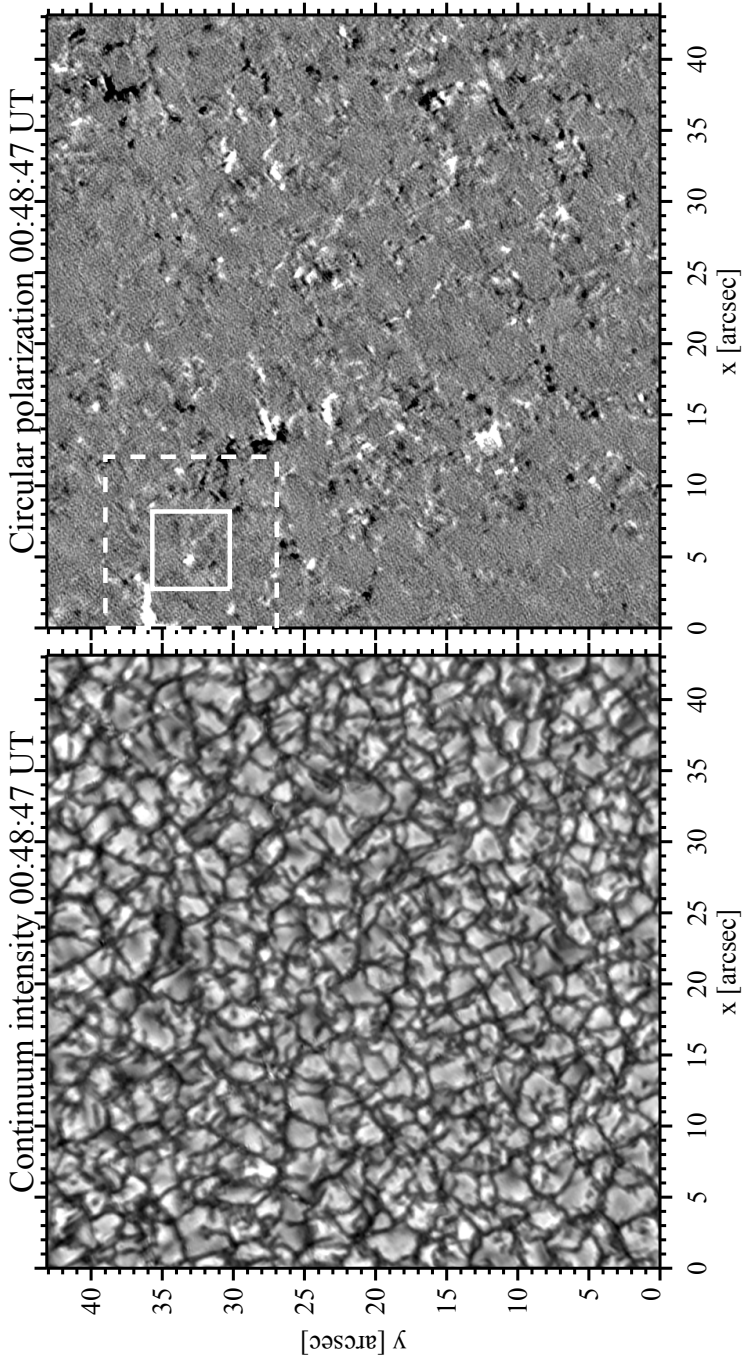


Figure 4.1: Left panel: Continuum intensity map, I_c . Right panel: Map of the mean circular polarization signal V_S with a scale range of $[-1, 1]\%$ of the I_c , covering the FOV of IMAx of about $43'' \times 43''$. The dashed-line square, with a FOV of $12''.1 \times 12''.1$, indicates the location whose continuum intensity has been aligned by cross-correlating two consecutive images. The inner solid line square, with a FOV of $5''.5 \times 5''.5$, indicates the subregion where the magnetic element is studied in detail, as shown in the sequences displayed in Figures 4.2, 4.4, and 4.6.

where $\langle I_c \rangle$ is the continuum intensity averaged over the IMAx FoV, $\varepsilon = [1, 1, -1, -1]$ and i runs over the first four wavelength positions. In the weak field regime, V_s very approximately scales with the longitudinal magnetic component, while L_s is a measure of the transverse (horizontal) component of the magnetic field.

We carried out inversions of the Stokes vector observed with IMAx using the SIR code (Ruiz Cobo & del Toro Iniesta 1992). This code, based on the Levenberg-Marquardt algorithm, numerically solves the radiative transfer equation along the line of sight under the assumption of local thermodynamic equilibrium and minimizes the difference between the measured and the computed synthetic Stokes profiles using response functions.

Using two nodes at which the temperature is explicitly determined, the inversion yields the temperature stratification in the range $-4.0 < \log \tau_c < 0$ through inter- and extra-polation, where τ_c is the continuum optical depth at 500 nm. However it is worth noting that with only 5 wavelength points and a single, very temperature dependent spectral line, the temperature is not constrained reliably in layers above $\log \tau_c = -1.5$ or -2 (depending on the type of feature and the strength of the line). We also obtain the height-independent magnetic field strength B , the inclination and azimuth angles γ and ϕ , the LOS velocity, and the microturbulent velocity, using one node for each of them. The magnetic filling factor is assumed to be unity and the macroturbulent velocity is set to zero due to the high spatial resolution of the data.

Figure 4.1 displays a map of the mean circular polarization for the FoV covered by the observations, about $43'' \times 43''$ over a quiet region at disk center. It shows many internetwork flux concentrations along with stronger and larger flux elements probably belonging to the network.

After applying a p-mode subsonic filter (Title et al. 1989) to the continuum intensity and LOS velocity maps, we focus on a smaller area of $12''.1 \times 12''.1$, indicated by the white dashed-line square in Figure 4.1. On this subfield, we aligned the continuum intensity maps by applying a cross-correlation technique on two consecutive images. The same displacement correction was also applied to the other parameters of interest. Finally, we restricted ourselves to study an even smaller area of $5''.5 \times 5''.5$, displayed by the white solid-line square in Figure 4.1. Within this area, we constructed movies of the continuum intensity, LOS velocity, circular polarization, and field strength, and we obtained horizontal velocity maps of the first three parameters time averaged over a given interval by using the local correlation tracking (LCT) technique (November 1986) as implemented by Molowny-Horas & Yi (1994). This technique selects small sub-fields around the same pixel in contiguous frames, and correlates them to find the best-match displacement. The sub-fields are defined by a Gaussian tracking window with a full width at half maximum (FWHM) of $0''.3$. In order to help the algorithm, the original images are interpolated in time (linearly) and space

(bi-linearly) so that the pixel size and cadence is reduced to $0''.028$ and 11 s respectively. These interpolations do not add any significant information and therefore do not change the results. They only help to get less noisy velocity maps. An example of such horizontal velocity maps is shown in Figure 4.3 which is discussed later in Section 4.3.

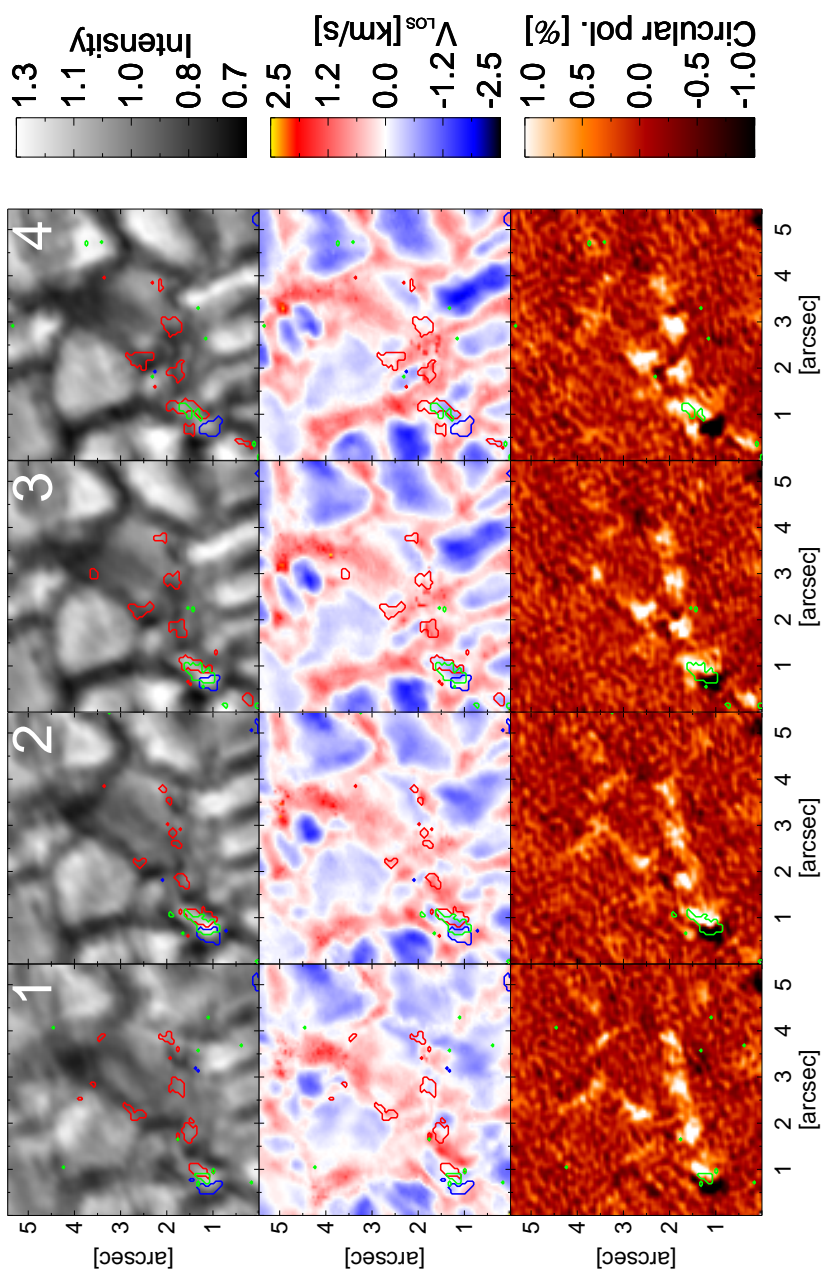
4.3 Flux concentration

Figure 4.2 displays a temporal sequence of the continuum intensity I_c normalized to the average value over the IMAx FoV, the LOS velocity retrieved with SIR, and the circular polarization V_s maps. Note that not all frames in the figure are consecutive. The sequence describes the first phase in the magnetic structure's evolution, mostly characterized by the rise of a small-scale magnetic flux loop and the granular dragging of its footpoints to nearby intergranular lanes. The high and constant spatial resolution of the data allows us to trace the dynamics of sub-arcsecond magnetic patches. We use this property to track the advection of polarization signal by the horizontal plasma flows. Red and blue contours encircle areas with positive and negative circular polarization respectively, whereas green contours indicate regions with a significant linear polarization signal.

In frame 1, at coordinates $[0''.75, 1''.25]$ there is a small-scale loop (Martínez González et al. 2007; Martínez González & Bellot Rubio 2009; Danilovic et al. 2010b) with a bipole flux of 4×10^{16} MX and a field strength peak of 300 G above a pre-existing granule.¹ Two opposite-polarity footpoints are connected by a quite strong L_s signal between them. A statistical study of granular scale loops has already been carried out by Martínez González et al. (2012a), using these IMAx data. From the same SUNRISE science flight, Guglielmino et al. (2012) reported on the evolution of a larger, intermediate-scale, magnetic bipole.

Here, the evolution of the loop can easily be followed in the subsequent V_s frames. The footpoints move from within the granule to nearby intergranular lanes. This motion represents a phase of flux expulsion. At the same time, the Ω -shaped loop is rising as witnessed by the progressive disappearance of the L_s signal (the loop top) while the footpoints stay in the photosphere. Therefore, the underlying granule not only helps to bring the loop to higher layers but also advects the footpoints to the intergranular lanes. At frame 6, the negative footpoint disappears, which is more likely due to cancellation with an opposite polarity patch appearing from frame 2 to 5 at coordinates $[0''.75, 1''.5]$, just above the negative footpoint. Note that the weakening of the L_s signal occurs when flux is cancelling, hence suggesting that cancellation also contributes to the disappearance of L_s . This cancellation of

¹Unless otherwise stated, fluxes are calculated throughout the Chapter by considering the area enclosed by contours of $V_s = 8 \times 10^{-3}$. Field strength values are calculated as averages over 3×3 pixel boxes to reduce the influence of noise.



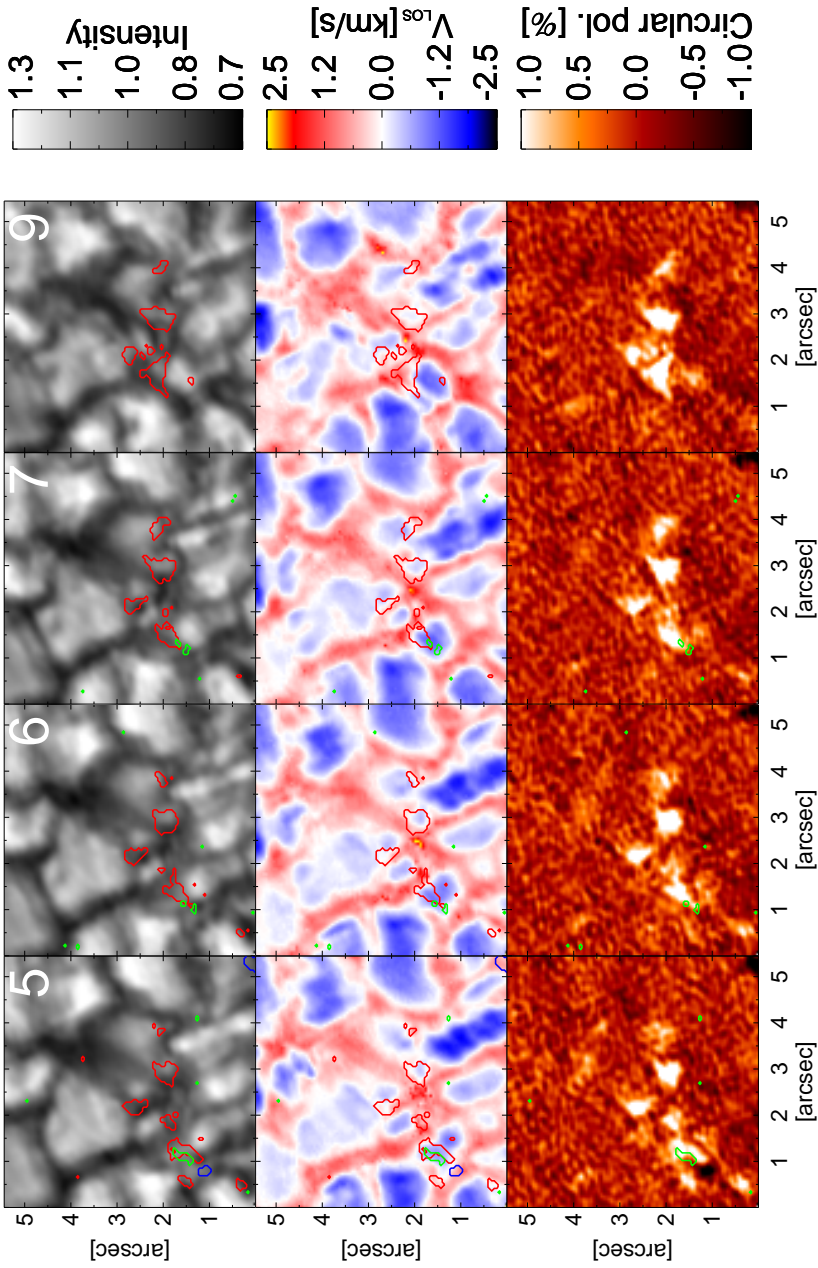


Figure 4.2: Temporal sequence of the continuum intensity maps (top rows), LOS velocity (middle rows), and total circular polarization V_s (bottom rows) during the flux concentration phase. Red (blue) contours over the maps represent a circular polarization signal of +0.8% (-0.8)% of the I_c , and green contours represent a linear polarization signal of 0.8% of the I_c . The elapsed time between consecutive frames is 33.25 s (except between the last two frames), and runs from left to right and continues in the lower set of panels, as numbered in continuum intensity maps. This figure is also available within Animation 1 in the electronic edition of [Requerey et al. \(2014\)](#).

opposite-polarity magnetic patches should be related with some form of magnetic reconnection, in a similar way as the strong blueshift events first observed by Borrero et al. (2010) using the same IMAx data. In fact, the supersonic upflow associated with this particular magnetic cancellation event is visible in the beginning of Animations 1 and 3 at coordinates $[5'', 33'']$ in Borrero et al. (2010). These quiet-Sun jets have been confirmed in *Hinode*/SP data (Martínez Pillet et al. 2011b), and their relation with horizontal field patches have been highlighted by Quintero Noda et al. (2013).

By the time the positive footpoint moves towards the intergranular lane and the negative one is canceled, three additional patches of positive V_s have appeared in contiguous convective downflow areas (frame 9 in Figure 4.2). The whole evolution (frames 1 through 21) of those small magnetic features can be followed in the Animation 1 included in the electronic edition of Requerey et al. (2014). As expected from the small sizes of these magnetic patches, they move along intergranular lanes driven by the horizontal displacement of the granules. This dragging of magnetic patches, gives rise to a number of merging and splitting processes, which result in a bigger and stronger magnetic structure at the end of this phase (frame 21 in the animation). As a result, the magnetic element carries a flux of 5×10^{17} Mx with a field strength peak of 600 G. Note that this and other field strength values given in this work are lower limits, since the inversion assumes filling factor unity. We can call these later stages of evolution as “flux concentration by granular advection”.

Figure 4.3 displays the horizontal velocity maps inferred by the LCT and averaged over this phase (~ 11 minutes, frames 1-21). The flows derived from the circular polarization show motions of magnetic features. On the other hand, the flows derived from the brightness and the LOS velocities show the evolution of granulation with time. The Gaussian tracking window with a FWHM of $0''.3$ could allow us to infer flows at a sub-granular scale. However, as we are averaging over a time period (21 frames, 11 minutes) much longer than that expected for the lifetime of internal convective velocities, the evolution of granules is the dominant contributor to these horizontal flows. This is supported by Verma et al. (2013), which presented rigorous testing of LCT algorithm by comparing its results with velocities in an MHD simulation. In particular, they found that proper motions of single granules are well captured when flow maps are averaged over 15 and 30 minutes, and claim that even with very narrow sampling windows and short time cadences, recovering details of the plasma flows might be unreliable.

The proper motions of continuum intensity and LOS velocity illustrate how granules converge towards the center of the maps where the strongest magnetic flux concentration is found. The circular polarization map shows that the small magnetic patches also move in the same direction as the granules, so that the magnetic flux is concentrated in the center of the map. Any motion of magnetic features then simply implies a motion caused by the evolution

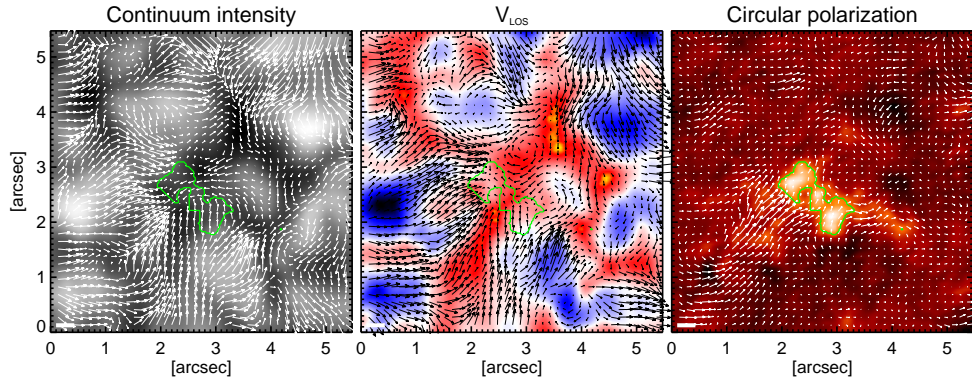


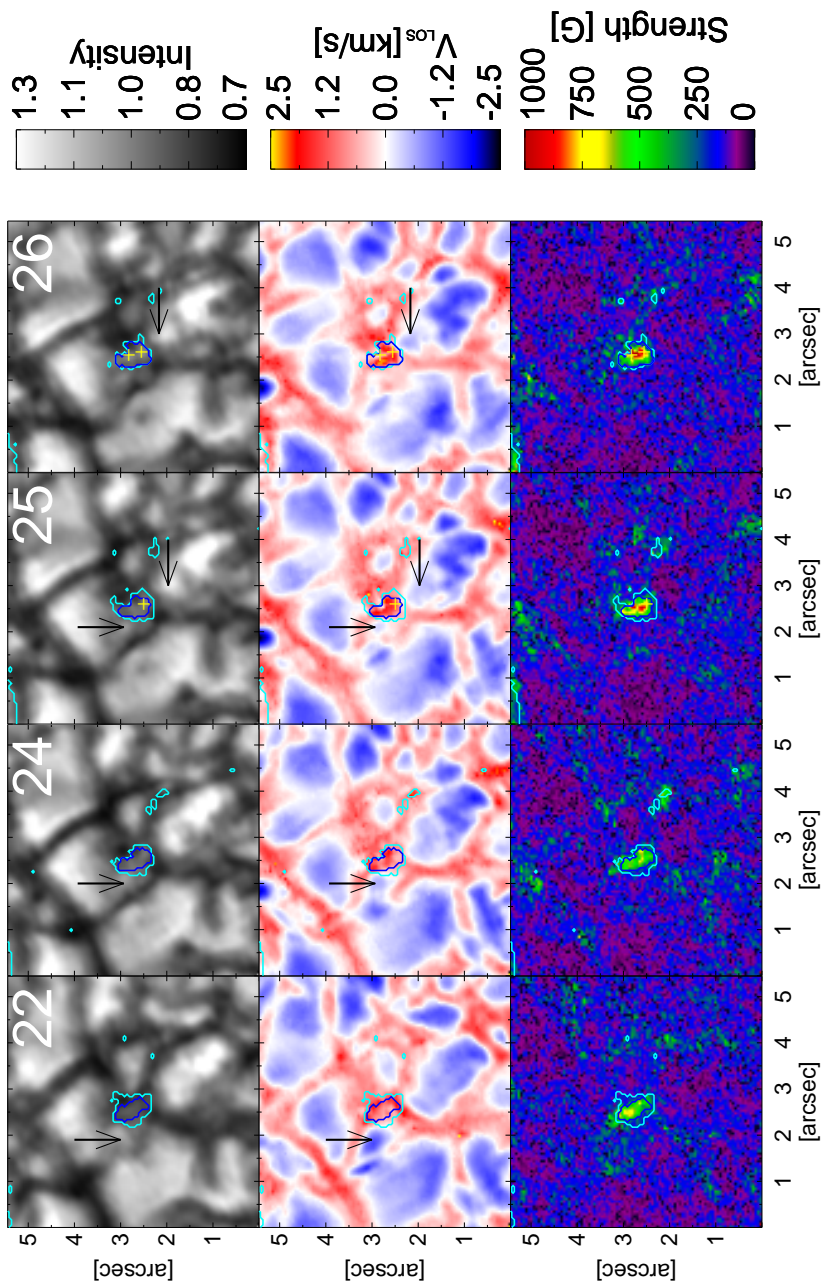
Figure 4.3: Horizontal velocity maps derived through the LCT technique averaged over the flux concentration phase (~ 11 minutes, frames 1-21). Proper motions of the parameters shown in Figure 4.2 are displayed. From left to right: continuum intensity, LOS velocity, and mean circular polarization. The images are averaged in time over this phase. The length of the white bar at coordinates (0.1,0.1) corresponds to 1.8 km s^{-1} . Green contours over the averaged maps represent a circular polarization signal of $+0.5\%$ of the I_c .

of granulation. Thus, the magnetic features can stay within the lanes all the time and still move dragged by these flows. Therefore, Figure 4.3 is indicative of flux concentration by granular advection.

In summary, we can say that this phase encompasses four clear stages, namely, a) the rise of an Ω loop within a granule; b) the expulsion of footpoints towards nearby intergranular lanes; c) flux cancellation of one of the footpoints with an opposite-polarity patch, likely through a reconnection process; and d) the increase of flux in the other footpoint by merging with pre-existing patches of the same polarity, driven by granular advection.

4.4 Formation of a kiloGauss magnetic flux tube

Figure 4.4 shows the formation of a small kG flux concentration. In frame 22 there is a small magnetic patch formed during the flux concentration phase described above. The magnetic structure has field strengths of about 400 G with a maximum value up to roughly 600 G in its center. These strengths are of the order of the typical equipartition field strength (300-500 G) for granules. Note that only eight of the total twelve frames of this convective collapse phase are shown. From top to bottom, rows correspond to continuum intensity, LOS velocity, and magnetic field strength. Overplotted are contours defining the magnetic element. The innermost, blue one corresponds to a region of constant magnetic flux. The external, cyan contour marks regions with longitudinal field components stronger than 60 G.



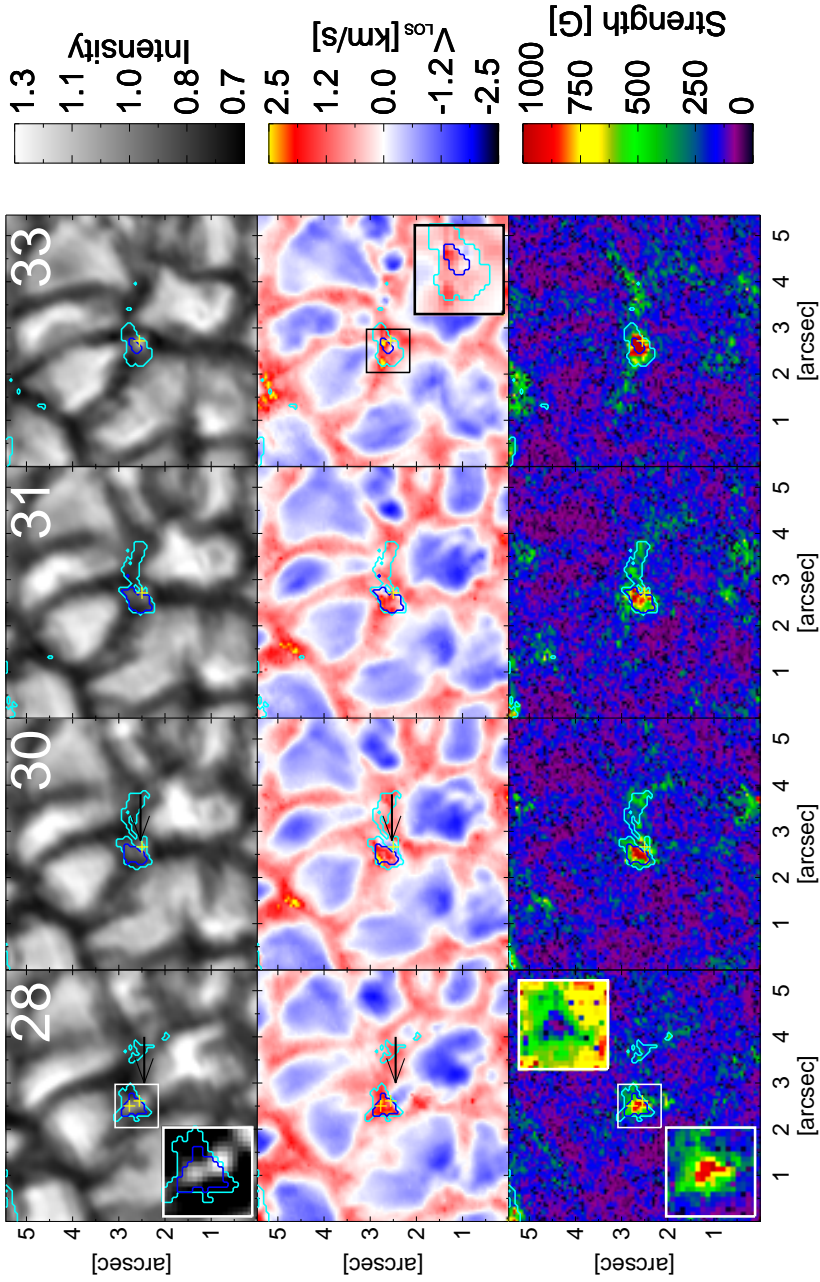


Figure 4.4: Same as Figure 4.2, during the formation of a kiloGauss magnetic element phase. Note that here the bottom rows show field strength maps instead of circular polarization. Cyan line represents iso-magnetic flux density contours of 1×10^{15} Mx. Blue line delineates regions containing a time-constant magnetic flux of 3.5×10^{17} Mx. The yellow cross marks show the bright points location, and the arrows point to small-scale converging upflow features. White boxes in frame 28 display a zoom of the magnetic element for continuum intensity (saturated to $[0.9, 1.1] I_c$), field strength and inclination; the latter is saturated to $[20, 120]$ degrees. The black box in frame 33 displays a zoom of the LOS velocity saturated to $[-5, 5] \text{ km s}^{-1}$. This figure is also available within Animation 1 in the electronic edition of Requerey et al. (2014).

These two contours will be used until the end of the present study. In the three bottom rows, inserts display zooms of the little squares containing the magnetic structure near the centres of the frames. In the case of the velocity insert in frame 33, the scale is doubled (from -5 to $+5 \text{ km s}^{-1}$) in order not to have saturated colors. Two inserts are plotted for the magnetic field strength in frame 28: the bottom one shows a blow-up of the field strength while the top one displays a map of the magnetic inclination in order to illustrate that indeed the magnetic element resembles a fully resolved, canonical flux tube where and almost vertical ($\sim 20^\circ$) inner core is surrounded by more inclined ($\sim 70^\circ$), canopy-like magnetic fields. The outer, 60-G contour is mostly used to illustrate how very small magnetic patches, external to our main structure at the beginning of this phase, progressively increase in size and are advected by granules until they merge with our structure in frame 31.

Let us concentrate now on the constant-flux region enclosed by the inner contour. It encloses a magnetic flux of $3.5 \times 10^{17} \text{ Mx}$ during this evolution phase. As shown in the first frame, this magnetic patch is embedded in an intergranular lane. As time goes on, the area enclosed by this contour decreases sharply while downward motions and field strengths increase within it until kG fields are reached. To quantitatively analyze the evolution in detail, we select the magnetic core of the structure as the centroid of field strengths within the above-mentioned constant-flux contour. The upper panel of Figure 4.5 displays the LOS velocity (crosses and black line), the magnetic field strength (asterisks and red line), and the continuum intensity (diamonds and green line) of such a magnetic flux tube core and the area (triangles and blue line) of the constant flux region. To increase the S/N in the magnetic core physical parameters, we represent averages over the core itself and its eight surrounding pixels. Although not explicit in the axis legends, areas are measured in Mm^2 and multiplied by 10 so that they can be read with the same scale as LOS velocities. Labels in the upper horizontal axis corresponds to frame numbers. The vertical dashed line corresponds to the end of this phase, at frame 33, 6.1 minutes after its start. At this moment the magnetic field reaches strength up to 1.6 kG, compared with the initial 600 G, while the downflow has grown from 0.9 km s^{-1} to 1.5 km s^{-1} . To estimate the noise-induced uncertainty in the field strength and LOS velocity, we repeated the inversions with 100 different realizations of added noise to the observed Stokes profiles. Amplitudes of $10^{-3} I_c$ were used. The standard deviation of the 100 results is 100 G and 100 m s^{-1} . Note that the area of the whole magnetic structure runs in almost anti-phase to the strength of the magnetic core, decreasing from 0.11 to 0.03 Mm^2 . This indicates that magnetic flux is conserved and that the flux contribution of the canopy fields is not very significant, as expected.

In general, the continuum intensity also seems to gradually increase as the field strength intensifies. However, in this case, there is no clear correlation, i.e, the peak intensity is

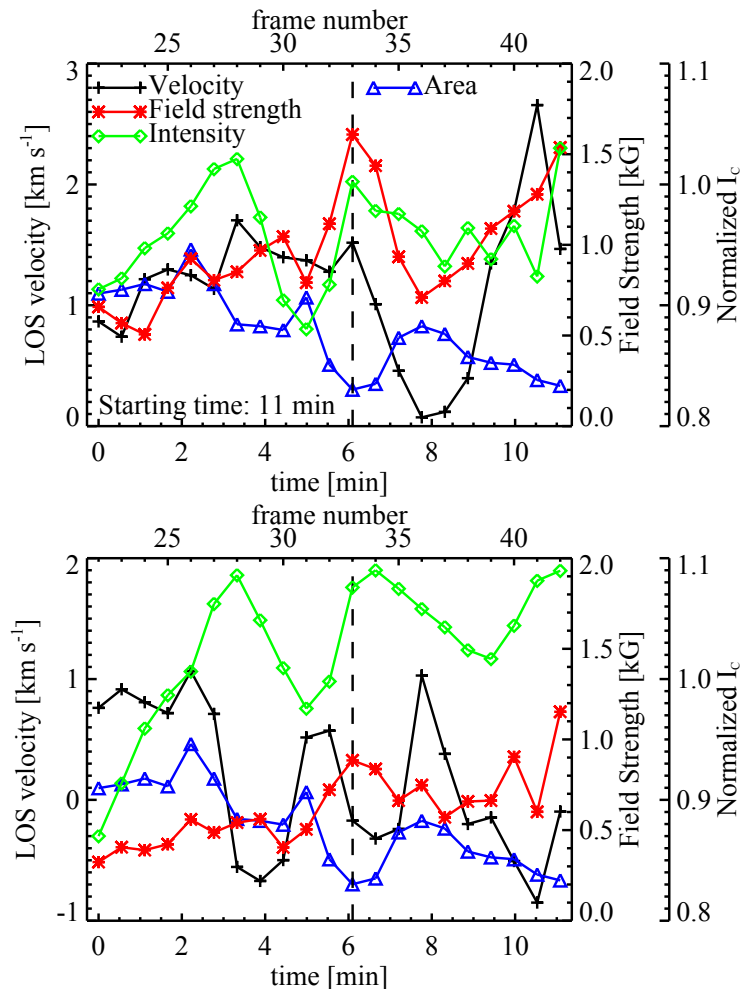


Figure 4.5: Evolution of LOS velocity (black line with plus symbols), field strength (red line with asterisks), and continuum intensity (green line with diamonds), of the flux tube core (Figure 4.5a) and one of the bright points (Figure 4.5b), for frames 22-42. The flux tube core is defined by the blue contour shown in Figures 4.4 and 4.6, which contains a constant magnetic flux of 3.5×10^{17} Mx. We display the evolution of the flux tube core area (blue line with triangles) in both a and b panels. The area is measured in Mm^2 , and we use the same y-axis as the one for LOS velocity. Note that the area has been multiplied by a factor 10 for better visualization. In addition, a value of 1 is subtracted from it in panel b. The physical parameters are extracted by averaging over 9 pixels around the centroid of the magnetic core and bright point for the panels respectively. The dashed vertical line indicates the end of the convective collapse and the beginning of an oscillation phase. Time 0 in the x-axis corresponds to 11 minutes after the observations started, as marked in the Figure. The upper x-axis at the top of each panel mark the frame numbers as shown in Figures 4.4 and 4.6.

reached before the field strength has attained its maximum. The change in brightness will be studied in more detail in Section 4.4.2.

4.4.1 Converging granules and small-scale upflow features

From the LOS velocity maps in Figure 4.4, the presence of two small-scale upflows at the periphery of our magnetic element are evident. These upflows lie above the estimated uncertainties. We mark them using small arrows in the I_c and LOS velocity maps.

The first of those features is indicated by a downward arrow from frame 22 to 25. It is a small upflow fragment detached from a bigger granule. It cools down quickly as it converges towards the magnetic structure. It completely disappears before the strongest downward velocities can be observed in the interior of the flux concentration from frame 26 on.

The feature indicated by the left pointing arrow, in frames 25-30, begins as a typical granule-shaped upflow located close to the magnetic structure. As it evolves, it splits in two. The fragment closer to the magnetic element starts to converge towards the flux concentration, while the other half shrinks and brightens. The converging fragment breaks up as it “collides” against the magnetic flux tube. These fragments are also seen in continuum intensity maps. In neither case do we observe the penetration of the features into the magnetic element as they do in Sobotka et al. (1999) for pores. In addition to these fragmenting processes, the granules as a whole continue converging and dragging small magnetic patches towards the center of the map where the magnetic flux concentration is located. In frames 30 through 33, one can see that small upflowing fragments detached from the upper central and upper right granules to our structure approach the small magnetic feature while it coalesces into our magnetic element as we commented on in Section 4.4.

Besides the above mentioned convergence, the shapes of the granules get perturbed by the presence of magnetic fields. In particular, they lengthen in the direction of the magnetic element and the new weak magnetic feature, thus adopting a “petal-like” appearance whose sharpest corner points towards the magnetic tube. All together, and surrounding the magnetic element, a characteristic “daisy-like” granular pattern (Muller et al. 1989; Muller & Roudier 1992) is observed at the end of the phase (frame 33 in Figure 4.4).

The sum of the above observations makes it seem as if the flux tube behaved as a sink, which attracted the surrounding convective upflows. This effect is clearly observed in Animation 1, included in the electronic edition of the journal. There are two effects that may contribute to this seeming attraction. Firstly, magnetic elements provide a larger surface area through which radiation can escape and hence the surrounding gas be cooled (Spruit 1976). This leads to more vigorous convection (Deinzer et al. 1984). Secondly, this magnetic ele-

ment is located at the intersection of a number of granules, where convective downflows are often particularly strong, so that horizontal flows tend to go towards them. Also, magnetic elements are often located near the centres of vortices that pull the nearby granules towards them (e.g., [Bonet et al. 2008, 2010](#)), which may also contribute.

4.4.2 Bright points inside the flux tube

On the continuum intensity maps in [Figure 4.4](#), two small-scale BPs are glimpsed inside the magnetic flux tube. The BPs appear as the downflow and field strength increase in the interior of the magnetic element and they are indicated by two yellow plus symbols. They can best be discerned in the insert zoom of the continuum intensity map of frame 28, the scale ranges from 0.9 to 1.1 I_c in order to enhance their contrast. It is worth noting that these BPs are smaller than the magnetic element. Hence, unlike the usual assumption, neither one can be identified with a single flux tube.

The BPs are first located close to the core of the magnetic element (frame 26) and, consequently, can be associated with the flux tube's evacuation. Although not exactly coincident with the core of the magnetic element, the uppermost one is close enough for its brightness evolution to be responsible for most of the continuum intensity variation we see in [Figure 4.5 \(a\)](#). Until the BP disappears in frame 29, its brightness correlates fairly well with the magnetic field strength intensification. Note, however, that at this point in time the field is still comparatively weak, since this is still prior to the convective collapse. The disappearance is almost simultaneous to the merging of the main magnetic element considered here with smaller magnetic patches mentioned in the first paragraph of [Section 4.4](#). The second BP (the one closer to the canopy) remains observable until the end of the time series. Thus, we can follow the evolution of its continuum intensity, LOS velocity, and magnetic field strength as calculated from an average of the nine-pixel box centered on the BP brightness centroid. Such an evolution is displayed in [Figure 4.5 \(b\)](#). Starting from frame 25, the BP gets closer and closer to the lower edge of the magnetic element as the granules and small granular fragments converge on the magnetic structure. The lowermost upflow feature described in [Section 4.4.1](#) arrives at the same time to that edge, thus producing a reversal in LOS velocity. Simultaneously, the continuum intensity reaches its peak (1.1 I_c ; frame 28). Later, the intensity starts to decrease as the small upflow breaks up and the magnetic element merges with the neighboring weak magnetic feature (frames 31-33; see [Figure 4.4](#)). Following this, a downflow (0.5 km s⁻¹) is re-established, but not for long because a narrow, weak upflow plume appears at the location of the BP by the end of the intensification phase at frame 33 (see insert). We cannot say whether this upflow feature is actually a part of the magnetic element boundary or just a non-magnetic gas parcel below the tube canopy, but

with its emergence, the continuum intensity increases sharply, reaching again values about $1.1 I_c$. We speculate that the presence of hot (bright) gas next to the magnetic element leads to an intensification of the bright point near the edge of the magnetic feature, since this hot gas heats up and brightens the wall of the magnetic element.

4.5 Mature flux tube

Figure 4.6 shows the newly formed kG magnetic flux concentration. The evolution of the different parameters at the flux tube's core can be followed in Figure 4.5a after the vertical dashed line.

Interestingly, rather than keeping a constant magnetic field strength, it drops below 1 kG where it stays for a number of frames before shooting up again. Oscillations of the strength of quiet-Sun magnetic fields have been observed for the first time by [Martínez González et al. \(2011\)](#) using the same IMAx data. They detected those oscillations by studying the changes with time of the area enclosed in a contour containing a constant magnetic flux. Here we have defined the area in the same way and, as expected, it varies in anti-phase with the field strength, whereas the LOS velocity is in phase with the field strength. First, it decreases to 0 km s^{-1} while the field strength drops to 700 G, and then it grows to 2.8 km s^{-1} as the field strength intensifies to 1500 G. Meanwhile, the continuum intensity remains almost constant in the interior of the magnetic core, around $1.0 I_c$. However, the intensity of the second BP shows a related oscillatory-like behavior at the wall of the magnetic element (see Figure 4.5 (b) after the vertical dashed line), reaching large values at times when the field strength is also large.

We have already mentioned the emergence of a small upflow plume at the end of the convective collapse (when the area is smallest). As shown in Figure 4.6, the following evolution of the BP is closely associated with that of the small upflow. Note that the upflow is observed exactly at the location where the BP is present. This fact can also be seen quantitatively in Figure 4.5 (b), after the vertical dashed line. As the upflow weakens, the gas cools down, the area increases and the intensity is reduced (time steps 34-36). Soon after that (time step 38) the area of the magnetic element starts to decrease again and a second upflow plume is detected followed by a rise in intensity.

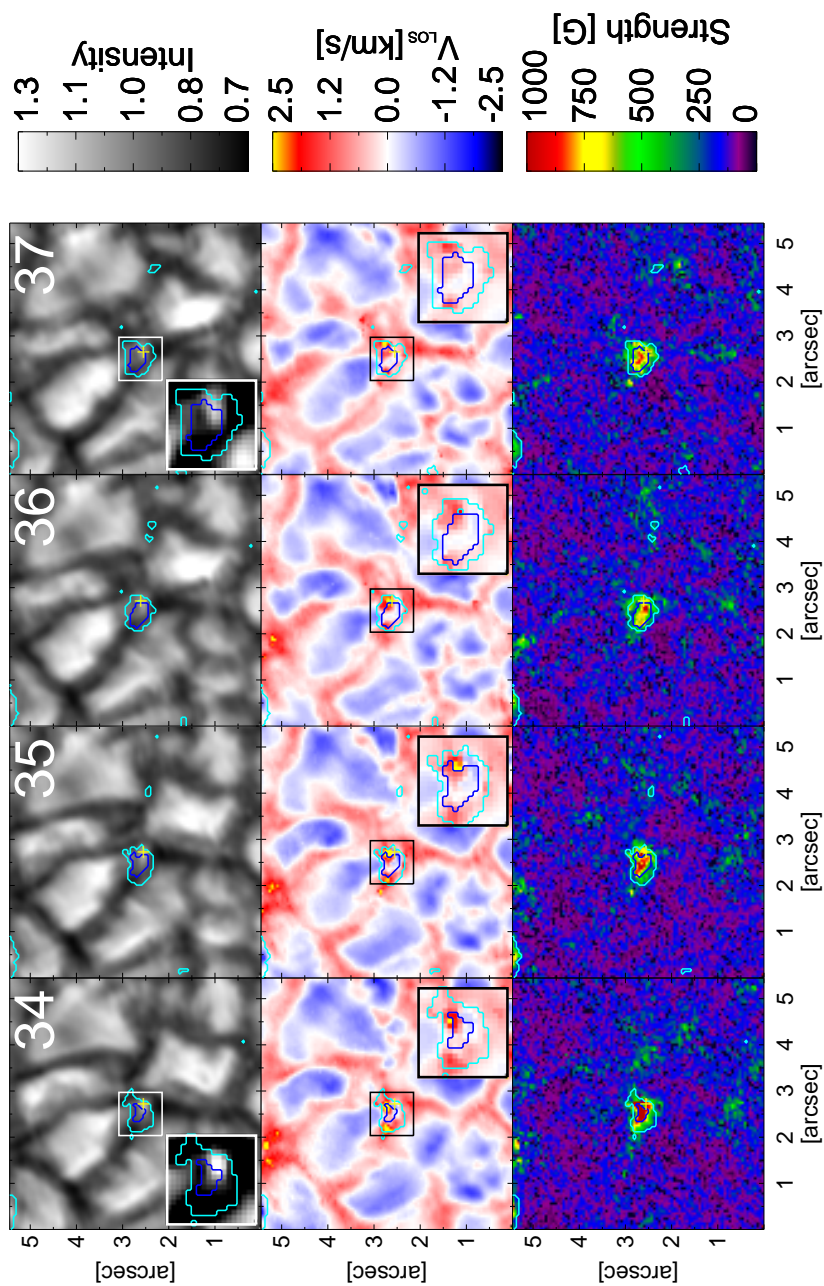
The second upflow feature appears when the magnetic element is being compressed (area reduced) again by the converging surrounding granules. Similar to those described in Section 4.4.1, two small-scale upflow features are again detected moving towards the flux concentration (indicated by arrows in Figure 4.6, frames 40-42). From the corresponding I_c maps, it can be concluded that they are associated with the splitting of neighboring granules. In addition, the daisy-like appearance is again enhanced.

Furthermore, the emergence of the small upflow takes place while a strong downflow of up to 2.8 km s^{-1} develops in the interior of the flux tube. Correspondingly, an upward/downward velocity pattern is observed within the magnetic element (frames 40-42). Similar small-scale upflow features often surrounded by ring-shaped downflows have already been observed in active plage regions (Narayan & Scharmer 2010). They detect them in large structures rather than in isolated BPs, which mostly show downflows, and interpret them as part of a small-scale magneto-convection in the interior of a strong plage solar magnetic field.

The anti-phase behavior of the velocity and brightness in the brightest point of the magnetic feature, suggests that at least some of the continuum brightness enhancements in the magnetic element are related to the presence of flows within it. We did not find any previous mention of such a relation between brightness and LOS velocity in BPs. This can be understood in terms of magneto-convection, with upflows bringing hot gas from below to cool and radiate away at the solar surface. But equivalently, it could also be explained by (magneto-acoustic) waves. Indeed, upwardly propagating acoustic waves are ubiquitous in quiet-Sun magnetic bright points and 3D MuRAM simulations (Jess et al. 2012). Whatever the mechanism may be, the intensity at the core of the magnetic element stays almost constant, with values close to $1.0 I_c$, while the BP brightness oscillates with an amplitude of $0.1 I_c$ as the small upflow features evolve.

4.5.1 Downflow plumes

As soon as the mature kG magnetic element is formed, and in agreement with Steiner (1999), two strong downflow plumes start to be clearly visible at the edge of the magnetic element in Figure 4.6 (frames 34 and 35). As an example, the rightmost downflow has a mean value of 2 km s^{-1} with speeds roughly up to 6 km s^{-1} (hence, almost supersonic) during its evolution. (Remember that the zoomed areas of the LOS velocity map are scaled to $[-5, 5] \text{ km s}^{-1}$.) These very high speed values have to be taken with caution because of the poor sampling of the spectral line in our data. Nevertheless, the Stokes profiles at these points display significant Doppler shifts although their quantitative value may be more uncertain than those for slower downflows. The downflows get weaker after two minutes, but they strengthen again around the same location at the end of the time sequence. Such strong downflows have been predicted by Steiner et al. (1998) in 2D models of magnetic flux sheets. In their 2D simulations, the downflows are fed by horizontal flows, and they evolve into “jets” as they become narrower and accelerate with depth. Here, the downflows appear in front of elongated converging granules. Accordingly, the gas required for producing such strong and narrow downdrafts is likely provided by these granules.



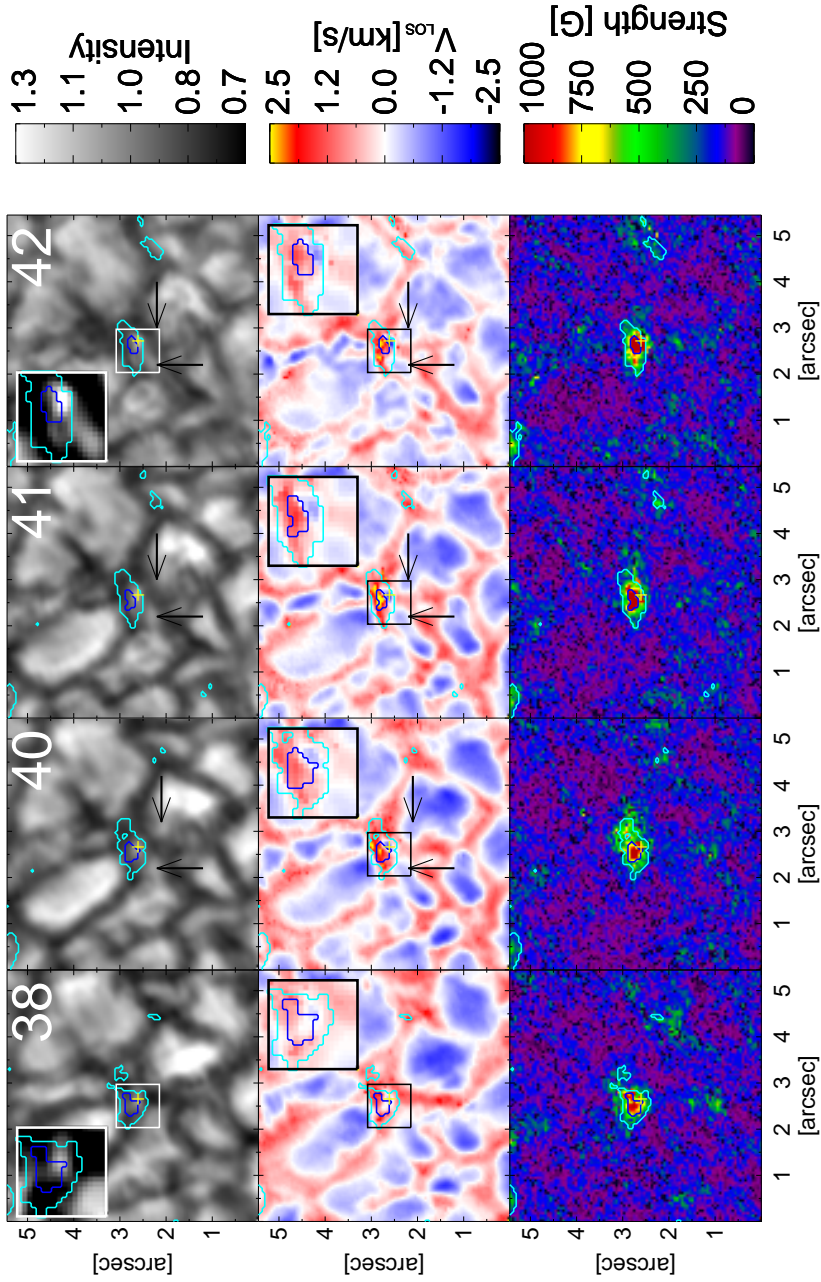


Figure 4.6: Same as Figure 4.4, during the evolution of the mature flux tube. This figure is also available within Animation 1 in the electronic edition of Requerey et al. (2014).

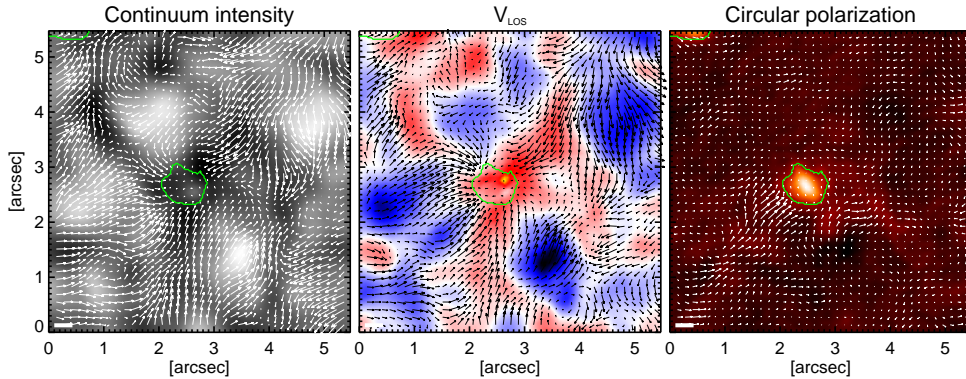


Figure 4.7: Same as Figure 4.3, but averaged over the whole data set (~ 23 minutes, frames 1-42). This figure is also available within Animation 1 in the electronic edition of [Requerey et al. \(2014\)](#).

4.6 Averaged history

In order to provide a global picture of the flux tube’s history, in Figure 4.7 we display the horizontal velocity maps averaged over the whole time series (~ 23 minutes, frames 1-42). Figure 4.7 is also illustrated by an animation where we show movies of continuum intensity, LOS velocity, circular polarization, and field strength maps. Making use of the LCT horizontal velocities we track the advection of passive tracers (corks) initially spread out all over the FoV ([Simon et al. 1988](#)).

The horizontal velocity obtained from the continuum intensity and LOS velocity point toward the magnetic feature near the centre of the FOV in Figure 4.7. A sink is centered at or close to the magnetic element throughout the data set, as persistent flows pointing towards it can be seen after averaging for 20 minutes (several times the life time of a granule; see [Verma et al. 2013](#)). Note that the flows tracked by LCT mainly show the evolution of the granulation with time, so that the converging flows imply that granules and granular fragments converge toward the center of the map. On the other hand, the circular polarization shows the advection of the sub-arcsecond magnetic patches, as described by the flux concentration phase.

The cork movies shown in the Animation 1 are very interesting. As time goes by, the corks flow towards the structure. While the continuum intensity tracers penetrate the magnetic feature, the ones for the LOS velocity end up at its border. The continuum intensity corks concentrate at two different inner borders of the structure. The location of the BPs described in Section 4.4.2 match very well with those two concentrations. Furthermore, the LOS velocity corks show two accumulation points at two opposite edges of the structure.

The downflow plumes described in Section 4.5.1 are observed close to if not within these accumulation points.

4.7 Summary and Conclusions

We have presented high resolution observations of the formation and evolution of an isolated quiet-Sun magnetic element and its interaction with the neighbouring convection. We have analyzed the polarization maps and used the SIR inversion code to retrieve LOS velocities and the vector magnetic field.

The history of our magnetic element starts with a small-scale magnetic Ω loop emerging in a granular upflow. The footpoints are dragged out into nearby intergranular lanes where some pre-existing, sub-arcsecond, positive circular polarity patches are already present. The linear polarity feature disappears at the same time as the negative footpoint cancels with one of those positive polarity patches. This cancellation is associated with a supersonic magnetic upflow detected by Borrero et al. (2010), which is probably a signature of magnetic reconnection between the cancelling opposite polarity magnetic features. The positive polarity footpoint and the pre-existing flux patches are swept along the lanes by converging granules and concentrated roughly up to (and possibly even beyond) the equipartition field strength (300-500 G).

This process is unable to concentrate the magnetic field significantly above equipartition values. Further intensification is achieved when downdrafts inside the magnetic field concentration are enhanced. According to the canonical convective collapse picture, at this point the tube is evacuated and the flux is compressed by the excess pressure of the surrounding gas. This compression leads to a reduction in the area of the flux concentration and an enhancement of its field strength. This phase of convective collapse is qualitatively consistent with the results of 3D MuRAM (Vögler et al. 2005) simulations and their comparison with *Hinode*/SP observations by Danilovic et al. (2010a). During this process, and due to the formation of a Wilson depression (Spruit 1976), the nearby gas cools and hence has a reduced pressure, creating a horizontal pressure gradient with respect to the gas that is located further away. Driven by the pressure gradient, gas then flows towards the magnetic feature. The traces of this inflow can be seen in Figure 4.7. The field lines act as a stiff hindrance to granular convection, so that a characteristic daisy-like granular pattern forms, in agreement with the observations of Muller et al. (1989) and Muller & Roudier (1992).

As the flux tube gets cooler than its surrounding at a given geometrical height, it is irradiated laterally from the gas in its immediate surroundings, which is fed by the converging granules and granular fragments. We observe the formation of two BPs within a seemingly

single magnetic element.² Both are located at or close to the boundary of the kG feature. We trace the bright point located at the lower edge of the magnetic element using the same approach as Nagata et al. (2008) and find that at the end of the convective collapse phase it displays an upflow. A similar upflow has also been seen by Bellot Rubio et al. (2001). They interpret it as a “rebound” arising when the internal downflows turn into upflows, and associate them with the destruction of the flux tube. However, in our study, the small-scale upflow feature does not destroy the magnetic flux tube and rather a large-amplitude variation in area and field strength is observed which may be part of an oscillatory pattern (only a single period is seen, due to the limited length of the observation).

We find that the field strength varies in anti-phase with the area enclosed by a contour of constant magnetic flux, supporting the conclusion drawn by Martínez González et al. (2011) that oscillations in this area are proportional to oscillations in field strength. In the tube core LOS velocity also changes in anti-phase with area. In the BP case however, brightness also varies in anti-phase with area while LOS velocity does it in phase. The BP follows the evolution of an emerging upflow plume. The upflow dissolves as the area increases in size, and a second upflow appears while the area recovers its initial value. Through this evolution the BP oscillates with an amplitude peak of $0.1 I_c$ above the almost constant brightness intensity at the tube core of about $1 I_c$.

Unfortunately, the data-set limited time span does not allow us to know whether an oscillations will continue or not. However, the magnetic field oscillations detected by Martínez González et al. (2011), as well as observations of BPs experiencing several brightness enhancements during their life (Muller & Roudier 1992), suggest that the magnetic element could undergo more oscillations.

Once the mature flux tube has been formed, we also find narrow, strong downflows at its edges. Two-dimensional models by Steiner et al. (1998) predict flux sheets bordered by narrow downflows. The classical picture for the creation of asymmetries in the presence of canopies (Grossmann-Doerth et al. 1988; Solanki 1993) predicts the appearance of such downflows. Bellot Rubio et al. (1997, 2000) already detected them in unresolved magnetic flux tubes. Here, we do not find rings of downflows bordering the magnetic structure, but rather downflow plumes at the edge’s of the flux concentration, similar to those observed by Rimmele (2004) in active region flux tubes. These downflows are accompanied by small-scale upflow features that appear at the external border of the magnetic element core. Our high spatial resolution findings agree very well with those obtained by Martínez González et al. (2012b), also based on IMAx data.

²Notice that in frame 25 of Figure 4.4 the magnetic element displays two close cores with strengths above 1 kG that subsequently merge in frame 26. This is a phenomenon that can be better seen in other magnetic structures of the same data set and whose study and discussion is deferred to Chapter 5.

Our new observation of a strong anti-phase correlation between the continuum intensity and the LOS velocity within the BP deserves a small discussion. A first suggestion can be drawn out of it: at least part of the continuum brightness of the magnetic feature is related to the presence of flows within it. Most notably, the brightness enhancement and the anti-phase velocity are not seen in the central, strongest core of the magnetic element. Rather they appear at well-localized, small-scale places of its external part. Whether this phenomenon is common to this type of elements or not cannot be ascertained from our present data. Further studies focused on this topic promise to offer new insight into the physics of quiet-Sun magnetic flux tubes.

Several mechanisms can be invoked to explain the possible oscillatory behavior. Overturning magneto-convection could be one such mechanism as the detailed studies by, e.g., [Weiss et al. \(1996\)](#) suggest. Another possible scenario is provided by overstable oscillations ([Spruit 1979](#); [Hasan 1985](#)) that can start as soon as the collapse has stopped. If the pattern we observe is not of a convective origin, we then have a third possibility: we might be witnessing the upward propagation of acoustic waves ([Jess et al. 2012](#)). If so, waves could be excited through magnetic pumping ([Kato et al. 2011](#)). Indeed, transient downflows in the immediate surroundings of a magnetic element, downdraft and upflows within the flux tube, and constant magnetic flux area oscillations are signatures of such a mechanism. Alternatively, the fourth option can be found in “sausage” modes ([Edwin & Roberts 1983](#)) excited through compression by granules. The very large amplitude of the oscillation in basically all variables, in particular in the magnetic field strength may also be a sign that it is not a true oscillation at all, but rather multiple episodes of convective collapse, with a loss of equilibrium in between. What is causing the flux tube’s field to be so unstable has not become entirely clear from this study. However, the absence of a strong upflow during the decay phase of the field strength suggests that this phase is not initiated by a strong upflow (rebound shock) such as that found by [Grossmann-Doerth et al. \(1998\)](#). Since we are only looking at a photospheric height, the present observations do not allow us to distinguish between the different mechanisms. In order to study the chromospheric response, we plan to supplement IMA_X observations with the simultaneous Ca II H filtergrams from the SUNRISE Filter Imager (SuFI; [Gandorfer et al. 2011](#)).

It is evident that the formation and the subsequent evolution of a solar magnetic element is a complicated problem, where many phenomena take place, namely, emergence of a magnetic Ω loop, expulsion of its footpoints from a granule, merging of flux patches in a long-lived inflow, formation of a kG magnetic element by convective collapse and granular compression, a subsequent weakening of the field strength to further increase again to kG values either through an oscillation or a second collapse. For the first time, we have been able to observe and relate all these phenomena in a single example.

DYNAMICS OF MULTI-CORED MAGNETIC STRUCTURES IN THE QUIET SUN

We report on the dynamical interaction of quiet-Sun magnetic fields and granular convection in the solar photosphere as seen by SUNRISE. We use high spatial resolution ($0''.15$ – $0''.18$) and temporal cadence (33 s) spectropolarimetric Imaging Magnetograph eXperiment data, together with simultaneous CN and Ca II H filtergrams from SUNRISE Filter Imager. We apply the SIR inversion code to the polarimetric data in order to infer the line of sight velocity and vector magnetic field in the photosphere. The analysis reveals bundles of individual flux tubes evolving as a single entity during the entire 23 minute data set. The group shares a common canopy in the upper photospheric layers, while the individual tubes continually intensify, fragment and merge in the same way that chains of bright points in photometric observations have been reported to do. The evolution of the tube cores are driven by the local granular convection flows. They intensify when they are “compressed” by surrounding granules and split when they are “squeezed” between two moving granules. The resulting fragments are usually later regrouped in intergranular lanes by the granular flows. The continual intensification, fragmentation and coalescence of flux results in magnetic field oscillations of the global entity. From the observations we conclude that the magnetic field oscillations first reported by Martínez González et al. correspond to the forcing by granular motions and not to characteristic oscillatory modes of thin flux tubes.

5.1 Introduction

Most of our empirical knowledge of the structure and dynamics of quiet-Sun magnetism derives from observations of the solar photosphere. In this thin layer, magnetic energy is in many places of the same order as the kinetic energy. Therefore, the interaction between the magnetic field and convection at the solar surface is an efficient way of converting kinetic energy into form that can be transported to the upper layers of the solar atmosphere by the magnetic field.

The most direct method of detecting the solar magnetic field is by measuring polarized light generated via the Zeeman effect. Unfortunately, in the quiet Sun, the Zeeman effect produces only a weak polarization signal, whose measurement requires both, high spatial resolution and accurate polarimetric sensitivity. Such measurements have only recently been achieved by the *Hinode* Spectro-Polarimeter (Lites et al. 2013) and the Imaging Magnetograph eXperiment (IMaX; Martínez Pillet et al. 2011a) aboard the SUNRISE balloon-borne solar observatory (Solanki et al. 2010; Barthol et al. 2011; Berkefeld et al. 2011; Gandorfer et al. 2011).

Before the era of space-borne spectropolarimeters, polarimetric observations have been limited by the need for stable seeing conditions to achieve a high spatial resolution. Instead, to maximize spatial and temporal resolution, indirect signatures, or proxies of magnetic structures have been used. In particular, magnetic elements, usually described in terms of flux tubes, have been tentatively identified with bright points (BPs) in photometric observations. Based on a recent comparison between SUNRISE observations and MHD simulations, Riethmüller et al. (2014) deduce that all magnetic BPs are associated with kG magnetic flux concentrations.

White-light observations obtained at the Pic du Midi Observatory in the French Pyrénées, revealed a mean lifetime of 18 minute for facular (Muller 1983) and network (Muller & Roudier 1992) BPs. Many BPs become elongated when they are squeezed between two moving or expanding granules (Roudier et al. 1994). 70% of these elongation processes end with the fragmentation of the bright structures.

Muller & Roudier (1984) were the first to observe bright points in the Fraunhofer G band, a CH molecular band-head around 430.5 nm. At these wavelengths BPs exhibit higher contrast than the one they display in the continuum. Berger & Title (1996) studied the dynamics of G-band bright points observed with the 50 cm Swedish Vacuum Solar Telescope (Scharmer et al. 1985) on the island of La Palma, Spain. Driven by the evolution of the local granular convection flows, fragmentation and coalescence are two important processes driving the evolution of BPs. BPs also appear to rotate and fold in chains or groups. Periodically, they split into smaller fragments, merge with other BPs, and sometimes fade until

they are no longer distinguishable from their surroundings. Nonetheless, [Berger et al. \(1998\)](#) found some BP groups to persist during the entire 70 minute data set. However, the different members of these chains cannot be identified as individual entities for longer than a granule lifetime, i.e., 6-8 minutes. Consistent with this view, [Berger & Title \(1996\)](#) concluded that the canonical picture of stable, isolated flux tube does not agree with observations.

Simultaneous filtergram and magnetogram observations revealed that continuum and line-core BPs ([Keller 1992](#); [Title et al. 1992](#); [Yi & Engvold 1993](#)) and G-band BPs ([Berger & Title 1996, 2001](#)) appear associated with a magnetic feature. While isolated BPs have nearly the same size as the associated magnetic element, BP groups appear inside a large magnetic structure that extends beyond the group. For the largest magnetic structures, [Muller et al. \(2000\)](#) found several magnetic signal maxima at the location of individual BPs.

If we assume that BPs are the counterparts of magnetic flux tubes, their fragmentation by the perturbation of surrounding granules might indicate that magnetic elements are liable to the interchange, or fluting, instability (e.g., [Krall & Trivelpiece 1973](#), Chap. 5). [Parker \(1975\)](#) and [Piddington \(1975\)](#) noticed that the interchange instability is indeed an intrinsic property of flux tubes. However, due to the reduced density of the magnetic plasma, [Meyer et al. \(1977\)](#) showed that flux tubes with fluxes greater than about 10^{19} Mx, such as sunspots and pores, can be stabilized by buoyancy thanks to the rapid expansion with height of their field. Small quiet-Sun magnetic structures with fluxes in the range of 10^{16} – 10^{18} Mx (e.g. [Wang et al. 1995a](#)) obviously do not fulfill this criterion. [Schüssler \(1984\)](#) proposed that such features could be stabilized as well if they are surrounded by whirl flows, with a whirl velocity around magnetic features between 2 and 4 km s⁻¹ ([Bunte et al. 1993](#)). Observations of whirl flows were first reported by [Bonet et al. \(2008\)](#). However, their lifetimes are only about 5 minute, on average, as they often do not survive neighboring granules, which have a similar lifetime ([Bonet et al. 2010](#)).

Stabilization of magnetic elements by means of the whirl flow mechanism is restricted to cylindrical flux tube geometry. [Bunte \(1993\)](#) showed that elongated magnetic slabs, or flux sheets, are also flute unstable. He demonstrated that the slabs are most strongly liable to the instability in a layer close to $\tau_c = 1$, where fragmentation into single tube-filaments takes place. These filaments, however, lose their identity at lower and upper layers as they merge into a single, stable magnetic slab. Of course, the validity of such idealized computations in the real, highly dynamic, turbulent solar photosphere remains an open question.

In order to shed new light on the physical mechanism behind the dynamic nature of quiet-Sun magnetism, high spatial and temporal resolution is required over a sufficiently long time series, along with accurate polarimetry. Such high-quality observations have only recently been achieved with SUNRISE/IMaX. The unprecedented spatial resolution of $0''.15$ – $0''.18$, allowed for the first time photospheric magnetic elements to be spatially resolved

even in the quiet Sun internetwork without requiring an ad-hoc filling factor, that specifies the fraction of the pixel filled with magnetic field (Lagg et al. 2010). This represents a considerable advance compared to previous works that studied magnetic structures via their indirect signatures, e.g., BPs, or without resolving the magnetic fields.

In Chapter 4, we reported on the first direct observation of the formation of an individual photospheric magnetic element as seen by SUNRISE/IMaX. Here, we complement that work by investigating the dynamical interaction of quiet-Sun magnetic structures with the convective flows.

5.2 Observations and data reduction

The spectropolarimetric observational data were obtained with SUNRISE/IMaX on 2009 June 9 from 00:36:03 UT to 00:58:46 UT, in a quiet-Sun region close to disk center. The data set of ~ 23 minutes length has a temporal cadence of 33 s, with a pixel size of $0''.055$. Throughout the observing cycle, the full Stokes vector was sampled at five wavelength positions across the Fe I 525.02 nm line (Landé factor $g = 3$) at $\lambda = -8, -4, +4, +8,$ and $+22.7$ pm from the line center (V5-6 mode of IMaX; see Martínez Pillet et al. 2011a, for details). For the polarization analysis, the incoming light is modulated by two liquid crystal variable retarders (LCVRs) and analyzed by a beam splitter. The spectral analysis is performed by a Fabry–Pérot interferometer based on a double-pass LiNbO₃ etalon.

IMaX data reduction and instrument calibrations are described by Martínez Pillet et al. (2011a). Several procedures were used for dark-current subtraction, flat-field correction, and polarization cross-talk removal. The calibration set consisted of 30 in-focus and out-of-focus image pairs that, through phase diversity (Gonsalves 1982; Paxman et al. 1996), were used for post-facto point-spread function (PSF) retrieval. The science images were reconstructed by deconvolving this PSF from the originally recorded images. The process requires an apodization that effectively reduces the IMaX field of view (FOV) down to about $43'' \times 43''$. The blueshift over the FOV produced by the Fabry–Pérot interferometer is corrected in the inferred velocity values. The instrument achieved a spectral resolution of 8.5 pm and the spatial resolution has been estimated to be $0''.15$ – $0''.18$ after reconstruction. The noise level in each Stokes parameter is about 3×10^{-3} in units of the continuum intensity, and the rms contrast of the quiet-Sun granulation obtained from continuum data is about 13.5% (Solanki et al. 2010), which testifies to the outstanding quality of IMaX images. We determine the line-core intensity by fitting the observed IMaX Stokes I profiles at the sampled spectral positions by a Gaussian.

In addition to the IMaX Fe I 525.02 nm images, several nearly simultaneous CN (centered at 388 nm with FWHM ≈ 0.8 nm) and Ca II H (centered at 396.8 nm with FWHM \approx

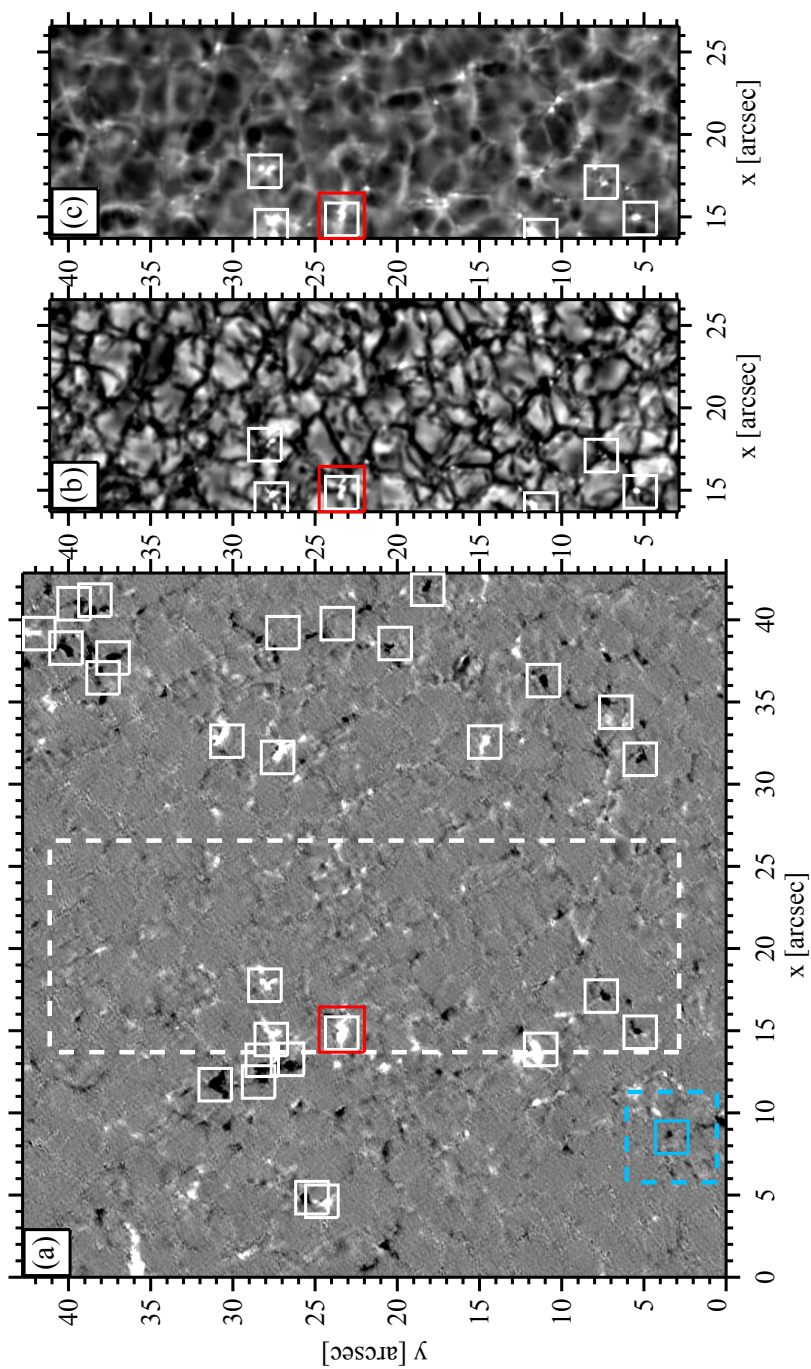


Figure 5.1: Examples of co-spatial images from both, the IMAx and SuFI instruments. (a) IMAx Fe I 525.02 nm longitudinal magnetic field covering the full FOV of about $43'' \times 43''$. The longitudinal component of the magnetic field, $B \cos \gamma$, is linearly scaled from -100 to 100 G. The white dashed-line rectangle, with a FOV of $13'' \times 38''$, illustrates the co-aligned area in common with the SuFI CN and Ca II H images. The white boxes enclose locations where multi-cored magnetic structures are observed. The red box highlights a feature that is examined in detail in Section 5.4. (b) SuFI CN image. (c) SuFI Ca II H image.

0.18 nm) filtergrams obtained with the SUNRISE Filter Imager (SuFI; [Gandorfer et al. 2011](#)) are used in the present Chapter. The time series has a cadence of 12 s, with a pixel size of $0''.0207$, and a FOV of about $13'' \times 38''$. The CN and Ca II H bandpass images have been phase diversity reconstructed ([Hirzberger et al. 2011](#)).

Since SuFI and IMAx data have different cadences, we select those CN and Ca II H images whose observing times are closest to the IMAx observations. Note that the pixel size is also different. Thus, we increase the size of the SuFI image pixels by neighborhood averaging to a common scale with IMAx. Furthermore, we properly align the images by applying a cross-correlation technique on all simultaneous frames of Ca II H and the IMAx line-core intensity, i.e., the data products having the closest BP contrast.

5.3 Data analysis

To determine the vector magnetic field and the LOS velocity, inversions of the full Stokes vector are carried out with the SIR code ([Ruiz Cobo & del Toro Iniesta 1992](#)) for all time steps in our series. This code numerically solves the radiative transfer equation along the LOS under the assumption of local thermodynamic equilibrium, and minimizes the difference between the measured and the computed synthetic Stokes profiles using response functions.

Starting from the Harvard–Smithsonian Reference Atmosphere ([Gingerich et al. 1971](#)) as initial guess (with added magnetic and velocity parameter values), the temperature T , is modified with two nodes.¹ The magnetic field strength B , the inclination and the azimuth angles γ and φ , the LOS velocity v_{LOS} , and the microturbulent velocity v_{mic} are assumed to be constant with height. The magnetic filling factor f is assumed to be unity and the macro-turbulent velocity v_{mac} is set to zero due to the high spatial resolution of the data. From B and γ we also derive the longitudinal component of the magnetic field $B_{\text{long}} = B \cos \gamma$. At each iteration step the synthetic profiles are convolved with the spectral PSF of IMAx, which was measured in the laboratory before the launch of SUNRISE ([Riethmüller et al. 2014](#)). To estimate the noise-induced uncertainty in the field strength and LOS velocity, we repeat the inversions with 100 different realizations of added noise to the observed Stokes pro-

¹As usual in SIR, the whole atmosphere is perturbed regardless of the number of nodes. *Equivalent* response functions are calculated at these nodes that include the sensitivity of **all** depth grid points (see [Ruiz Cobo & del Toro Iniesta \(1994\)](#) and [Del Toro Iniesta \(2003\)](#)). The number of nodes basically indicates the degree in the polynomial spline interpolation that is assumed to apply to the perturbations (not to the final stratification). In the specific case of two nodes, they are put at the first and last point of the grid ($\log \tau_c = 1.4$ and -4.0) but such positions are irrelevant: the same linear perturbation is applied independently of the node positions. However, it is worth noting that with only five wavelength points, the temperature is not well constrained in layers above $\log \tau_c = -2$ or below $\log \tau_c = 0.5 - 0$.

files. Amplitudes of 3×10^{-3} in units of the continuum intensity were used. The standard deviation of the 100 results is 150 G and 150 m s^{-1} respectively.

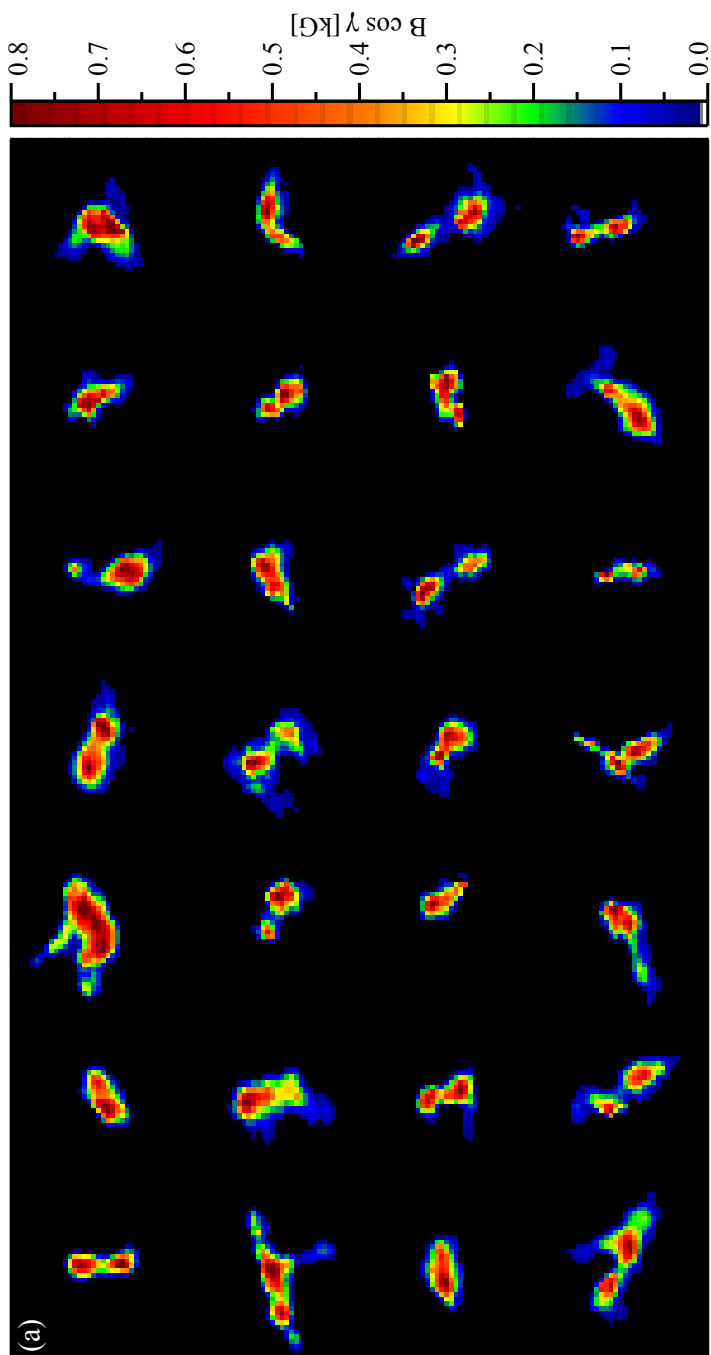
Finally, we apply a p-mode subsonic filter (Title et al. 1989) to the continuum intensity, line-core intensity, LOS velocity, CN and Ca II H images, and compute the horizontal velocity maps of the continuum intensity by means of a local correlation tracking (LCT) technique (November 1986; November & Simon 1988) as implemented by Molowny-Horas & Yi (1994). Figure 5.1 displays example frames of an IMAx longitudinal magnetic field (left), a SuFI CN (center) and a Ca II H (right) image after co-alignment.

5.4 Multi-cored magnetic structures

The high spatial and temporal resolution observations allow us to study the dynamics of resolved small-scale magnetic structures. This implies that we are able to track magnetic elements themselves rather than just their proxies, i.e., BPs. We use time series of B_{long} as context data to follow the evolution of magnetic elements. After visual inspection of each maps frame, we identify 28 groups of flux tubes evolving as single entities while the individual tubes undergo different coalescence and fragmentation processes. The locations where such magnetic structures are detected are highlighted by white boxes in Figure 5.1.

Figure 5.2 shows enlarged views of these structures. The longitudinal magnetic field maps (Figure 5.2(a)) illustrate “multi-cored” magnetic structures that are resolvable into a series of more elemental structures, each of which might be described by a flux tube. In general, the magnetic structures are seen in the longitudinal magnetic field maps to have at least two inner cores surrounded by a common and weaker envelope. In most cases, the line core intensity maps display a BP associated with each magnetic core (see Figure 5.2(b)). Thus, the multi-cored magnetic structures are generally characterized by groups of resolved BPs. Similar quiet-Sun bright structures have been previously observed by e.g., Berger & Title (1996); Berger et al. (1998, 2004); Rouppe van der Voort et al. (2005) and Goode et al. (2010). Here we have been able to relate each BP group with a magnetic core group that belongs to a common underlying magnetic structure.

The red box in Figure 5.1 highlights a region of interest containing a representative example of a multi-cored magnetic structure whose dynamics we have followed. We focused on this region because it shows, in a single example, many of the processes involved in the evolution of these magnetic features. In addition, it is one of the comparatively few cases for which we have also information from SuFI. We describe it in some detail in what follows.



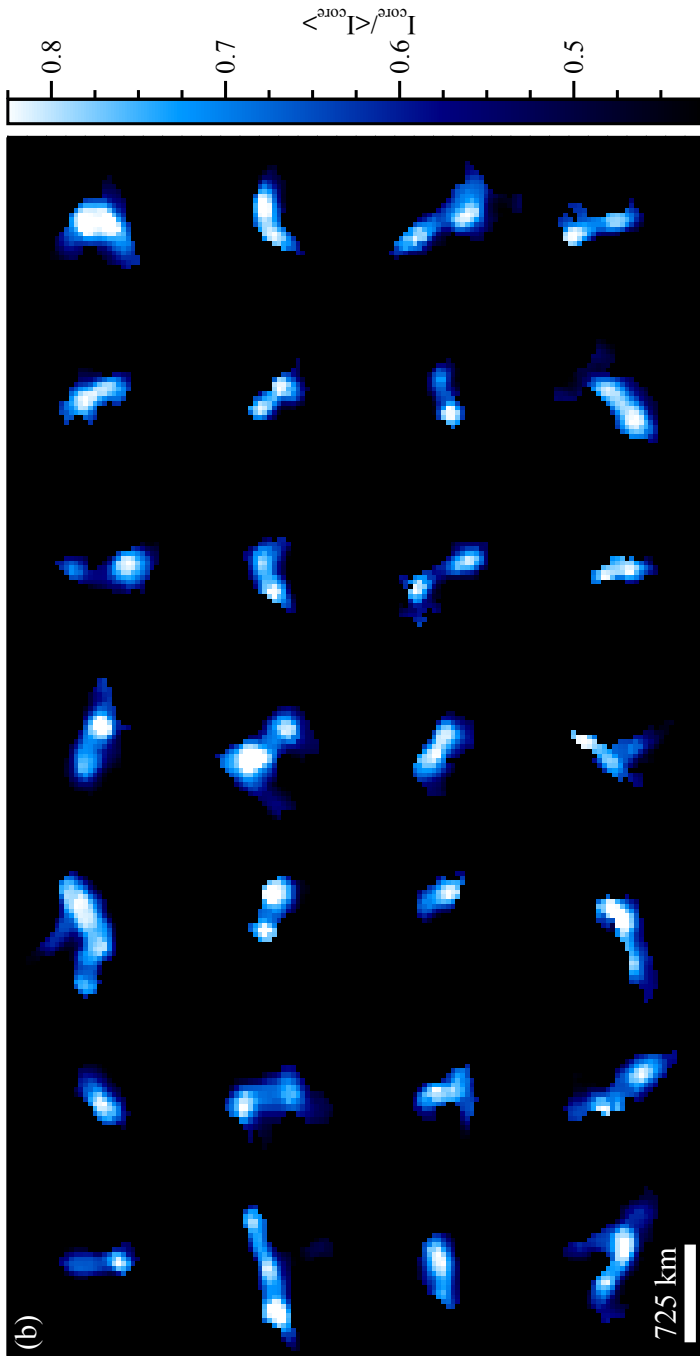


Figure 5.2: Enlarged views of the white boxes in Figure 5.1. Each structure corresponds to a different box and is not co-temporal with the others. (a) Longitudinal component of the magnetic field. (b) Line-core intensity in units of the continuum intensity. For clarity, the plotted line-core intensity has been set to zero outside the magnetic features.

5.5 Evolution of magnetic elements

Figure 5.3 illustrates the temporal evolution of a multi-cored magnetic structure (red box in Figure 5.1) based on five selected B_{long} maps (first row), magnetic field strength and inclination maps (second and third rows), and co-aligned CN maps (fourth row). The blue contour in the last row marks the periphery of the multi-cored magnetic structure. This has been selected by visual inspection in such a way that all the magnetic cores are kept within the global structure. In all frames it delineates longitudinal magnetic field iso-contours of approximately 250 G, and it encloses a magnetic flux of $(5.4 \pm 1.3) \times 10^{17}$ Mx, where ± 1.3 is the amount by which it changes over time. This contour will be used until the end of Section 5.6.

In frame number 13, an elongated CN bright structure, with two seemingly brighter concentrations, is observed. (The existence of two BPs can be confirmed through their evolution as seen in Animation 2.) The co-temporal longitudinal magnetic field map identifies the two brighter concentrations (BPs) with two associated magnetic cores embedded in a more diffuse magnetic structure. These cores are also clearly observed in the field strength and inclination images. The structure is formed by two strong (~ 1000 G) and almost vertical ($\sim 20^\circ$) inner cores surrounded by a common, weaker (~ 400 G) and more inclined ($\sim 70^\circ$), canopy-like ring. Evidence that such rings are associated with canopies in single-cored magnetic structures has been provided by, e.g., [Rezaei et al. \(2007\)](#), [Martínez González et al. \(2012b\)](#) and [Buehler et al. \(2015\)](#). Our highly inclined fields of the rings are fairly consistent without a-priori assumptions with the conventional picture of a canopy. However, their quantitative values may be more uncertain than those from the cores, because the polarimetric signal is weaker over the rings than over the cores. [Martínez González et al. \(2012b\)](#), for instance, found smaller tube expansions with higher spectral resolution from SUNRISE/IMaX, but no linear polarization was studied since only Stokes I and V were available in their case.

The magnetic morphology suggests that the dual-core feature is formed by two magnetic elements (flux tubes) that lose their individual identity as they expand with height and merge together. Canopy merging has been observed by [Buehler et al. \(2015\)](#) in a fairly different scenario: they report on individual magnetic flux concentrations whose canopies blend with those from neighbor concentrations.

The subsequent evolution shows² that the rightmost magnetic core splits into two (frame 20). Then the three of them merge and form an isolated magnetic element (frame 32). Soon afterwards, however, it fragments into two apparently identical cores (frame 37) that subsequently start to fuse again into a single magnetic concentration (frame 41). Two small

²Better seen in Animation 2. We suggest the reader to manually play back and forth the individual frames of the movie.

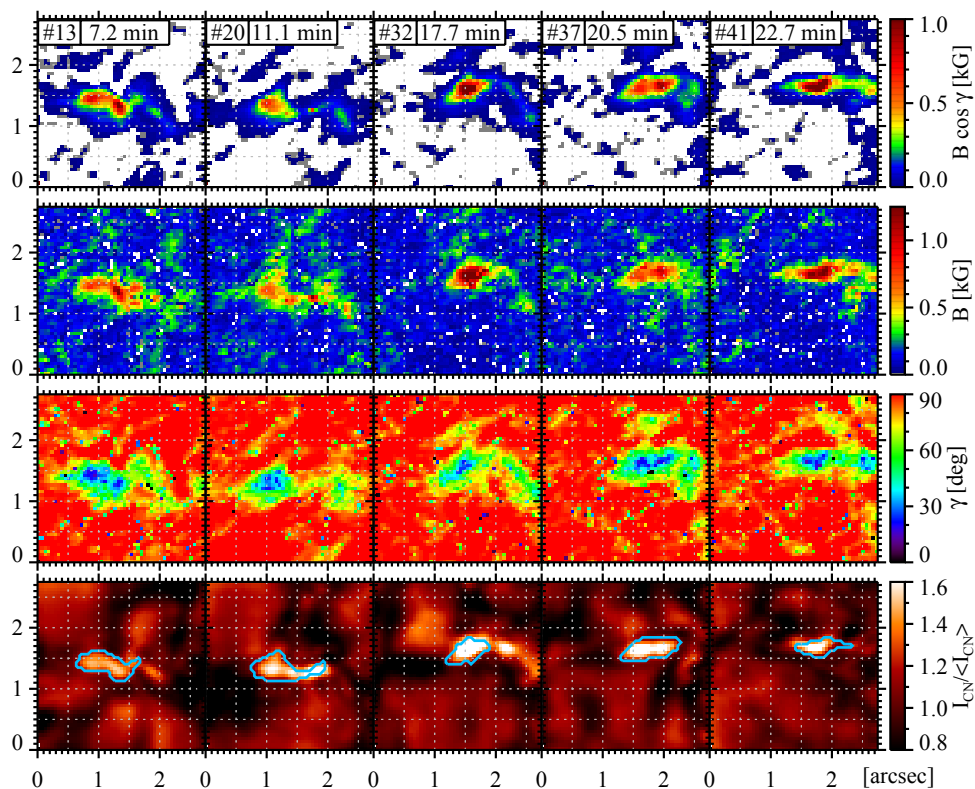


Figure 5.3: Evolution of a multi-cored magnetic structure (red box in Figure 5.1). First row: longitudinal magnetic field. Second row: magnetic field strength B . Third row: magnetic field inclination γ . Fourth row: CN band images. Frame numbers and elapsed time are given in the upper left corner of each top frame. Both axes are in arcsec.

remnants appear to leave the main merged core during the merging process itself. They follow an independent evolution (best seen in the CN maps) until the end of the time series through which both merge into a different (weaker) magnetic structure. Despite these recurrent fragmentation and coalescence processes, the magnetic cores keep sharing the same canopy over the whole time. These processes are analyzed in more detail in the following section.

Since we have observed that CN BPs are good proxies of magnetic cores and this is also true for those seen in the G band (Kiselman et al. 2001), the above-described evolutionary behavior is consistent with the photometric observations of, e.g., Berger & Title (1996). In the light of our co-aligned spectropolarimetric observations we are in a position to assert

that such BP groups, that keep together for periods much longer than a granule lifetime (up to 70 minute in [Berger et al. 1998](#)), can be members of the same magnetic structures.

5.6 Interaction with granular convection

Figure 5.4 indicates the different processes that take place during the evolution of the multi-cored magnetic structure due to its interaction with the local granular convection flows. From top to bottom, the rows show longitudinal magnetic field maps, CN intensity, LOS velocity, and continuum intensity maps. This figure is complemented by Animation 2, which is included in the electronic edition of [Requerey et al. \(2015\)](#). In the animation we also display the Ca II H intensity maps. As in Figure 5.3, the blue contours mark the periphery of the multi-cored magnetic structure. The new black contours have been created to follow the evolution of the individual magnetic cores and delineate a set of regions whose summed magnetic flux is constantly equal to 2.9×10^{17} Mx throughout the period of observation. These flux contours are constructed by starting from the most intense pixels in the longitudinal magnetic field map and then gradually expanding the contour by lowering the B_{long} for pixels included inside it. The black contours thus outline the magnetic cores. Finally, blue arrows show the horizontal velocity maps inferred through the LCT technique by correlating the displayed frames with the previous ones.

In Figure 5.5 we quantitatively analyze the evolution of the multi-cored magnetic structure shown in Figure 5.4. For this purpose, we manually track the magnetic cores in the longitudinal magnetic field maps. Figure 5.5 (a) displays the evolution of the area enclosed by our constant-flux region of 2.9×10^{17} Mx. This area is delimited by black contours in Figure 5.4. The other panels show the evolution of the LOS velocity (b), field strength (c), and CN intensity (d) for each of the magnetic cores. To increase the signal-to-noise ratio in the magnetic core physical parameters, we represent averages over 9 pixels around their B_{long} centroid. The red and green lines correspond to the leftmost and rightmost cores respectively, while a black line is drawn when the two cores merge into one. The vertical dotted lines corresponds to the end of the different phases described in the following Sections.

5.6.1 Intensification by granule compression

From frame 12 to 16, the leftmost magnetic core (red lines in Figure 5.5) stays at rest whereas the rightmost magnetic core is compressed between two granules (Figure 5.4 and Animation 2). The upper granule (at coordinates $[1''75, 2'']$ in frame 12) moves toward the magnetic core, while the lower granule (at coordinates $[1''25, 0''25]$) expands. This compression process results in the intensification of the magnetic core. The field strength

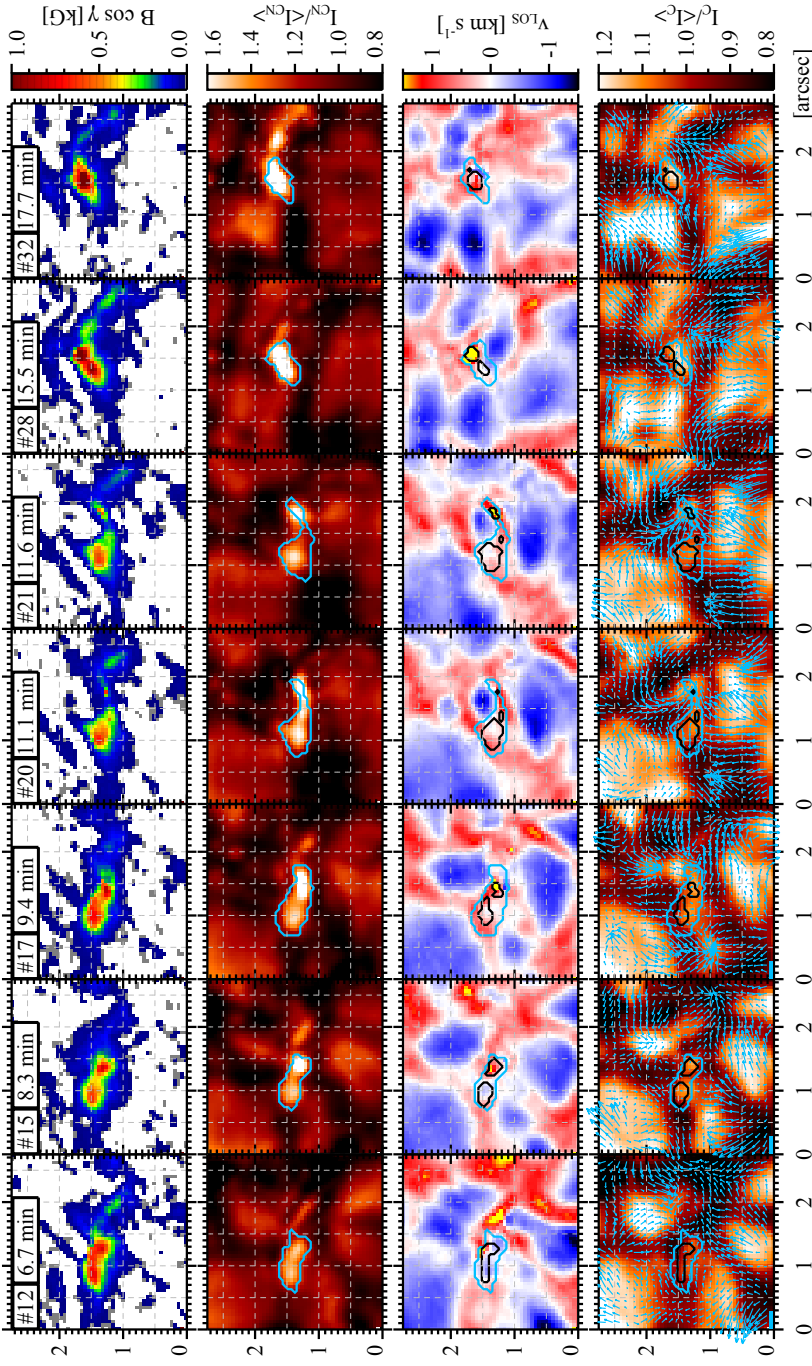


Figure 5.4: Closeup of the first three frames in Figure 5.3 with greater temporal resolution. First row: longitudinal magnetic field $B \cos \gamma$. Second row: CN images. Third row: LOS velocity v_{LOS} . Fourth row: continuum intensity. The total magnetic flux within all the black contours in a given image is constantly equal to 2.9×10^{17} Mx. Overplotted blue arrows outline the horizontal flow field derived through the LCT technique by correlating the displayed frames with the previous ones. The length of the blue bar at coordinates $[0''/0, 0''/0]$ corresponds to 1.8 km s^{-1} . Blue contours are the same as in Figure 5.3. This figure is also available within Animation 2 in the electronic edition of Requerey et al. (2015).

increases from about 800 G to about 1100 G (green line in Figure 5.5 (c)) as the CN intensity also rises. Meanwhile, the LOS velocity grows from nearly 0 to 1.1 km s^{-1} (average) with a peak velocity of up to 3 km s^{-1} . This maximum downflow is reached at frame 16 within the rightmost core close to a small upflow feature that emerges at the edge of the magnetic structure. As soon as this small-scale downflow/upflow feature appears, a co-spatial BP is detected in the Ca II H images (see Animation 2).

Such a nearly simultaneous small-scale downward/upward velocity pattern was first observed within a magnetic element (Chapter 4) and, later, close to many BPs visible in the line core of Fe I 525.02 nm (Utz et al. 2014). In Chapter 4, this pattern was detected at the end of two consecutive magnetic field intensification processes. The isolated magnetic element was compressed by all surrounding granules, and both intensification processes led to a reduction in the area of the flux concentration and an enhancement of its field strength. In our new observations, however, this phase does not contribute much to decreasing the area of the global magnetic structure (Figure 5.5 (a)). This is mainly due to the small size of the rightmost magnetic core compared to the entire area covered by magnetic flux.

5.6.2 Fragmentation

After the intensification phase the rightmost magnetic core and its related CN BP get elongated (frame 17 in Figure 5.4) as a consequence of the compression. The “squeezing” ends by fragmenting the magnetic core in two (frames 17-21). The squeezing is also well illustrated by the horizontal velocity arrows in the bottom panels of Figure 5.4. For simplicity, in Figure 5.5 we only show the evolution of the rightmost fragment, whose field strength and CN intensity drops abruptly (green line up to frame 23). The decrease of the field strength in the resulting fragments leads to the increase of the area enclosed in the contour of constant magnetic flux (5.5 (a)). Small variations in the average LOS velocity accompany this process.

5.6.3 Coalescence and further fragmentation

At the end of the fragmentation phase the upper granule fades away and the surrounding granules start to fill the “empty” space (see frame 21 to 32 in Animation 2) soon afterwards. In this way, the three magnetic cores are advected to the wide space left by the fading granule, and compressed by the surrounding granules until they merge into a single magnetic element (frame 32 in Figure 5.4). The advection of magnetic cores by the proper motions of the neighboring granules is also well illustrated by the horizontal velocity flow field. During this compression phase a strong downflow is detected within the rightmost magnetic core (frame 28) and a small upflow in its surroundings (frame 32). As soon as the down-

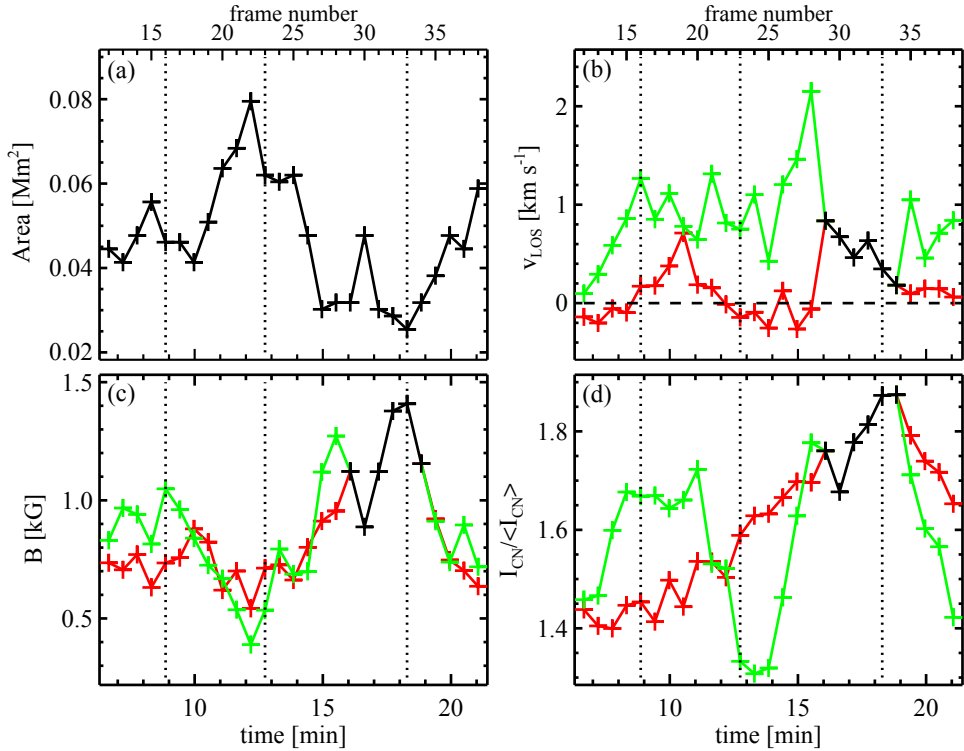


Figure 5.5: Evolution of relevant quantities with full temporal resolution, for frames 11-38. (a): the area within the black contour (enclosing a time-independent magnetic flux of 2.9×10^{17} Mx). The x-axis at the top of the panel marks the frame numbers. (b) LOS velocity. (c) magnetic field strength. (d) CN intensity. The plots display values of the corresponding quantities averaged over nine pixels centered around the centroid of the magnetic cores in the longitudinal magnetic field maps. Red (green) lines stand for the leftmost (rightmost) magnetic core and the black line is used when a single magnetic core is observed.

flow appears, a new co-spatial bright feature is detected in the Ca II H image (Animation 2). The almost co-temporal upflow that emerges at the periphery of the magnetic structure also appears co-spatial to the Ca II H BP.

The coalescence process takes place from frame 23 to 33 (Figure 5.5). Within these 5 minutes, the magnetic fields are concentrated and, because the flux is conserved, the area decreases while the field strength increases. The magnetic field reaches a strength of up to 1.4 kG, compared with the initial ~ 600 G of each magnetic core. Simultaneously, the CN intensity is also enhanced nearly in phase with the field strength. The plasma within the leftmost core is approximately at rest on average while the LOS velocity increases from 1 to 2 km s^{-1} within the rightmost core. Note, however, that our 9-pixel average LOS velocity

can be misleading. The apparent decrease in v_{LOS} for the coalesced structure results from the simultaneous presence of a downflow (in the inner core) and an upflow (at its periphery).

The evolution continues with a new fragmentation process. In a time interval of about 3 minutes, the magnetic element splits in two (see frame 37 in Figure 5.3 or Animation 2) and the different physical quantities are almost restored to their values prior to the coalescence phase (Figure 5.5).

5.7 Magnetic field oscillations

Driven by the local granular convective flows, the sequence of intensification, fragmentation and coalescence events described above occur all along the evolution of the multi-cored magnetic structure. This evolutionary behavior results in oscillations of its constant magnetic flux area (Figure 5.5 (a)). Similar magnetic field oscillations were first detected in four quiet-Sun magnetic patches by [Martínez González et al. \(2011\)](#) within IMAx data. They argued that the periods associated with this oscillatory pattern could be related with characteristic oscillation modes of flux tubes or, might correspond to the forcing by granular motions. Due to their compatibility with the granular lifetime and the fact that the oscillations can be strongly damped or amplified and their period abruptly modified, they favor the latter scenario.

Here, we wonder if the oscillations found by [Martínez González et al. \(2011\)](#) have also something to do with the evolution of our multi-cored magnetic structures. With the purpose of answering this question, in Figure 5.6 we display the time evolution of the longitudinal magnetic field for the four magnetic patches analyzed by them. We find that at least three of them (if not all four) are indeed multi-cored magnetic structures. The one displayed in the top row also shows hints that at some point it may be composed of at least two magnetic cores (see panels at 11.1 and 17.7 minute). However, this is not that evident as in the other three cases.

According to our new analysis, the oscillations of the three multi-cored magnetic structures can be explained through the intensification, coalescence and fragmentation processes that their inner cores suffer when they are continuously buffeted by granular flows. The damping and amplification phenomenon of oscillations and the strong changes in their periods might be caused by the changes in the number of magnetic cores contained within the structure, and by the fact that some of the fragments fade into a more diffuse magnetic field below our observational threshold (see e.g., the evolution of the magnetic feature in the second row).

It seems evident that the oscillations in at least three of the four magnetic structures are compatible with the forcing by granular motions. However, it may still be possible that

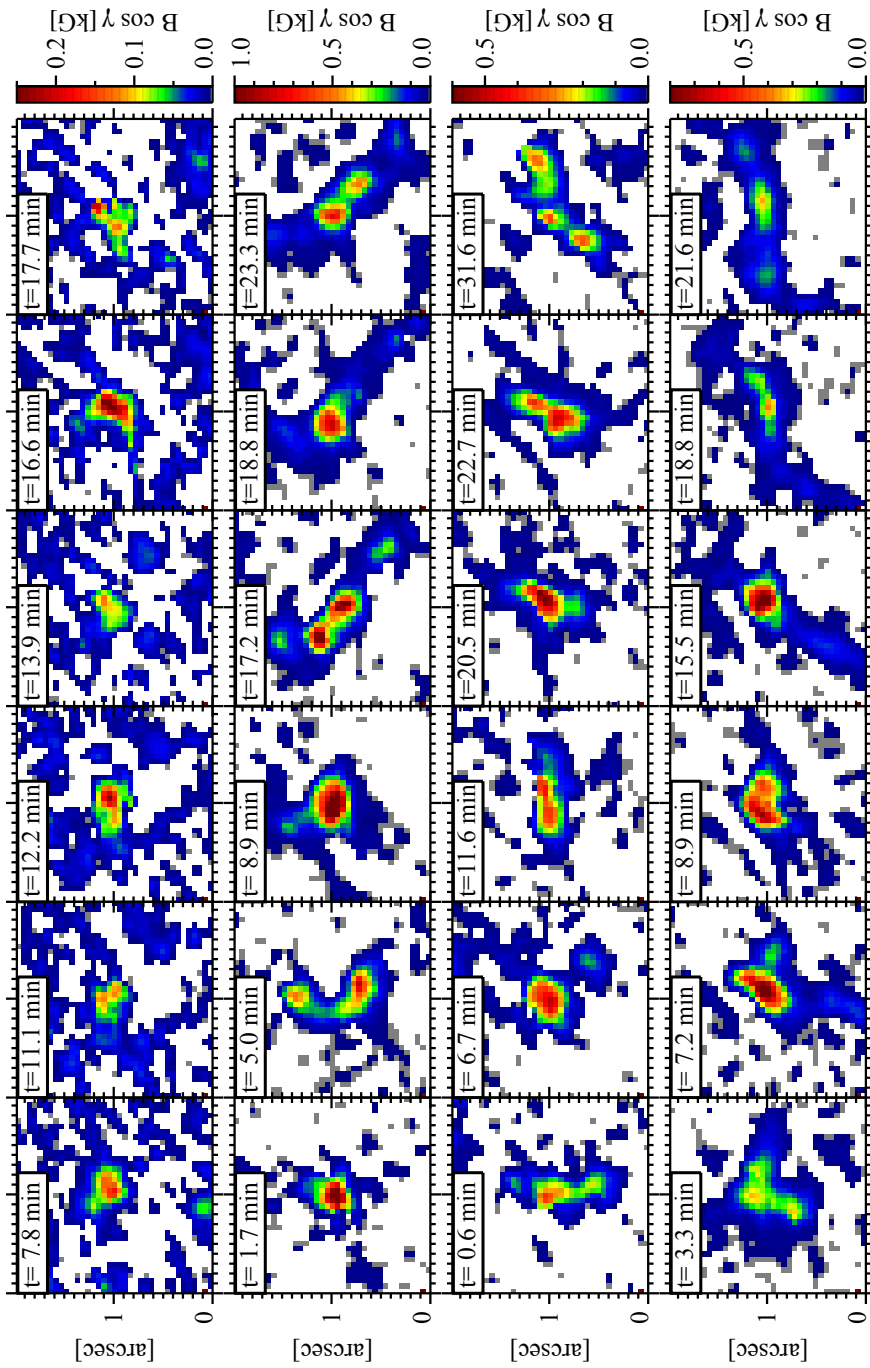


Figure 5.6: Evolution of the longitudinal magnetic field of the four magnetic structures analyzed by Martínez González et al. (2011). The structure at the top row is located within the blue solid square in Figure 5.1. The other tree features corresponds to other IMaX time series and consequently their location is not shown in Figure 5.1.

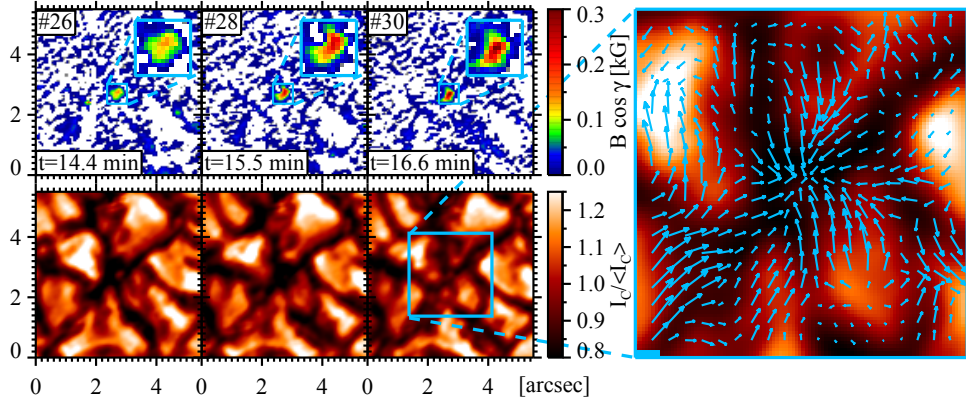


Figure 5.7: Closeup of one of the intensification phases of the magnetic structure in the top row of Figure 5.6. The structure is located within the blue dashed square in Figure 5.1. First row: longitudinal magnetic field. Second row: continuum intensity. The rightmost panel shows the horizontal velocity maps derived through the LCT technique averaged over the intensification phase. The length of the blue bar at the lower left corner of the rightmost panel corresponds to 1.8 km s^{-1} .

oscillatory modes are present in the evolution of the magnetic structure in the first row of Figure 5.6. In order to dispel these doubts we analyze the interaction of this feature with convection. With this purpose in mind we show one of the intensification events undergone by this feature in Figure 5.7. In the first panel, the magnetic element is located in a wide space left by granules. The magnetic structure become stronger as it is compressed between the granules. During this process the surrounding granules elongate in the direction of the magnetic feature, thus forming a characteristic daisy-like pattern first described by Muller et al. (1989). The compression process is well characterized by the horizontal velocity flows (rightmost panel in Figure 5.7), which point toward the magnetic feature near the center of the FOV. This shows that the oscillations correspond also in this case to the forcing by granular motions, as the magnetic feature is intensified at each of the recurrent granule compression phases.

5.8 Discussion and conclusions

We have presented direct observations of small-scale magnetic field dynamics in the quiet-Sun. This has been done with the accurate polarimetric measurements and high spatial resolution images obtained with the IMaX and SuFI instruments aboard the SUNRISE balloon-borne stratospheric mission.

The results reported about several vertical magnetic cores surrounded by a common more horizontal magnetic structure suggest that we are witnessing a collection of flux concentrations in the lower photosphere that share a common canopy in the upper photospheric layers. In the photosphere, intensification, fragmentation and coalescence processes play an important role in the evolution of the individual magnetic elements. This evolution is consistent with that of their photometric counterparts (BPs) as described by [Muller & Roudier \(1992\)](#), [Roudier et al. \(1994\)](#) and [Berger & Title \(1996\)](#).

The fragmentation and merging episodes appear to be governed by the evolution of the local granular convection flows. Magnetic cores have been observed to fragment when they are “squeezed” or “compressed” by converging or expanding granules. The fragmentation of magnetic cores through the perturbation of surrounding granules may be evidence for the action of the interchange, or fluting, instability in magnetic elements. The liability to the interchange instability is indeed an inherent property of flux tubes as first noticed by [Parker \(1975\)](#) and [Piddington \(1975\)](#). The fact that the magnetic fragments share a common canopy strongly supports the theoretical predictions of [Bünte \(1993\)](#). His idealized model contended that magnetic slabs are liable to fluting in a limited height range around $\tau_c = 1$, i.e., around the solar surface. Thus, a sheet-like magnetic structure fragments into tube-like filaments. Higher up in the atmosphere, however, the single magnetic tubes lose their individual identity as they expand with height and merge into a single, stable magnetic canopy. He also conjectured that the continuous advection of the tubes back to intergranular lanes by converging granular motions might prevent further dispersion through hydrodynamic drag.

We have also observed that soon after the splitting takes place, the resulting fragments are quickly regrouped again in intergranular lanes by the converging surrounding granules. Since the flux concentration cools the surrounding gas, it enhances the granular flows towards it ([Deinzer et al. 1984](#)). This effect keeps the multi-cored magnetic structure together during the entire 23 minute dataset. In the light of this spectropolarimetric picture, it is understandable that groups of BPs can persist for long times (up to 70 minute according to [Berger et al. 1998](#)) while being constantly buffeted by granules.

The quantitative analysis shows that the total magnetic flux of a typical multi-cored magnetic structure remains roughly constant during its evolution. We obtain this result as we are able to spatially resolve (at least partially) this magnetic structure. We are then enabled to relate the enhancement (decrease) of the CN BP brightness during the intensification and coalescence (fragmentation) phases with the increase (decrease) of the magnetic field strength and not with changes in the local filling factor as proposed by [Viticchié et al. \(2009\)](#). It is worth noting that in contrast to them with the spatial resolution of the SUNRISE/IMaX data ($\sim 0''.15$), we can get rid of the filling factor ([Lagg et al. 2010](#)). This correlation between the brightness and the field strength supports the classical picture of magnetic element radiance

by the hot-wall mechanism. Accordingly, the reduced gas pressure within the flux tubes locally depresses the optical depth unity level. The less opaque magnetic flux-tube interior then causes an excess of lateral inflow of radiation into their evacuated interiors (Spruit 1976; Deinzer et al. 1984), and as a consequence the magnetic elements appear brighter than their surroundings.

In addition, as a consequence of the flux conservation, the continuous intensification, coalescence and fragmentation of magnetic cores results in oscillations of the magnetic field strength and cross-section area of the entire magnetic feature. Such oscillations were first detected in four quiet-Sun magnetic patches by Martínez González et al. (2011). We have found that three of them are indeed multi-cored structures, while the fourth one may have sub-resolution structure. In all these features (and in other multi-cored magnetic structures) the compression by surrounding granules plays an important role in the intensification of the magnetic field. In Chapter 4 we already observed a large-amplitude variation in area and field strength within a magnetic element related to similar granule compression processes. However, due to the limited length of the observation only a single period was seen, and therefore we could not confirm that these variations were part of an oscillatory pattern.

The excitation of the oscillations is consistent with the forcing by granular motions. The pattern we observe corresponds to the evolution of magnetic flux concentrations, whose internal structure change as they are perturbed by granular flows. Through this interaction the magnetic structures are continuously being compressed, fragmented, or their different components regrouped and hence the magnetic fields are constantly being strengthened or weakened.

These magnetic field variations could explain the fact that brightness enhancements are observed at BPs when compressed by converging granules (Muller & Roudier 1992). They could also be the cause for the broad range of field strengths found at BPs by Beck et al. (2007b), p.165.

When the magnetic structure is compressed, kG field strengths are sometimes reached at the same time that strong photospheric downward motions are found within the magnetic cores. Such a correlation has been interpreted as a convective collapse by different authors (e.g., Nagata et al. 2008; Danilovic et al. 2010a). Our findings, then, suggest that convective collapse could be triggered by granular perturbations.

The highly dynamic nature of small-scale magnetic fields found here suggests the generation of waves that could propagate up through the solar atmosphere. This is supported by the chromospheric activity that we have detected during the intensification, coalescence and fragmentation processes related with photospheric downward and upward motions. Correlation between photospheric downflows and Ca II H brightenings has been explained in terms of the convective collapse process (Shimizu et al. 2008; Fischer et al. 2009), and as disk-

center photospheric traces of type II spicules (Quintero Noda et al. 2014). We did not find, however, any previous mention in the literature of a relationship between Ca II H brightness and photospheric upflows as found here. In the chromosphere, high plasma velocities in the blue wing of Ca II IR line have been first found by Langangen et al. (2008) as the disk counterpart of type II spicules. Could the photospheric upflows that we observe here have something to do with those seen in the chromosphere? Further investigations using time series observations of comparable spatial resolution and polarimetric sensitivity at the photosphere, together with simultaneous spectroscopic information on the chromosphere, are to shed new light on these issues.

ON THE RELATION BETWEEN MAGNETIC FIELDS AND CONVECTIVELY DRIVEN SINKS IN THE QUIET SUN

The relation between mesogranular convective flows, localized downdrafts and magnetic fields is studied. We use high spatial resolution spectropolarimetric data acquired with the Imaging Magnetograph eXperiment on board SUNRISE. We obtain the horizontal velocity flow fields of two quiet-Sun regions ($31.2 \times 31.2 \text{ Mm}^2$) via local correlation tracking. We identify the mesogranular lanes and the central position of sinkholes using passively advected tracers. 131 sinks located at the mesogranular vertices are detected. 35 % of the total sample are vortices with a median vertical vorticity of $\sim 0.06 \text{ s}^{-1}$, which corresponds to a period of rotation of some 3.5 minutes. The spatial distribution of magnetic fields in the quiet Sun is examined quantitatively at the same time. We find that the 50 % of the pixels with longitudinal magnetic fields higher than 600 G are located in the near neighborhood of sinkholes. This amount increases up to 95 % for magnetic fields above $\sim 1200 \text{ G}$ when a magnetic network feature is present in one of the observed regions. Meanwhile the small-scale magnetic loops detected by Martínez González et al. at the same two observed areas do not show any preferential distribution at mesogranular scales. The evolution of two such magnetic loops shows how the footpoints are advected by exploding granules toward the mesogranular boundary and in particular toward mesogranular vertices where the strongest downdrafts and magnetic fields are observed.

6.1 Introduction

Quiet-Sun magnetic fields evolve in the solar surface driven by convective motions. The largest magnetic structures outline the boundaries of supergranular cells —the magnetic *network*. Between them, smaller magnetic flux concentrations permeate the solar *internetwork*. Inside the supergranular cells magnetic elements with mixed polarities are seen to concentrate in mesogranular lanes (Yelles Chaouche et al. 2011) rather than in intergranular ones (e.g., Lin & Rimmele 1999), and a significant fraction of the magnetic flux emerges to the surface cospatially with granules in the form of small-scale magnetic loops (Martínez González et al. 2007; Centeno et al. 2007; Martínez González & Bellot Rubio 2009; Martínez González et al. 2010, 2012a).

Convection displays highly localized sinks where cold plasma returns to the solar interior (Spruit et al. 1990; Stein & Nordlund 1998). Due to conservation of the angular momentum, a vortex can be formed as the plasma approaches the downdraft (the *bathtub* effect, Nordlund 1985). The plasma can also drag magnetic fields toward the draining point, where they can be intensified up to kG values (Danilovic et al. 2010a; Kitiashvili et al. 2010). As a consequence, large amount of vorticity can be generated through interaction between plasma and magnetic fields in the intergranular junctions (Shelyag et al. 2011). Vertical vorticity is known to concentrate preferentially in negative divergence areas, i.e. downflow regions (Wang et al. 1995b; Pötzi & Brandt 2005, 2007). Vortex flows are observed at large scales (up to 20 Mm, Brandt et al. 1988; Attie et al. 2009) in supergranular junctions and at smaller scales ($\lesssim 0.5$ Mm, Bonet et al. 2008, 2010; Vargas Domínguez et al. 2011) in granular ones. Small-scale whirlpools are also visible in the chromosphere (Wedemeyer-Böhm & Rouppe van der Voort 2009) and their imprints have been identified in the transition region and low corona (Wedemeyer-Böhm et al. 2012).

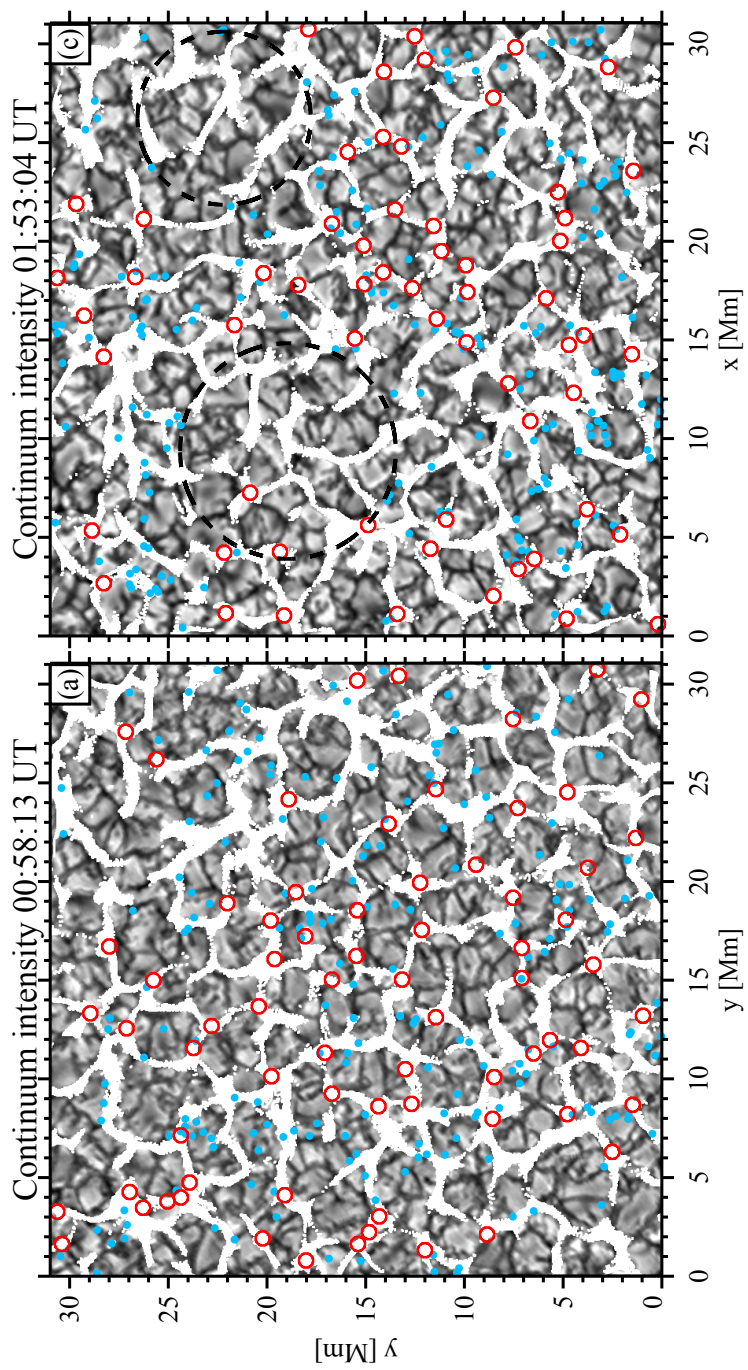
Vortex flows which harbor magnetic fields are rather abundant (Bonet et al. 2010). In particular, Balmaceda et al. (2010) showed evidences of small-scale magnetic concentrations being dragged toward the center of a sinkhole. The same event was further studied by Vargas Domínguez et al. (2015), who found sudden downflows and intensification processes of the magnetic concentrations. Manso Sainz et al. (2011) found that the trajectories of some small-scale loop footpoints describe a vortical motion suggesting that they can be engulfed by a downdraft. Finally, in Chapter 4 observed a loop footpoint being advected and concentrated in a sinkhole together with other same polarity weak magnetic patches. All these papers strengthen the idea that strong localized downdrafts are places where the concentration of magnetic fields is favored. In order to confirm such a relation quantitative and statistical information is still required.

The aim of this work is to provide such quantitative bases for the association between convectively driven sinks and small-scale magnetic fields in the quiet Sun. We use spectropolarimetric observations from the Imaging Magnetograph eXperiment (IMaX; [Martínez Pillet et al. 2011a](#)) on board the SUNRISE balloon-borne solar observatory ([Solanki et al. 2010](#); [Barthol et al. 2011](#)). IMaX provides stable time series of both intensity and polarization filtergrams at high spatial resolution (~ 100 km), which makes it the most suitable, currently available instrument for our study. Using the same SUNRISE/IMaX data, [Yelles Chaouche et al. \(2011\)](#) clearly demonstrated that magnetic elements are preferentially located in mesogranular lanes rather than in intergranular ones. On the other hand, [Bonet et al. \(2010\)](#) observed a large number of magnetic features swirling in convectively driven vortex flows. They detected vortices from the horizontal velocities obtained through local correlation tracking of magnetograms and other IMaX images. They found a mean duration of about 7.9 minutes and several events appearing at the same location all along the time series. The recurrent events were also observed in the flow field maps when averaged over the entire data set. In the present Chapter we find that such long-living sinks are located in mesogranular junctions and that they are places where the strongest magnetic fields tend to concentrate. We also study the evolution and the spatial distribution of magnetic loops at mesogranular scales.

6.2 Observations

We use high-quality spectropolarimetric data obtained with IMaX, which is a dual-beam imaging spectropolarimeter with full Stokes vector capabilities at the Fe I line at 525.02 nm (Landé factor $g = 3$). The line is sampled by a Fabry–Pérot interferometer at five wavelength positions taken at $\lambda = -8, -4, +4, +8,$ and $+22.7$ pm from the line center. The polarization analysis is then performed by two liquid crystal variable retarders (LCVRs) and a beam splitter. The image sequences were recorded over a disk-center, quiet Sun area on 2009, June 9. We analyze two different time series, namely, S_1 : 00:36:03 to 00:58:46 UT (22.7 minutes) and S_2 : 01:31:54 to 02:02:29 UT (32.1 minutes), with a cadence of 33.25 s, and a spatial sampling of 39.9 km.

The science images were reconstructed through phase diversity ([Gonsalves 1982](#); [Paxman et al. 1996](#)) as described by [Martínez Pillet et al. \(2011a\)](#). This procedure effectively reduces the IMaX field of view (FOV) down to about $43'' \times 43''$ (31.2×31.2 Mm²). After reconstruction, the spatial resolution has been estimated to be $0.''15$ – $0.''18$ and the noise level in each Stokes parameter is about $3 \times 10^{-3} I_c$ (I_c being the continuum intensity). We recover information of the vector magnetic field through inversions of the full Stokes vector using the SIR code ([Ruiz Cobo & del Toro Iniesta 1992](#)) as described in Section 3.2. Constant



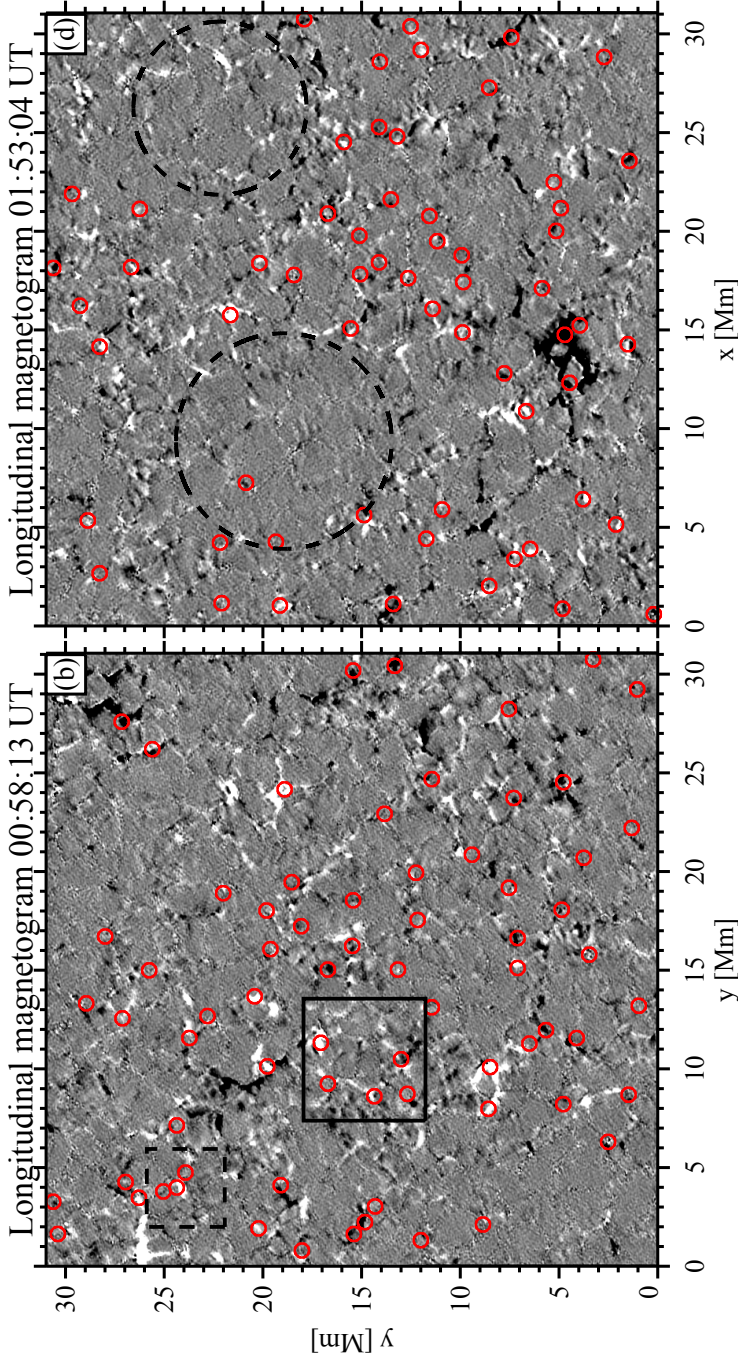


Figure 6.1: Top panels: white pixels represent locations where $\rho_{\text{corok}} \geq 2$ coroks pixel^{-1} at $t = 21.6$ minutes and its 1 pixel neighborhoods for time series S_1 (a) and S_2 (c), respectively. The background image is the continuum intensity at $t = 21.6$ minutes. Bottom panels: the longitudinal component of the magnetic field, $B \cos \gamma$, at $t = 21.6$ minutes (saturated at ± 50 G) for the time series S_1 (b) and S_2 (d), respectively. Red circles (with a radius of 9 pixel ~ 360 km) represent the position of the 131 sunspots. Blue filled circles show the average position (between both footpoints) of the small-scale loops detected by [Martínez González et al. \(2012a\)](#). The two areas delineated by the dashed circles mark two *dead calm* regions found by [Martínez González et al. \(2012a\)](#). The black dashed box represent the regions analyzed in Chapter 4. The black solid rectangle, with a FOV of $6.2 \times 6.2 \text{ Mm}^2$, illustrate the area used in Figure 6.4.

values for the three components of the magnetic field and LOS velocity are assumed. From the magnetic field strength B and the inclination γ we derive the longitudinal component of the magnetic field (hereafter referred to as the longitudinal magnetogram) $B_{\text{long}} = B \cos \gamma$.

6.3 Sink detection and statistics

6.3.1 Mesogranular lane identification

Mesogranulation is a horizontal cellular flow pattern revealed through the LCT technique when applied to intensity images of the solar granulation (November et al. 1981; Simon et al. 1988; Title et al. 1989; Brandt et al. 1991; Muller et al. 1992; Roudier et al. 1998; Yelles Chaouche et al. 2011). Here we reproduce this pattern by using the continuum intensity filtergrams of the two entire data sets. We use a common time coverage for both time series, namely, the total duration of series S_1 (the shortest one), series S_2 , hence, reduces to its first 42 snapshots. We apply a p-mode subsonic filter (Title et al. 1989) to remove the characteristic 5-min solar oscillations. This process degrades the first and the last frames, which are deleted from our time series. The final data sets last, therefore, 21.6 minutes. We employ the LCT technique (November & Simon 1988) as implemented by Molowny-Horas & Yi (1994) to obtain the mean horizontal velocity field averaged along the whole duration of the data sets. This technique correlates small local windows in consecutive images to find the best-match displacement. The tracking window is defined by a Gaussian function with a FWHM=600 km. After measuring the horizontal velocity vector $\mathbf{v} = v_x + v_y$, we also compute the flow divergence $\nabla \mathbf{v} = \frac{\partial v_x}{\partial x} + \frac{\partial v_y}{\partial y}$ and vertical vorticity $(\nabla \times \mathbf{v})_z = \frac{\partial v_y}{\partial x} - \frac{\partial v_x}{\partial y}$.

We outline the location of intermesogranular lanes (called here mesolanes for short) by using passively advected tracers (*corks*), which are usually used to trace the evolution of plasma motions (see, e.g., Yi 1992; Márquez et al. 2006). Initially, a cork is located at each pixel of the image. They are advected by surface motions whose mean horizontal velocity field is computed. We count the number of corks at each pixel to obtain the cork density function, ρ_{cork} (Yelles Chaouche et al. 2011). At the end of the series ($t = 21.6$ minutes) we define the mesolanes as those locations where $\rho_{\text{cork}} \geq 2$ plus 1-pixel wide neighborhoods. These areas are shown in Figure 6.1 (a) and (c) through white pixels overlaid over the continuum intensity images at $t = 21.6$ minutes for time series S_1 and S_2 respectively. These white regions clearly delineate a fully developed network of mesogranular cells (5-10 Mm of size, November et al. 1981).

6.3.2 Sink identification

The mesogranular pattern is visible after only ~ 20 minutes, when most of the corks have already converged to mesolanes (Yelles Chaouche et al. 2011). However, if the corks are left to be advected even longer, they finally end up in well localized places at the central position of sinkholes. We obtain therefore the locations of persistent sinks, which appear in the mean flow corresponding to the full time series. These long-lasting sinkholes are produced by either recurrent sinks appearing nearly at the same location, or by sinks strong enough for not being smoothed away by the LCT temporal average. We identify a total of 131 sinks within both observed regions. Taking into account the spatial area covered by each FOV, we get an occurrence rate of 6.7×10^{-2} sinks Mm^{-2} .

6.3.3 Sink classification

In previous studies, small whirlpools have been first detected as swirling motions of bright points (Bonet et al. 2008), and later from LCT horizontal velocities of magnetograms (Bonet et al. 2010) and G-band images (Vargas Domínguez et al. 2011). In the same way as in here, Vargas Domínguez et al. (2011) applied LCT to the whole FOV and duration of two G-band time series (20 minutes each) acquired with the Swedish 1-m solar telescope. By visual inspection of the horizontal flow field maps, they identify individual vortices as those locations where the horizontal velocity vectors converge to a central point and form a swirl. They found these regions coincident with the final destination of corks. However they detected many other places where the corks get accumulated without any apparent swirling motion.

Here we inspect both the horizontal flow maps and the cork movies to analyze all the detected sinkholes. We realize that the corks follow different trajectories on their way to being engulfed by the sinks. Sometimes they converge radially, while other times they trace a spiral path as they fall into the downdrafts. In Figure 6.2 we display the horizontal velocity maps for these two different type of sinkholes. In the left panel, the vectors point radially towards the center of the image, while in the right panel, they display a swirl. We shall hereafter refer to them as *uniform sink flows* and *vortex sink flows*, respectively. In this regard, it is worth mentioning that, according to our criterion the convective vortex region reported by Balmaceda et al. (2010) and Vargas Domínguez et al. (2015) is indeed a uniform sink flow.

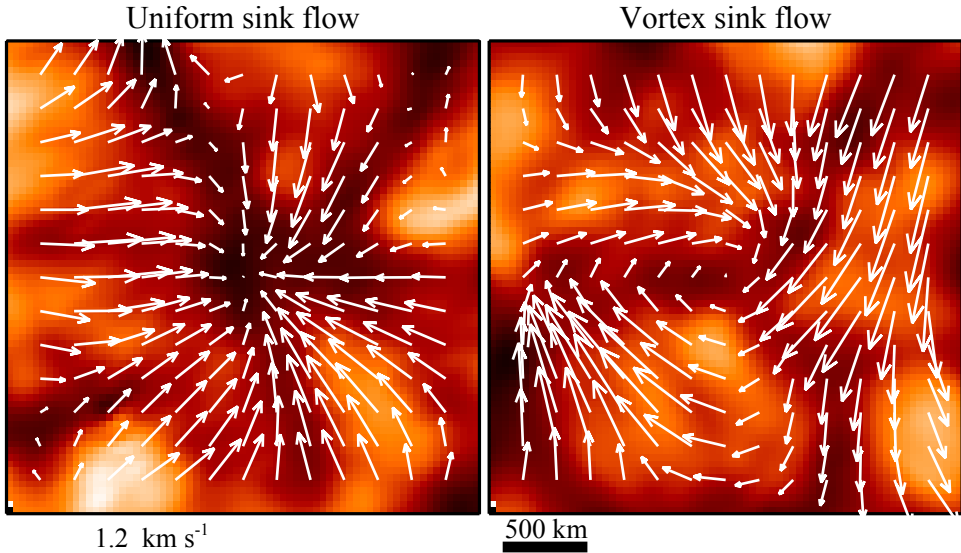


Figure 6.2: Two examples of sinks detected in the IMAx data. The background images represent the continuum intensity average over the whole time series in false color. The white arrows represent the horizontal velocity vectors obtained from LCT. The left panel shows an example of a uniform sink flow where velocity vectors are radially pointing towards the center of the image. The right panel displays a vortex flow where the velocity vectors exhibit a swirl motion with a clockwise sense of rotation.

6.3.4 Sink statistics

We detect 46 vortex sinks (35 % of the total sample) and 85 uniform sinks. These result in occurrence rates of 2.4×10^{-2} vortices Mm^{-2} and 4.4×10^{-2} uniform sinks Mm^{-2} , respectively. Our values for vortices is ~ 1.8 times larger than the number obtained by Vargas Domínguez et al. (2011) of $1.1\text{--}1.5 \times 10^{-2}$ vortices Mm^{-2} .

In Figure 6.3 we display the divergence (left-panels) and the vertical vorticity (right-panels) histograms at the central pixel of the sinks. As expected, all the sinkholes (panel (a)) are located in negative divergence areas with a median value of -0.07 s^{-1} . The divergence distribution is very similar for both vortex sinks (panel (e)) and uniform sinks (panel(c)) with a 25% smaller mean value for the former, suggesting that vortex sinks are (25%) less vigorous than uniform ones. The distribution of the vertical vorticity is completely different. We find a strong peak centered at zero values for uniform sinks (panel (d)), while the distribution for vortex flows (panel (f)) reveals two humps shifted to negative and positive values, respectively. Panel (d) shows that most of the uniform sinks have very low vorticity, whereas the negative and positive humps in panel (f) are produced by the distribution of

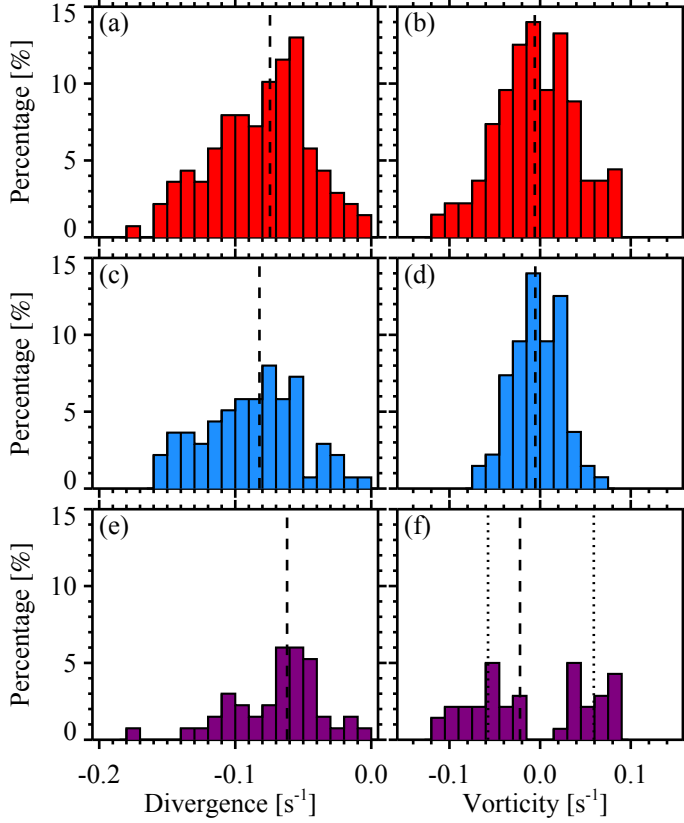


Figure 6.3: Histograms of the divergence (left-panels) and the vertical vorticity (right-panels) obtained from LCT proper motions at the centers of the sinks. Panel (a) divergence and (b) vertical vorticity at all 131 sinks. Panel (c) divergence and (d) vertical vorticity at 85 uniform sink flows. Panels (e) divergence and (f) vertical vorticity at 46 vortex flows. The vertical dashed lines indicate the median values of the distributions. In panel (f) the left and right vertical dotted lines mark the median value of the clockwise and counterclockwise vortices respectively.

whirls with clockwise and counterclockwise sense of rotation, respectively. Both clockwise and counterclockwise vortices have a median of the absolute vertical vorticity of 0.06 s^{-1} . In a pure rotational motion of the plasma $(\nabla \times \mathbf{v})_z = 2\omega$ (ω being the angular velocity), a vertical vorticity of 0.06 s^{-1} corresponds to a rotation period of 3.5 minutes. We find a slightly larger number of clockwise (54 %) than counterclockwise motions (46 %) but the difference is not significant in view of the number of studied events.

6.4 Correlation between mesogranules, sinks, and magnetic fields

In Figure 6.1 we show the distribution of sinks (red circles) over the continuum intensity images and longitudinal magnetograms of the two observed areas at $t = 21.6$ minutes. White pixels in the continuum intensity images represent the distribution of corks delineating the mesolanes. The sinkholes show a mesogranular distribution as they are located at the junctions of multiple mesogranular lanes. However, their spatial distribution is not completely uniform and there are some extended areas with lack of detected sinkholes. There are two particularly prominent regions in time series S_2 (Figure 6.1 (c) and (d)). Interestingly they are coincident with the *dead calm* areas found by Martínez González et al. (2012a). Such areas are characterized by having very low magnetic activity and lack of small-scale magnetic loops. In Figure 6.1 (c) and (d) the dashed circles mark the two most prominent dead calm regions found by Martínez González et al. (2012a). These two regions contain several mesogranules within them but only a single sink is observed in the largest void. The spatial distribution of the sinks at the longitudinal magnetograms (Figure 6.1 (b) and (d)) also reveal that many sinkholes harbor magnetic fields.

From visual inspection of the sinkholes and the study of individual examples (e.g., Bonet et al. 2010, Chapter 4), we obtain indications that the magnetic field concentrations are preferentially located at well localized sinkholes. In order to obtain quantitative estimations we build a binary mask by defining sinks as 6 pixel (~ 240 km) radius circles plus 3 pixel neighborhoods. This 240 km value corresponds to the mean radius found for vortex flows by Vargas Domínguez et al. (2011). Using the same IMAx data as in here, Yelles Chaouche et al. (2011) proved quantitatively that the longitudinal magnetic field is concentrated in mesogranular lanes rather than in intergranular ones. As a reference here, we also count the number of magnetic concentrations located at mesolanes and mesogranules. The latter are considered those areas in the FOV that are not covered by mesolanes (defined in Section 6.3.1). We remove from our analysis the prominent positive patch appearing at the top-left edge of the time series S_1 (Figure 6.1 (b)). This magnetic structure enters partially into the FOV during the course of the time series, and it is located at the edge where the horizontal flow fields are not properly determined.

The frequency distribution (in percent) of pixels with $|B_{\text{long}}|$ larger than a given value is plotted in Figure 6.4 (a) taking into account the full time series in both observed areas. Different line colors indicate different locations, namely, green for mesolanes, blue for mesogranules, and red for sinkholes. Certainly, mesolane and mesogranule distributions add up to 100 % according to our definition. The distributions show that the magnetic field are

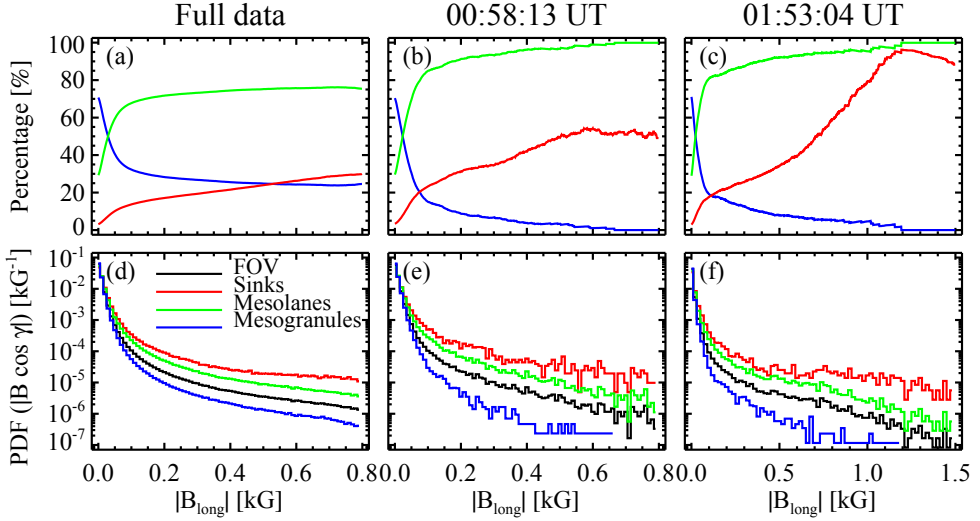


Figure 6.4: Top panels: percentage of pixels with $|B_{\text{long}}|$ above the value given in abscissas time-averaged along the two observed areas (a), at $t = 21.6$ minutes in time series S_1 (b) and S_2 (c). Bottom panels: probability density functions of $|B_{\text{long}}|$ time-averaged along the two observed areas (d), at $t = 21.6$ minutes in time series S_1 (e) and S_2 (f). The black, red, green, and blue solid lines stand for all pixels in the FOV, sinks, mesolanes, and mesogranules, respectively. These regions are defined in the text.

mainly located at mesolanes for strength larger than 100 G (green lines). A non-negligible amount of stronger fields are also found at sinks (red lines). Figure 6.4 (d) shows the corresponding probability density functions (PDFs) for sinks, mesolanes, mesogranules, and the whole FOV (black line). The PDFs show that the fraction of the area occupied by magnetic fields decreases with strength. Similar distributions are found in numerical simulations of quiet-Sun magnetoconvection (e.g., [Stein & Nordlund 2006](#); [Vögler & Schüssler 2007](#)).

The magnetic elements are evolving during the time series and thus the relation between mesolanes, sinks, and fields changes with time. Specifically, correlation increases as we approach to the end of the time series ($t = 21.6$ minutes) when mesolanes have been computed. In Figure 6.4 we also display the frequency distributions and the PDFs at that time for both observed regions. In agreement with [Yelles Chaouche et al. \(2011\)](#), 85 % of the pixels harboring fields with longitudinal component larger than 100 G are located in mesolanes. This result applies for the two time series (see panel (b) and (c)). Very remarkably, a large portion of the stronger fields (50 % for those with $|B_{\text{long}}| \gtrsim 600$ G) are located in the sinkholes or their close vicinity. In fact, in series S_2 , where a strong network feature is present, we see that almost all the pixels with $|B_{\text{long}}| \gtrsim 1200$ G are found in these convectively driven sinks (panel (c)). This large portion of quiet-Sun magnetic elements in sinkholes is even

more significant if the surface fraction covered by the latter is taken into account: 29 % of the observed area is covered by mesolanes, but only 3 % is occupied by sinks. Therefore, the probability for quiet-Sun magnetic field appearance in convectively driven sinks is the largest as shown in Figure 6.4 (e) and (f). In both time series, all the PDFs peak at 0 G, and then decrease rapidly toward stronger fields. This decrease is steeper for mesolanes than for sinks, and even more abrupt for mesogranules. All these measurements suggest that the magnetic fields in the quiet-Sun areas are preferentially located at well localized long-living downdrafts: it is more probable to find magnetic fields at sinks than at mesolanes in almost the whole range of strengths. Specifically, since the surface covered by sinkholes is only 10 % of that covered by mesolanes, that 50 % of field elements with $|B_{\text{long}}| \gtrsim 600$ G in sinkholes could be interpreted as if the probability for strong fields to be in sinkholes is 5 times as large as that in mesolanes.

At granular scales precious observations indicate that there is a continuous injection of magnetic flux in the form of small-scale magnetic loops (e.g., [Martínez González & Bellot Rubio 2009](#)). Exploring, then, whether any preferential location also applies to these loops is in order. In Figure 6.1 (a) and (c) blue filled circles show the distribution of the average position between both footpoints of each detected loop. The average initial distance between footpoints was found to be ~ 0.25 Mm. To have an idea of the surface area covered by loops, we build a binary mask by defining them as 0.25 Mm diameter circles around the average position between both footpoints. We count the number of pixels in both observed regions and find that 65.5 % of them are located at mesogranules, 34.5 % at mesolanes, and only 4.5 % at sinks. These values are close to those of the surface fraction covered by each region (71 % mesogranules, 29 % mesolanes, and 3 % sinks), suggesting that magnetic loops are homogeneously distributed on mesogranular scales except in the dead calm areas where no loop is seen to emerge ([Martínez González et al. 2012a](#)).

6.4.1 Mesogranule: a case study

In Figure 6.5 we zoom in on one of the mesogranules. Panel (a) shows the divergence map in colors and the overlaid white arrows display the horizontal flow field. The mesogranule is characterized by a strong positive divergence and a horizontal flow that goes from the center of the map outward. The time sequence of the continuum intensity in panel (d) reveals the recurrent appearance of exploding granules. The location of these granules prior to their fragmentation is marked by white arrows. Such families of repeatedly splitting granules can persist for long times (up to 8 hours; [Roudier et al. 2003](#)) and when averaged in time they give rise to positive divergences which are identified as mesogranules ([Roudier & Müller 2004](#)).

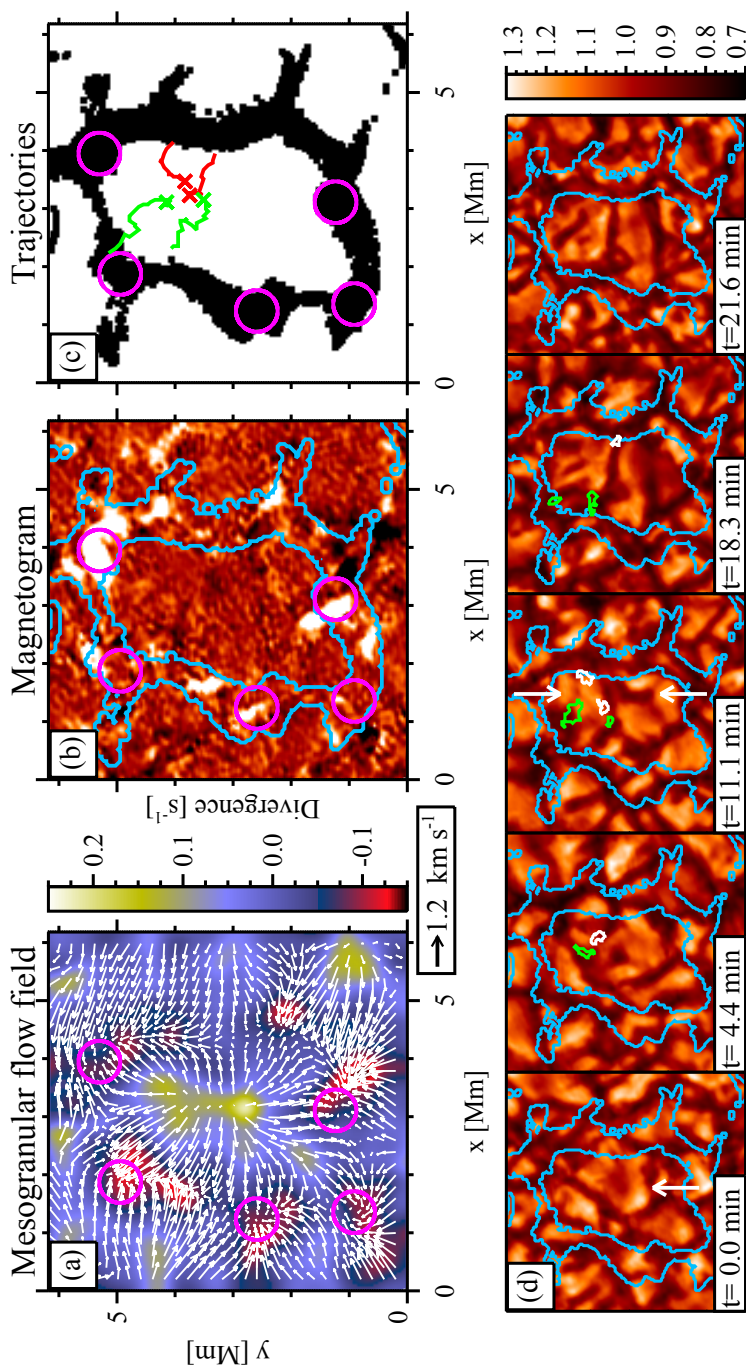


Figure 6.5: Closeup of a mesogranule. The area is located within the black solid rectangle in Figure 6.1. (a) divergence map (background image) and mesogranular flow field (white arrows). (b) longitudinal magnetogram at $t = 18.3$ minutes saturated at ± 50 G. Blue contours delineate the mesolanes. (c) mesolanes (black pixels) and trajectories followed by the footpoints of small-scale magnetic loops. Red and green paths refer to the positive and negative polarity footpoints, respectively. Cross marks indicate the initial position of the footpoints. Magenta circles (with a radius of 9 pixel ~ 360 km) represent the position of sinkholes. (d) a time sequence of the continuum intensity maps. Arrows indicate exploding granules. White and green contours represent positive and negative polarity patches, respectively.

In panel (b) a longitudinal magnetogram at $t = 18.3$ minutes is shown. The blue contours trace the mesolanes and the magenta circles display the location of sinkholes. Notice that in panel (a) the sinkholes are found at strong negative divergence areas in which the horizontal flows converge. In the magnetogram, the vast majority of the magnetic elements are located within the mesolanes and in particular inside or near sinkholes. As an example, in the bottom right sink two opposite polarity features are found and in the upper right one a prominent magnetic element is observed. The evolution of the latter one was studied in detail in Chapter 5. It contains multiple inner magnetic cores which are continuously being fragmented and merged driven by the evolution of surrounding granules. Here, we find that this structure is indeed anchored in a persistent downdraft. This constant inwards attraction may help maintain all the fragments together into a single magnetic structure.

In the interior of the mesogranular cell, smaller magnetic patches are also observed. These features are much weaker with a longitudinal magnetic field component smaller than 50 G. Some of them are identified as small loop-like structures as a linear polarization patch appears flanked by two opposite polarities. We track the evolution of their footpoints manually until they merge or cancel with other features or they fade away below the detection limit. We display their trajectories in panel (c). Red and green lines stand for positive and negative polarity patches and crosses indicate their initial position. Interestingly, they move radially toward the mesolanes, although they also describe a random motion at smaller scales. In panel (d) we also show the evolution of these patches over the continuum intensity maps. White and green contours represent positive and negative polarities patches, respectively. They appear located at the edge of granules and are swept to the mesogranular lanes as the granules expand and explode. The uppermost negative polarity patch reaches the periphery of a sinkhole where it is soon canceled out by an opposite polarity feature. These two structures are observed prior to their interaction at the border of the top left sink in panel (b). [Manso Sainz et al. \(2011\)](#) studied the trajectories of many small-scale loop footpoints and they found two instances in which the magnetic features describe a vortical motion. Those trajectories could easily be understood if they were particular cases where footpoints are engulfed by downdrafts. In fact, draining of weak fields has been observed in Chapter 4 inside the black dashed box in Figure 6.1 (b). In that Chapter, the weak magnetic patches (one of them identified as a loop footpoint) are advected to the center of a sinkhole, where they are confined and concentrated by converging granular flows up to ~ 1.5 kG. Similar events are also found in 3D simulations, where kG magnetic elements are formed at the vertices between neighboring granules ([Bushby et al. 2008](#); [Danilovic et al. 2010a](#)). Further confirmation of these results can settle low-lying, weak magnetic loops as the natural candidate to supply the necessary flux to form most quiet-Sun magnetic elements.

6.5 Discussion and conclusions

The accurate polarimetric measurements and high spatial resolution of the IMaX data allowed us to quantify the relation between quiet-Sun magnetic fields, mesogranulation, and convectively driven sink flows. We have computed the horizontal flow field through LCT of continuum intensity maps averaged over the whole duration of two time series. From the inferred velocity vectors, we have detected the mesogranular lanes and the central position of sinks by tracing the plasma flows with passively advected tracers. The sinkholes are preferentially located in the junction of multiple mesogranular lanes. According to the cork trajectories and the distribution of the converging flow fields we have found two types of sinks, namely, (1) uniform sink flows: radially symmetrical flow fields directed inwards to the sinkhole; and (2) vortex sink flows: flow fields rotating around the vertical axis. We have detected 131 long-living sinks, 65% belonging to type 1, and the rest to type 2. This results in an occurrence rate for vortex flows of 2.4×10^{-2} vortices Mm^{-2} , which is ~ 1.8 times larger than that found by [Vargas Domínguez et al. \(2011\)](#).

Vortices have a median vertical vorticity of $\sim 0.06 \text{ s}^{-1}$, which is one order of magnitude larger than the previous estimation found by [Bonet et al. \(2010\)](#) and [Vargas Domínguez et al. \(2011\)](#). However, [Bonet et al. \(2010\)](#) inferred vorticities from magnetograms, where the values are systematically smaller than in intensity images. A vorticity of 0.06 s^{-1} corresponds to a period of rotation of some 3.5 minutes. These values are of the same order of magnitude as those predicted by numerical simulations ([Stein & Nordlund 1998](#); [Danilovic et al. 2010a](#); [Moll et al. 2011](#); [Shelyag et al. 2011](#)). Simulations show that vorticity increases with increasing numerical resolution. The values found here agree better with numerical resolution values in the range of (100, 200) km (see Figure 31 in [Stein & Nordlund 1998](#)).

We have not found a preferred sense of rotation for the vortices (21 counterclockwise and 25 clockwise), compatible with [Bonet et al. \(2008\)](#) and [Vargas Domínguez et al. \(2011\)](#), but not with [Bonet et al. \(2010\)](#), who found a significant preference for counterclockwise sense of rotation. There are several reasons that can explain the discrepancy. First, their detection is based on magnetograms, where they look for magnetic structures that seem to rotate, while here we detect both magnetic and non-magnetic vortices. Second, they focus only in an *effective* FOV of $28''5 \times 28''5$, where the magnetograph signals are largest within the second time series analyzed here (see Figure 6.1 (d)). Third, they detected short-living vortices as well, which are diluted by the LCT temporal average in our analysis.

We have provided quantitative measurements of the relation between magnetic fields, mesogranules and sinks. A large amount (50%) of the magnetic elements with longitudinal magnetic fields above $\sim 600 \text{ G}$ are found within 360 km around sinkholes centers. This amount increases up to 95% for magnetic fields above $\sim 1200 \text{ G}$ when a prominent magnetic

patch, probably belonging to the network, is present in one of the time series. In contrast, we have found that 65.5 % of the 400 small-scale magnetic loops detected by [Martínez González et al. \(2012a\)](#) are located at mesogranules, 34.5 % at mesolanes, and only 4.5 % in the close neighborhood of long-living sinkholes. Certainly, these values are remarkably similar to that of the surface fraction covered by each region and we conclude that magnetic loops are homogeneously distributed on mesogranular scales.

We have analyzed the evolution of two particular loops appearing inside a mesogranule. Their footpoints passively follow the mesogranular horizontal flows, as they are swept by exploding granules. Through this process they reach the boundaries of the underlying mesogranules and even well localized sinkholes located at the vertices of mesogranular lanes. In such a downdraft they can be confined and concentrated up to kG values by converging granular flows ([Bushby et al. 2008](#); [Danilovic et al. 2010a](#), Chapter 4). The advection of weak fields by mesogranular horizontal flows and their concentration in mesogranular vertices is also supported by magnetoconvection models that study the interaction of convective flows with and imposed field (see e.g., [Stein & Nordlund 2006](#)). However, a small-scale dynamo can be consistent as well with the organization of strong flux concentrations at mesogranular lanes, provided that the computational domain is large enough ([Rempel 2014](#)). In fact, local dynamo is more efficient when the mesogranulation is also present ([Bushby & Favier 2014](#)), and the photospheric magnetic energy is doubled as a strong mesogranular network is formed ([Rempel 2014](#)).

At the light of our results we can conjecture a hierarchical picture for the evolution of quiet Sun magnetic fields: flux emerges preferentially at granules in the form of small-scale magnetic loops; the footpoints are first swept to nearby intergranular lanes ([Centeno et al. 2007](#)), and then advected further to mesogranular lanes, especially, to those junctions where long-living downdraft are formed. The concentration of weak fields in the mesogranular vertices gives rise to the so-called internetwork magnetic elements. If these magnetic elements are strong (long-lived) enough, then supergranular flows can swipe them ([de Wijn et al. 2008](#); [Orozco Suárez et al. 2012](#)), reach the supergranular boundaries and eventually contribute to the magnetic network flux ([Gošić et al. 2014](#)). This qualitative picture has been possible thanks to the stable, high-resolution, accurate polarimetric SUNRISE/IMaX observations. A statistical, quantitative verification of whether the magnetic flux of the smallest (weaker) scales is able to supply that of the internetwork in the same way as the latter does with the network magnetic flux ([Gošić et al. 2014](#)) needs further observations of the same quality that remain stable for longer time. They are a motivation for new balloon-borne mission like SUNRISE.

CONCLUSIONS

We have studied the evolution of quiet-Sun magnetic features based on high-quality spectropolarimetric observations. To this end we have employed high spatial and temporal resolution time series of polarimetric images at the diffraction limit of a 1-m telescope. The data have been acquired with the IMAx spectropolarimeter during the first flight of the SUNRISE balloon-borne mission.

We have applied the SIR inversion code to the four Stokes profiles of the Fe I line at 525.02 nm measured by IMAx. Through this process we have inferred the model parameters that characterize the solar photosphere such as the vector magnetic field and the line-of-sight velocity. In the inversion, we have assumed that the physical parameters are constant with depth. We have also applied the local correlation tracking technique to the time series of continuum intensity images. This has allowed us to derive the horizontal proper motions of the solar granulation. Therefore we have obtained horizontal velocity flow field maps, and from those we have computed the flow divergence and the vertical vorticity images.

First of all, we have reported on the formation and evolution of an isolated quiet-Sun magnetic element and its interaction with the neighboring convection. Seen at a scale of one hundred kilometers, we have found that this is a complex process where many phenomena are involved. The formation starts when a small-scale magnetic Ω loop with field strength of ~ 200 G emerges to the solar surface in a granular upflow. Its footpoints are soon swept to nearby intergranular lanes where some, weak positive polarity patches are already present. The negative polarity footpoint cancels out, likely through a reconnection process, with an opposite polarity feature. Meanwhile the positive polarity footpoint and the other remaining patches are advected by converging granular flows toward a long-living sink. The magnetic fields are confined and concentrated in the sinkhole and a magnetic element with

field strength (~ 500 G) in equipartition with the kinetic energy density of the convective motions is formed. The intergranular downflow then starts to increase within the magnetic feature and the surrounding granules compress the structure until the field strength increases up to ~ 1.5 kG values. During this process, a bright point (BP) appears at the edge of the flux concentration together with a co-spatial upflow feature. The evolution of the BP is closely related to that of the upflow as an anti-phase correlation between the continuum intensity and the line-of-sight velocity is observed. At the end of the intensification phase, strong downflow plumes, with speeds roughly up to 6 km s^{-1} , also develop at the periphery of the magnetic element. The gas required for producing such strong and narrow downdrafts is likely provided by converging granules. The development of the magnetic element does not stop here, and we have discovered that it is indeed unstable. The magnetic element displays an oscillatory behavior as the field strength weakens and rises again with time.

In summary, we can say that the history of our magnetic element encompassed three main phases, namely, (1) flux concentration in a long-living sink by granular advection; (2) evacuation by a downflow and intensification to kG strength by granular compression; and (3) unstable evolution of the mature magnetic element.

We have also investigated the dynamics of quiet-Sun magnetic features. Specifically, we have focused on those magnetic structures that appear associated with chains of bright points. The dynamical interaction of these features with the convective flows have been analyzed and we have drawn the following conclusions:

- These magnetic structures are resolvable into a series of more elemental inner magnetic cores, each of which appears related with a single bright point.
- The strong and vertical inner cores are surrounded by a common, weaker and more inclined fields, suggesting that we are witnessing a collection of flux concentrations in the lower photosphere that expand with height and merge into a common canopy in the upper photospheric layers.
- The evolution of the individual magnetic cores is completely governed by the local granular convection flows.
- They continuously intensify, fragment, and merge in the same way that chains of bright points in photometric observations have been reported to do.
- This evolutionary behavior results in magnetic field oscillations of the global entity.
- The magnetic field oscillations first reported by [Martínez González et al. \(2011\)](#) correspond to the forcing by granular motions and not to characteristic oscillatory modes of thin flux tubes.

Finally, we have studied the relation between mesogranular convective flows, localized downdrafts, and quiet-Sun magnetic fields. With this purpose in mind, we have first identified the mesogranular lanes and the central position of sinkholes. We have detected 131 sinks at the junctions of multiple mesogranular lanes. We have found two types of sinks, namely, (1) uniform sink flows displaying radially symmetrical converging flows; and (2) vortex sinks flows that manifest as whirlpools. Their main properties are:

- The sinkholes are located in negative divergence areas with a median value of -0.07 s^{-1} .
- The vortex flows have a median vertical vorticity of $\sim 0.06 \text{ s}^{-1}$, which corresponds to a period of rotation of some 3.5 minutes.
- The vortices do not show a preferred sense of rotation with 46% being counterclockwise and 54% clockwise.

We have also provided quantitative measurements of the spatial distribution of magnetic fields. We have found that the 50 % of the pixels with longitudinal magnetic fields above $\sim 600 \text{ G}$ are located within sinkholes. The probability to find such magnetic fields at sinkholes is 5 times as large as that in mesogranular lanes. From these results we have concluded that the strongest magnetic structures tend to concentrate at well localized long-living downdrafts at the mesogranular junctions. Among them are the magnetic elements studied in Chapter 4, and the multi-cored magnetic structure analyzed in detail in Chapter 5. Meanwhile the small-scale magnetic loops do not show any preferential distribution at mesogranular scales. However, we have observed that the footpoints of magnetic loops appearing inside the mesogranules can be advected by horizontal mesogranular flows toward the mesogranular boundaries and in particular to their vertices.

All these results could be understood in a single evolutionary path: Flux emerges preferentially at granules in the form of small-scale magnetic loops. The footpoints are first swept to nearby intergranular lanes, and then advected further to mesogranular lanes, especially, to those junctions where long-living sinkholes are formed. The weak fields are confined in the mesogranular vertices and concentrated by converging granular flows up to kG values. The newly formed magnetic element is constantly being buffeted by surrounding granules, and it is fragmented into a series of more elemental inner magnetic cores. The continuous inward advection to the sinkhole, however, prevents the cores to be detached from the global structure and even fuse them again into a single magnetic element. The recurrent coalescence and fragmentation of magnetic cores results in magnetic field oscillations of the magnetic feature.

BIBLIOGRAPHY

- Asensio Ramos, A. 2009, *ApJ*, 701, 1032
- Attie, R., Innes, D. E., & Potts, H. E. 2009, *A&A*, 493, L13
- Babcock, H. W., & Babcock, H. D. 1955, *ApJ*, 121, 349
- Balmaceda, L., Vargas Domínguez, S., Palacios, J., Cabello, I., & Domingo, V. 2010, *A&A*, 513, L6
- Barthol, P., Gandorfer, A., Solanki, S. K., et al. 2011, *SoPh*, 268, 1
- Beck, C., Bellot Rubio, L. R., Schlichenmaier, R., Sütterlin, P. 2007a, *A&A*, 472, 607
- Beck, C., Mikurda, K., Bellot Rubio, L. R., Schlichenmaier, R., Sütterlin, P. 2007b, *Modern Solar Facilities—Advanced Solar Science*, ed. F. Kneer, K. G. Puschmann & A. D. Wittmann. Published by Universitätsverlag Göttingen, 165
- Bellot Rubio, L. R., Ruiz Cobo, B., & Collados, M. 1997, *ApJL*, 478, L45
- Bellot Rubio, L. R., Ruiz Cobo, B., & Collados, M. 1998, *ApJ*, 506, 805
- Bellot Rubio, L. R., Ruiz Cobo, B., & Collados, M. 2000, *ApJ*, 535, 489
- Bellot Rubio, L. R., Rodríguez Hidalgo, I., Collados, M., Khomenko, E., & Ruiz Cobo, B. 2001, *ApJ*, 560, 1010
- Bellot Rubio, L. R., & Collados, M. 2003, *A&A*, 406, 357
- Bellot Rubio, L. R., & Orozco Suárez, D. 2015, *Living Reviews in Solar Physics*, in press
- Berger, T. E., & Title, A. M. 1996, *ApJ*, 463, 365
- Berger, T. E., Löfdahl, M. G., Shine, R. S., & Title, A. M. 1998, *ApJ*, 495, 973
- Berger, T. E., & Title, A. M. 2001, *ApJ*, 553, 449
- Berger, T. E., Rouppe van der Voort, L. H. M., Löfdahl, M. G., et al. 2004, *A&A*, 428, 613
- Berkefeld, T., Schmidt, W., Soltau, D., et al. 2011, *SoPh*, 268, 103
- Bonet, J. A., Márquez, I., Sánchez Almeida, J., Cabello, I., & Domingo, V. 2008, *ApJL*, 687, L131

- Bonet, J. A., Márquez, I., Sánchez Almeida, J., et al. 2010, *ApJL*, 723, L139
- Borrero, J. M., Martínez-Pillet, V., Schlichenmaier, R., et al. 2010, *ApJL*, 723, L144
- Borrero, J. M., & Kobel, P. 2011, *A&A*, 527, A29
- Brandt, P. N., Scharmer, G. B., Ferguson, S., Shine, R. A., & Tarbell, T. D. 1988, *Nature*, 335, 238
- Brandt, P. N., Ferguson, S., Shine, R. A., Tarbell, T. D., & Scharmer, G. B. 1991, *A&A*, 241, 219
- Buehler, D., Lagg, A., Solanki, S. K., & van Noort, M. 2015, *A&A*, 576, A27
- Büntje, M., Steiner, O., & Pizzo, V. J. 1993, *A&A*, 268, 299
- Büntje, M. 1993, *A&A*, 276, 236
- Bushby, P. J., Houghton, S. M., Proctor, M. R. E., & Weiss, N. O. 2008, *MNRAS*, 387, 698
- Bushby, P. J., Favier, B., Proctor, M. R. E., & Weiss, N. O. 2012, *Geophysical and Astrophysical Fluid Dynamics*, 106, 508
- Bushby, P. J., & Favier, B. 2014, *A&A*, 562, A72
- Cattaneo, F. 1999, *ApJL*, 515, L39
- Cattaneo, F., Lenz, D., & Weiss, N. 2001, *ApJL*, 563, L91
- Centeno, R., Socas-Navarro, H., Lites, B., et al. 2007, *ApJL*, 666, L137
- Danilovic, S., Schüssler, M., & Solanki, S. K. 2010a, *A&A*, 509, A76
- Danilovic, S., Beeck, B., Pietarila, A., et al. 2010b, *ApJL*, 723, L149
- Deinzer, W., Hensler, G., Schüssler, M., & Weisshaar, E. 1984, *A&A*, 139, 435
- Del Toro Iniesta, J. C. 1996, *Vistas in Astronomy*, 40, 241
- Del Toro Iniesta, J. C., & Ruiz Cobo, B. 1996, *SoPh*, 164, 169
- Del Toro Iniesta, J. C., & Collados, M. 2000, *AO*, 39, 1637
- Del Toro Iniesta, J. C. 2003, *Introduction to Spectropolarimetry* (Cambridge: Cambridge Univ. Press)
- Del Toro Iniesta, J. C., Orozco Suárez, D., & Bellot Rubio, L. R. 2010, *ApJ*, 711, 312
- Del Toro Iniesta, J. C., & Martínez Pillet, V. 2012, *ApJS*, 201, 22
- de Wijn, A. G., Rutten, R. J., Haverkamp, E. M. W. P., Sütterlin, P. 2005, *A&A*, 441, 1183
- de Wijn, A. G., Lites, B. W., Berger, T. E., et al. 2008, *ApJ*, 684, 1469
- de Wijn, A. G., Stenflo, J. O., Solanki, S. K., & Tsuneta, S. 2009, *ssr*, 144, 275
- Domínguez Cerdeña, I. 2003a, *A&A*, 412, L65

- Domínguez Cerdeña, I., Kneer, F., & Sánchez Almeida, J. 2003b, *ApJL*, 582, L55
- Domínguez Cerdeña, I., Sánchez Almeida, J., & Kneer, F. 2003c, *A&A*, 407, 741
- Edwin, P. M., & Roberts, B. 1983, *SoPh*, 88, 179
- Fischer, C. E., de Wijn, A. G., Centeno, R., Lites, B. W., & Keller, C. U. 2009, *A&A*, 504, 583
- Foukal, P. V. 2004, *Solar Astrophysics*, 2nd ed. New York, Wiley-Interscience, 2004
- Gandorfer, A., Grauf, B., Barthol, P., et al. 2011, *SoPh*, 268, 35
- Gingerich, O., Noyes, R. W., Kalkofen, W., & Cuny, Y. 1971, *SoPh*, 18, 347
- Gonsalves, R. A. 1982, *Optical Engineering*, 21, 829
- Goode, P. R., Yurchyshyn, V., Cao, W., et al. 2010, *ApJL*, 714, L31
- Gošić, M., Bellot Rubio, L. R., Orozco Suárez, D., Katsukawa, Y., & Del Toro Iniesta, J. C. 2014, *ApJ*, 797, 49
- Gošić, M., Bellot Rubio, L. R., Del Toro Iniesta, J. C., Orozco Suárez, D., & Katsukawa, Y. 2015, *ApJ*, submitted
- Grossmann-Doerth, U., Schüssler, M., & Solanki, S. K. 1988, *A&A*, 206, L37
- Grossmann-Doerth, U., Keller, C. U., & Schuessler, M. 1996, *A&A*, 315, 610
- Grossmann-Doerth, U., Schüssler, M., & Steiner, O. 1998, *A&A*, 337, 928
- Guglielmino, S. L., Martínez Pillet, V., Bonet, J. A., et al. 2012, *ApJ*, 745, 160
- Hale, G. E. 1908, *ApJ*, 28, 315
- Hasan, S. S. 1985, *A&A*, 143, 3
- Hirzberger, J., Feller, A., Riethmüller, T. L., Gandorfer, A., & Solanki, S. K. 2011, *A&A*, 529, A132
- Howard, R., & Stenflo, J. O. 1972, *SoPh*, 22, 402
- Ishikawa, R., Tsuneta, S., Kitakoshi, Y., et al. 2007, *A&A*, 472, 911
- Ishikawa, R., & Tsuneta, S. 2009, *A&A*, 495, 607
- Ishikawa, R., & Tsuneta, S. 2010, *ApJL*, 718, L171
- Jafarzadeh, S., Solanki, S. K., Feller, A., et al. 2013, *A&A*, 549, A116
- Jess, D. B., Shelyag, S., Mathioudakis, M., et al. 2012, *ApJ*, 746, 183
- Jin, C., Wang, J., & Zhou, G. 2009, *ApJ*, 697, 693
- Jin, C. L., Wang, J. X., & Xie, Z. X. 2012, *SoPh*, 280, 51
- Jin, C., & Wang, J. 2015a, *ApJ*, 806, 174

- Jin, C. L., & Wang, J. X. 2015b, *ApJ*, 807, 70
- Kato, Y., Steiner, O., Steffen, M., & Suematsu, Y. 2011, *ApJL*, 730, L24
- Keller, C. U. 1992, *Nature*, 359, 307
- Kentischer, T. J., Schmidt, W., Sigwarth, M., & Uexkuell, M. V. 1998, *A&A*, 340, 569
- Khomenko, E. V., Collados, M., Solanki, S. K., Lagg, A., & Trujillo Bueno, J. 2003, *A&A*, 408, 1115
- Khomenko, E. V., Shelyag, S., Solanki, S. K., Vögler, A. 2005, *A&A*, 442, 1059
- Khomenko, E., Martínez Pillet, V., Solanki, S. K., et al. 2010, *ApJL*, 723, L159
- Kiselman, D., Rutten, R. J., & Plez, B. 2001, *Recent Insights into the Physics of the Sun and Heliosphere: Highlights from SOHO and Other Space Missions*, 203, 287
- Kitiashvili, I. N., Kosovichev, A. G., Wray, A. A., & Mansour, N. N. 2010, *ApJ*, 719, 307
- Klimchuk, J. A. 2006, *SoPh*, 234, 41
- Kosugi, T., Matsuzaki, K., Sakao, T., et al. 2007, *SoPh*, 243, 3
- Krall, N. A., & Trivelpiece, A. W. 1973, *Principles of Plasma Physics* (Tokyo: McGraw-Hill)
- Lagg, A., Solanki, S. K., Riethmüller, T. L., et al. 2010, *ApJL*, 723, L164
- Landi Degl'Innocenti, E. 1987, *Numerical Radiative Transfer*, 265
- Landi Degl'Innocenti, E., & Landolfi, M. 2004, *Astrophysics and Space Science Library*, 307,
- Langangen, Ø., De Pontieu, B., Carlsson, M., et al. 2008, *ApJL*, 679, L167
- Leitzinger, M., Brandt, P. N., Hanslmeier, A., Pötzi, W., & Hirzberger, J. 2005, *A&A*, 444, 245
- Lin, H. 1995, *ApJ*, 446, 421
- Lin, H., & Rimmele, T. 1999, *ApJ*, 514, 448
- Lites, B. W., Rutten, R. J., & Kalkofen, W. 1993, *ApJ*, 414, 345
- Lites, B. W., Leka, K. D., Skumanich, A., Martinez Pillet, V., & Shimizu, T. 1996, *ApJ*, 460, 1019
- Lites, B. W., & Socas-Navarro, H. 2004, *ApJ*, 613, 600
- Lites, B. W., Kubo, M., Socas-Navarro, H., et al. 2008, *ApJ*, 672, 1237
- Lites, B. W. 2011, *ApJ*, 737, 52
- Lites, B. W., Akin, D. L., Card, G., et al. 2013, *SoPh*, 283, 579

- Livingston, W., & Harvey, J. 1971, *Solar Magnetic Fields*, 43, 51
- Livingston, W. C., & Harvey, J. 1975, *BAAS*, 7, 346
- Manso Sainz, R., Martínez González, M. J., & Asensio Ramos, A. 2011, *A&A*, 531, L9
- Márquez, I., Sánchez Almeida, J., & Bonet, J. A. 2006, *ApJ*, 638, 553
- Martin, S. F. 1984, *Small-Scale Dynamical Processes in Quiet Stellar Atmospheres*, 30
- Martínez González, M. J., Collados, M., & Ruiz Cobo, B. 2006, *A&A*, 456, 1159
- Martínez González, M. J., Collados, M., Ruiz Cobo, B., & Solanki, S. K. 2007, *A&A*, 469, L39
- Martínez González, M. J., Collados, M., Ruiz Cobo, B., & Beck, C. 2008, *A&A*, 477, 953
- Martínez González, M. J., & Bellot Rubio, L. R. 2009, *ApJ*, 700, 1391
- Martínez González, M. J., Manso Sainz, R., Asensio Ramos, A., & Bellot Rubio, L. R. 2010, *ApJL*, 714, L94
- Martínez González, M. J., Asensio Ramos, A., Manso Sainz, R., et al. 2011, *ApJL*, 730, L37
- Martínez González, M. J., Manso Sainz, R., Asensio Ramos, A., & Hijano, E. 2012a, *ApJ*, 755, 175
- Martínez González, M. J., Bellot Rubio, L. R., Solanki, S. K., et al. 2012b, *ApJL*, 758, L40
- Martínez Pillet, V., Lites, B. W., & Skumanich, A. 1997, *ApJ*, 474, 810
- Martínez Pillet, V., Bonet, J. A., Collados, M. V., et al. 2004, *SPIE*, 5487, 1152
- Martínez Pillet, V. 2007, in *Proc. Second Solar Orbiter Workshop*, ed. L. Conroy (ESA SP-641; Noordwijk: ESA), www.esa.int/esapub/conferences/toc/tocSP641.pdf
- Martínez Pillet, V., Del Toro Iniesta, J. C., Álvarez-Herrero, A., et al. 2011a, *SoPh*, 268, 57
- Martínez Pillet, V., Del Toro Iniesta, J. C., & Quintero Noda, C. 2011b, *A&A*, 530, A111
- Martínez Pillet, V. 2013, *ssr*, 178, 141
- Matloch, L., Cameron, R., Schmitt, D., & Schüssler, M. 2009, *A&A*, 504, 1041
- Matloch, L., Cameron, R., Shelyag, S., Schmitt, D., & Schüssler, M. 2010, *A&A*, 519, A52
- Meyer, F., Schmidt, H. U., & Weiss, N. O. 1977, *MNRAS*, 179, 741
- Moll, R., Cameron, R. H., & Schüssler, M. 2011, *A&A*, 533, A126
- Molowny-Horas, R., & Yi, Z. 1994, *Internal Rep. 31*, Institute of Theoretical Astrophysics (Oslo: Univ. Oslo)
- Muller, R. 1983, *SoPh*, 85, 113

- Muller, R., & Roudier, T. 1984, *SoPh*, 94, 33
- Muller, R., Hulot, J. C., & Roudier, T. 1989, *SoPh*, 119, 229
- Muller, R., Auffret, H., Roudier, T., et al. 1992, *Nature*, 356, 322
- Muller, R., & Roudier, T. 1992, *SoPh*, 141, 27
- Muller, R., Dollfus, A., Montagne, M., Moity, J., & Vigneau, J. 2000, *A&A*, 359, 373
- Nagata, S., Tsuneta, S., Suematsu, Y., et al. 2008, *ApJL*, 677, L145
- Narayan, G., & Scharmer, G. B. 2010, *A&A*, 524, A3
- Nordlund, Å. 1985, *SoPh*, 100, 209
- Nordlund, Å., Stein, R. F., & Asplund, M. 2009, *Living Reviews in Solar Physics*, 6, 2
- November, L. J., Toomre, J., Gebbie, K. B., & Simon, G. W. 1981, *ApJL*, 245, L123
- November, L. J. 1986, *AO*, 25, 392
- November, L. J., & Simon, G. W. 1988, *ApJ*, 333, 427
- Orozco Suárez, D., Bellot Rubio, L. R., Del Toro Iniesta, J. C., et al. 2007a, *PASJ*, 59, 837
- Orozco Suárez, D., Bellot Rubio, L. R., Del Toro Iniesta, J. C., et al. 2007b, *ApJL*, 670, L61
- Orozco Suárez, D., & Bellot Rubio, L. R. 2012, *ApJ*, 751, 2
- Orozco Suárez, D., Katsukawa, Y., & Bellot Rubio, L. R. 2012, *ApJL*, 758, L38
- Parker, E. N. 1963, *ApJ*, 138, 552
- Parker, E. N. 1975, *SoPh*, 40, 291
- Parker, E. N. 1978, *ApJ*, 221, 368
- Parnell, C. E., & De Moortel, I. 2012, *Royal Society of London Philosophical Transactions Series A*, 370, 3217
- Paxman, R. G., Seldin, J. H., Loefdahl, M. G., Scharmer, G. B., & Keller, C. U. 1996, *ApJ*, 466, 1087
- Pesnell, W. D., Thompson, B. J., & Chamberlin, P. C. 2012, *SoPh*, 275, 3
- Petrovay, K., & Szakaly, G. 1993, *A&A*, 274, 543
- Piddington, J. H. 1975, *APSS*, 34, 347
- Pötzi, W., & Brandt, P. N. 2005, *Hvar Observatory Bulletin*, 29, 61
- Pötzi, W., & Brandt, P. N. 2007, *Central European Astrophysical Bulletin*, 31, 11
- Priest, E. 2014, *Magnetohydrodynamics of the Sun*, by Eric Priest, Cambridge, UK: Cambridge University Press, 2014,

- Quintero Noda, C., Martínez Pillet, V., Borrero, J. M., & Solanki, S. K. 2013, *A&A*, 558, A30
- Quintero Noda, C., Ruiz Cobo, B., & Orozco Suárez, D. 2014, *A&A*, 566, AA139
- Rast, M. P. 2003, *ApJ*, 597, 1200
- Rees, D. E., Durrant, C. J., & Murphy, G. A. 1989, *ApJ*, 339, 1093
- Rempel, M. 2014, *ApJ*, 789, 132
- Requerey, I. S., Del Toro Iniesta, J. C., Bellot Rubio, L. R., et al. 2014, *ApJ*, 789, 6
- Requerey, I. S., Del Toro Iniesta, J. C., Bellot Rubio, L. R., et al. 2015, *ApJ*, 810, 79
- Rezaei, R., Steiner, O., Wedemeyer-Böhm, S., et al. 2007, *A&A*, 476, L33
- Riethmüller, T. L., Solanki, S. K., Berdyugina, S. V., et al. 2014, *A&A*, 568, A13
- Rieutord, M., Roudier, T., Malherbe, J. M., & Rincon, F. 2000, *A&A*, 357, 1063
- Rieutord, M., & Rincon, F. 2010, *Living Reviews in Solar Physics*, 7, 2
- Rimmele, T. R. 2004, *ApJ*, 604, 906
- Roudier, T., Espagnet, O., Muller, R., & Vigneau, J. 1994, *A&A*, 287, 982
- Roudier, T., Malherbe, J. M., Vigneau, J., & Pfeiffer, B. 1998, *A&A*, 330, 1136
- Roudier, T., Lignières, F., Rieutord, M., Brandt, P. N., & Malherbe, J. M. 2003, *A&A*, 409, 299
- Roudier, T., & Muller, R. 2004, *A&A*, 419, 757
- Roupe van der Voort, L. H. M., Hansteen, V. H., Carlsson, M., et al. 2005, *A&A*, 435, 327
- Ruiz Cobo, B., & Del Toro Iniesta, J. C. 1992, *ApJ*, 398, 375
- Ruiz Cobo, B., & Del Toro Iniesta, J. C. 1994, *A&A*, 283, 129
- Sánchez Almeida, J., Bonet, J. A., Viticchié, B., & Del Moro, D. 2010, *ApJL*, 715, L26
- Sánchez Almeida, J., & Lites, B. W. 2000, *ApJ*, 532, 1215
- Sánchez Almeida, J., & Martínez González, M. 2011, *Solar Polarization* 6, 437, 451
- Scharmer, G. B., Petterson, L., Brown, D. S., & Rehn, J. 1985, *AO*, 24, 2558
- Scherrer, P. H., Schou, J., Bush, R. I., et al. 2012, *SoPh*, 275, 207
- Schüssler, M. 1984, *A&A*, 140, 453
- Semel, M., & López Ariste, A. 1999, *A&A*, 342, 201
- Shelyag, S., Keys, P., Mathioudakis, M., & Keenan, F. P. 2011, *A&A*, 526, A5
- Shimizu, T., Lites, B. W., Katsukawa, Y., et al. 2008, *ApJ*, 680, 1467

- Shine, R. A., Simon, G. W., & Hurlburt, N. E. 2000, *SoPh*, 193, 313
- Simon, G. W., Title, A. M., Topka, K. P., et al. 1988, *ApJ*, 327, 964
- Smithson, R. C. 1975, *BAAS*, 7, 346
- Sobotka, M., Vázquez, M., Bonet, J. A., Hanslmeier, A., & Hirzberger, J. 1999, *ApJ*, 511, 436
- Solanki, S. K., & Stenflo, J. O. 1984, *A&A*, 140, 185
- Solanki, S. K. 1986, *A&A*, 168, 311
- Solanki, S. K., Keller, C., & Stenflo, J. O. 1987, *A&A*, 188, 183
- Solanki, S. K. 1993, *ssr*, 63, 1
- Solanki, S. K., Barthol, P., Danilovic, S., et al. 2010, *ApJL*, 723, L127
- Spruit, H. C. 1976, *SoPh*, 50, 269
- Spruit, H. C. 1979, *SoPh*, 61, 363
- Spruit, H. C., & Zweibel, E. G. 1979, *SoPh*, 62, 15
- Spruit, H. C., Nordlund, Å., & Title, A. M. 1990, *ARAA*, 28, 263
- Stein, R. F., & Nordlund, Å. 1998, *ApJ*, 499, 914
- Stein, R. F., & Nordlund, Å. 2006, *ApJ*, 642, 1246
- Steiner, O., Grossmann-Doerth, U., Schüssler, M., & Knölker, M. 1996, *SoPh*, 164, 223
- Steiner, O., Grossmann-Doerth, U., Knölker, M., & Schüssler, M. 1998, *ApJ*, 495, 468
- Steiner, O. 1999, in *ASP Conf. Ser. 184, Third Advances in Solar Physics Euroconference: Magnetic Fields and Oscillations*, ed. B. Schmieder, A. Hofmann, & J. Staude (San Francisco, CA: ASP), 38
- Steiner, O., Franz, M., Bello González, N., et al. 2010, *ApJL*, 723, L180
- Stenflo, J. O. 1973, *SoPh*, 32, 41
- Stenflo, J. O., & Harvey, J. W. 1985, *SoPh*, 95, 99
- Stix, M. 2002, *The sun : an introduction – 2nd ed. /Michael Stix. Berlin : Springer, 2002. QB 521 .S75,*
- Takeuchi, A. 1999, *ApJ*, 522, 518
- Title, A. M., Tarbell, T. D., Topka, K. P., et al. 1989, *ApJ*, 336, 475
- Title, A. M., Topka, K. P., Tarbell, T. D., et al. 1992, *ApJ*, 393, 782
- Tsuneta, S., Ichimoto, K., Katsukawa, Y., et al. 2008, *SoPh*, 249, 167

- Usoskin, I. G. 2013, *Living Reviews in Solar Physics*, 10, 1
- Utz, D., Del Toro Iniesta, J. C., Bellot Rubio, L. R., et al. 2014, *ApJ*, 796, 79
- Vargas Domínguez, S., Palacios, J., Balmaceda, L., Cabello, I., & Domingo, V. 2011, *MNRAS*, 416, 148
- Vargas Domínguez, S., Palacios, J., Balmaceda, L., Cabello, I., & Domingo, V. 2015, *SoPh*, 290, 301
- Verma, M., Steffen, M., & Denker, C. 2013, *A&A*, 555, A136
- Viticchié, B., Del Moro, D., Berrilli, F., Bellot Rubio, L., & Tritschler, A. 2009, *ApJL*, 700, L145
- Viticchié, B., Del Moro, D., Criscuoli, S., & Berrilli, F. 2010, *ApJ*, 723, 787
- Vögler, A., Shelyag, S., Schüssler, M., et al. 2005, *A&A*, 429, 335
- Vögler, A., & Schüssler, M. 2007, *A&A*, 465, L43
- Wang, H., & Zirin, H. 1988, *SoPh*, 115, 205
- Wang, J., Wang, H., Tang, F., Lee, J. W., & Zirin, H. 1995a, *SoPh*, 160, 277
- Wang, Y., Noyes, R. W., Tarbell, T. D., & Title, A. M. 1995b, *ApJ*, 447, 419
- Webb, A. R., & Roberts, B. 1978, *SoPh*, 59, 249
- Wedemeyer-Böhm, S., & Rouppe van der Voort, L. 2009, *A&A*, 507, L9
- Wedemeyer-Böhm, S., Scullion, E., Steiner, O., et al. 2012, *Nature*, 486, 505
- Weiss, N. O. 1964, *MNRAS*, 128, 225
- Weiss, N. O. 1966, *Royal Soc. London Proc. Ser. A*, 293, 310
- Weiss, N. O., Brownjohn, D. P., Matthews, P. C., & Proctor, M. R. E. 1996, *MNRAS*, 283, 1153
- Wiegelmann, T., Thalmann, J. K., & Solanki, S. K. 2014, *A&A Revs*, 22, 78
- Wiehr, E. 1978, *A&A*, 69, 279
- Yelles Chaouche, L., Moreno-Insertis, F., Martínez Pillet, V., et al. 2011, *ApJL*, 727, L30
- Yi, Z. 1992, PhD thesis, University of Oslo, Oslo
- Yi, Z., & Engvold, O. 1993, *SoPh*, 144, 1
- Zhou, G. P., Wang, J. X., & Jin, C. L. 2010, *SoPh*, 267, 63
- Zhou, G., Wang, J., & Jin, C. 2013, *SoPh*, 283, 273

